Exploring dipole electric strength functions through QRPA : Systematic calculations and other developments

Luis González-Miret Zaragoza

université
PARIS-SACLAY

Exploring dipole electric strength functions through QRPA : Systematic calculations and other developments

Exploration des fonctions de force dipolaires électriques avec la QRPA : Calculs systématiques et autres développements

Thèse de doctorat de l'université Paris-Saclay

École doctorale n° 576, PHENIICS
Particules, Hadrons, Énergie, Noyau,
Instrumentation, Imagerie, Cosmos et Simulation
Spécialité de doctorat : Physique nucléaire
Graduate school : Physique
Référent : Faculté des sciences d'Orsay

Thèse préparée dans l'unité de recherche **Laboratoire Matière en Conditions Extrêmes (Université Paris-Saclay, CEA)** ,
sous la direction de **Stéphane HILAIRE**, Directeur de recherche,
le co-encadrement de **Sophie PÉRU**, Directrice de recherche
et le co-encadrement de **Jean-Paul EBRAN**, Directeur de recherche

Thèse soutenue à Paris-Saclay, le 25 Novembre 2024, par

Luis GONZÁLEZ-MIRET ZARAGOZA

Composition du jury

Membres du jury avec voix délibérative

David VERNEY Directeur de recherche, IJCLab - Université Paris-Saclay	Président
Gianluca COLÒ Directeur de recherche, Università degli Studi di Milano INFN	Rapporteur & Examinateur
Dario VRETENAR Professeur, Sveučilište u Zagrebu	Rapporteur & Examinateur
Ann-Cecilie LARSEN Professeur, Universitetet i Oslo	Examinatrice
Kamila SIEJA Directrice de recherche, IPHC, Strasbourg	Examinatrice

THESE DE DOCTORAT

NNT : 2024UPASP146

université PARIS-SACLAY

ÉCOLE DOCTORALE
Particules, hadrons, énergie et noyau : instrumentation, imagerie, cosmos et simulation (PHENIICS)

Titre : Exploration des fonctions de force dipolaires électriques avec la QRPA : Calculs systématiques et autres développements

Mots clés : Méthodes à N-corps, HFB, QRPA, Structure nucleaire, Fonctions force, Résonances gèantes

Résumé : La quête d'une description microscopique complète du noyau atomique reste un problème ouvert après près d'un siècle de recherche. Les divers phénomènes présents dans le noyau, qui découlent principalement de sa nature quantique à plusieurs corps, ont conduit à la prolifération de modèles, chacun se spécialisant dans la description d'un ensemble donné de caractéristiques nucléaires. Pour comprendre pleinement le comportement collectif d'un point de vue microscopique, il est essentiel d'aller au-delà de l'approche statique du champ moyen. Toutefois, en raison principalement du coût de calcul élevé nécessaire, il existe relativement peu de méthodes de ce type qui permettent de réaliser des études systématiques sur l'ensemble de la carte nucléaire. Une exception notable est la méthode QRPA (Quasiparticle Random Phase Approximation), qui permet de décrire sur un pied d'égalité les excitations nucléaires individuelles et collectives tout en incorporant les effets d'appariement. Des études antérieures ont été réalisées avec la force Gogny D1M pour produire des fonctions de force gamma pour tous les noyaux. Néanmoins, pour une compréhension plus complète, l'utilisation d'autres interactions et approches au sein de la QRPA est primordiale. Dans cette thèse, de nouvelles études systématiques QRPA sont présentées, ainsi que de nouveaux développements numériques et formels autour de la QRPA.

Tout d'abord, deux études systématiques des transitions gamma E1 sont discutées. Ici, le problème QRPA est abordé en utilisant la méthode des amplitudes finies (FAM), qui permet l'évaluation rapide des fonctions de force lissées. La première étude utilise le lagrangien effectif covariant DD-PC1 pour effectuer des calculs approfondis sur l'ensemble de la carte nucléaire. En outre, une autre étude examine les mêmes transitions dans des noyaux légers et de masse moyenne en utilisant des interactions chirales, qui fournissent une caractérisation réaliste de la force internucléon fondée sur la chromodynamique quantique à travers de la théorie effective des champs chirale. En particulier, nous présentons les tout premiers résultats de la QRPA chirale utilisant un champ moyen déformé triaxialement, explorant l'impact de cette déformation sur la réponse de la QRPA dans ^{24}Mg et ^{32}S.

Au-delà des études systématiques de la QRPA, deux autres développements sont présentés. Tout d'abord, nous nous attaquons au problème de l'obtention d'états excités QRPA exacts à l'aide de l'approche FAM. Dans sa formulation originale, FAM était utilisé pour calculer les fonctions de force, tandis que l'obtention des états propres QRPA n'était possible que par une procédure de post-traitement. Dans cette thèse, nous introduisons une nouvelle méthode basée sur l'algorithme de Jacobi-Davidson, qui permet le calcul efficace de plusieurs états propres QRPA ciblés avec un temps de calcul significativement réduit par rapport à l'approche QRPA matricielle. Enfin, nous proposons une nouvelle formule simple pour corriger la violation du principe de Pauli dans la QRPA, qui est appliquée pour calculer les énergies de corrélation.

Title : Exploring dipole electric strength functions through QRPA : Systematic calculations and other developments

Keywords : Many-body methods, HFB, QRPA, Nuclear structure, Strength functions, Giant resonances

Abstract : The quest for a comprehensive microscopic description of the atomic nucleus remains an open problem after almost a century of research. The diverse phenomena present within the nucleus, primarily arising from its many-body quantum nature, have led to a proliferation of models, each specializing in describing a given set of nuclear features. To fully understand collective behavior from a microscopic perspective, it is essential to move beyond a static mean-field approach. However, due mainly to the high computational cost required to do so, relatively few such methods exist that provide systematic studies across the entire nuclear chart. One notable exception is the Quasiparticle Random Phase Approximation (QRPA) method, which allows for the description of both single-particle and collective nuclear excitations on the same footing while incorporating pairing effects. Previous studies have been carried out with the Gogny D1M force to produce gamma-strength functions for all nuclei. Nevertheless, for a more complete understanding, the use of other effective interactions and approaches within QRPA is paramount. In this thesis, new systematic QRPA studies are presented, alongside some new numerical and formal developments around QRPA. First, two systematic studies of gamma E1 transitions are discussed. Here, the QRPA problem is addressed using the Finite Amplitude Method (FAM), which enables the rapid evaluation of smoothed strength functions. The first study employs the covariant effective Lagrangian DD-PC1 to conduct extensive calculations across the nuclear chart. Additionally, another study investigates the same transitions in light and mid-mass nuclei using chiral interactions, which provide a realistic characterization of the internucleon force grounded in Quantum Chromodynamics through effective field theory. Notably, we present the first-ever chiral-QRPA results using a triaxially deformed mean field, exploring the impact of this deformation on the QRPA response in ^{24}Mg and ^{32}S.

Beyond the systematic QRPA studies, two further developments are presented. Firstly, we tackle the problem of obtaining exact QRPA excited states using the FAM approach. In its original formulation, FAM was used to calculate strength functions, while obtaining the QRPA eigenstates was only possible via a post-processing procedure. In this thesis, we introduce a new method based on the Jacobi-Davidson algorithm, which enables the efficient calculation of several targeted QRPA eigenstates with significantly reduced computational time compared to the matrix QRPA approach. Lastly, we propose a new straightforward formula to correct for the violation of the Pauli principle in QRPA, which is applied to compute correlation energies.

A mis abuelos

Acknowledgements

May you live in interesting times

Chinese curse, apocryphal

I would like to start by thanking all the members of the jury. Thank you for reading through my work and providing valuable comments that have improved the quality of the manuscript. I would like to give special thanks to David Verney. David, your role as the director of the doctoral school has been crucial, and without you, this work might not have been completed.

Now, let's continue with the supervising team: First of all, to Sophie Péru. Thank you for everything. Thank you for all the physics you've taught me. Thank you for the trust you've placed in me and in my ideas. Thank you for pulling me out of the hole every time I became demotivated. I will miss our colorful lunch breaks where we talked about everything: physics, politics, and sometimes got a little philosophical. If I am the scientist I am today, it's because of you.

Now, to Stéphane Hilaire. Thank you for all the advice you've given me throughout this thesis. Thank you for closely following my work and always providing valuable insights. Thank you for all the help you've given me to succeed, not only during my thesis but beyond. I'm especially grateful for all the rides to Gare du Guichet. As I've mentioned before, I've had the privilege of having the most renowned taxi driver one could ask for. It was a great ride.

To Jean-Paul Ebran, thank you for your highly motivating attitude and for always being in tune with what's the real deal in the field. Thank you for initiating the various collaborations that have been so fruitful throughout my thesis. And thank you for taking the time to discuss things with me and clarify all my doubts.

To my collaborators,

First and foremost, to Mikael Frosini. Your contribution in this work has been huge. Thank you for always being willing to discuss, debug, and think together. Some of the most fun I have had during this thesis it's been working on the projects we've pursued together. Thank you for your hospitality in Cadarache, at work and your place. You have a lovely family, and your (and your wife's) cooking skills are on par with your skills in boardgames.

Thanks to Elias Khan and Stéphane Gorielly for your contributions to the work, especially the use of your codes to apply the strength functions generated in this thesis. Thanks again to Stéphane and to Wouter Ryssens for your hospitality in Brussels and for accepting me to work with you for the next few years. Thanks to Thomas Duguet for his insights in the part of this work concerning chiral EFT derived interactions. Thanks also to Caroline Robin and Gabriel Martínez Pinedo for their hospitality in GSI. Thanks Diana and Ante for our great discussions there, and thank you for the fun! Thanks also to Martino Trassinelli and Piet Van Isacker for the work we have done together.

Thanks to my colleagues in Bruyères-le-Châtel. Thanks to Marc Dupuis for our nice discussions. Thanks to Nöel Dubray and his young PhD candidate Junah Newsome for their help working with the cluster. Thank to my fellow PhD students and post-docs for all our time together and support ! Thanks you, Paul Carpentier, for all the discussions, on every topic.

Thanks to my disparate band of (mostly foreigner) friends in Paris. You have been a source of joy during my four-year stay in this crazy city. I am hesitant to give names because I'm sure I'll forget some important people. If you are reading this and feel that you should be included in this group, rest assured because you are! A special thanks goes to the people in my band, current and former members : Thanks for the music we've played together.

Muchas gracias a mi familia: Mi madre, mi padre, mi hermana, tías, tíos, primas y primos. Desde la distancia me habéis aportado tanto. Si estoy aquí hoy es gracias a vosotros.

Lastly, thanks to Naya. You have been with me during all these years, in the good and not so good moments. Thank you for having shared your life with me. Thank you for all the love and care. $Ευχαριστώ$.

Contents

Introduction

Nuclear physics covers the study of interacting protons and neutrons, known collectively as nucleons. Nucleons form compact structures that lie at the core of atoms: the atomic nuclei. Experimentally measured nuclei range in size between 1 (^{1}H) and 298 (^{298}Og[1]) nucleons. These are kept bound using the nuclear interaction, which is a manifestation of the strong force. The nucleons themselves are not elementary particles but are rather a composite system formed by up and down quarks held together by the same force. Quantum chromodynamics (QCD), the theory of the strong interaction, is highly non-perturbative at the energy scales of the nucleus, which renders its direct application to the nuclear problem extremely difficult. Moreover, nucleons are color-chargeless[2], with the nuclear interaction being a residual effect of the strong interaction. This has been compared to the van der Waals force between electrically neutral molecules. Additionally, the *bare* interaction between free nucleons in the vacuum is different from that in the nuclear medium. On the other hand, irrespective of the interaction binding them, the nucleus presents all the difficulties of a mesoscopic quantum many-body system. A system with the number of particles typical of atomic nuclei cannot be described exclusively in terms of a statistical model, as finite size effects are relevant, but at the same time, the resolution of the A-body Schroedinger equation is an incredibly arduous task.

With all this in mind, the practitioner of nuclear structure faces two main questions:

- Which prescription may one use to model the internucleonic force?
- Which quantum many-body method may one use to solve the Schroedinger equation?

The answer to both these questions varies depending on the set of nuclear features that one aims at describing[3] and are fundamentally intertwined, as the answer to one influences the answer to the other. This translates into a myriad of methods, each specializing in describing a set of nuclear phenomena. In broad strokes, they can be divided into several subsets. In this introduction, we cover *Energy density functional* and *Ab initio* methods.

Energy Density Functional methods

In the single-reference *energy density functional* (EDF) [4, 5] approach, the wave-function of the nuclear system is modeled as a set of non-interacting particles embedded in a *mean-field* that is created by all the other nucleons. This mean-field wave function is obtained via the *Hartree-Fock*

[1] Heaviest sythesized nucleus at the time of writing [1].

[2] Color charge can be understood, in a simplistic way, as the equivalent of the electric charge for the strong interaction

[3] One may ask oneself, what are good results? Is the aim of nuclear structure to reproduce experiments no matter the price in terms of approximations? In reference [2, 3] the author argues that the actual goal of nuclear structure is to answer whether *the same nuclear forces that explain free-space scattering experiments also explain the properties of finite nuclei and nuclear matter when applied in nuclear many-body theory?* (*sic*). May the reader answer this question as they see fit.

method in closed-shell nuclei. In superfluid nuclei, pairing correlations [4] are captured via the use of *quasiparticles*, by which the concept of mean-field is preserved. The resulting method is *Hartree-Fock-Bogolyubov* (HFB). In EDF, the mean-field solution is taken as a good approximation to the nuclear ground state, while an effective interaction is used to model the internucleonic potential. Further correlations are captured by fitting the effective potentials to a set of experimental data. There exist different families of these effective interactions. From the non-covariant interactions, by far the most popular are the *Skyrme* [6] and *Gogny* [7] forces. While Skyrme is a contact force, Gogny-type interactions include finite range terms that cure some of the ultraviolet divergencies characteristic of δ-forces. Both these potentials include density-dependent terms to model the effect of the nuclear medium. This clashes with a proper definition of a Hamiltonian, as some of its terms depend on the wave function itself, so the term *pseudopotential* has often been dubbed. Moreover, the central object in EDF is the *energy functional*, obtained when contracting the Hamiltonian with the mean-field wave function. It is now common practice, in particular in the Skyrme case, to rule out any connection to the pseudopotential [5, 8, 9] and start directly from an energy functional that is not derivable from an effective force. This adds extra freedom to fit the EDF to experimental data. The number of different Skyrme parametrizations is enormous. Some examples of particular Skyrme functionals are the very widespread SLy4 [8] or the BSk family of mass models [10]. As for the Gogny case, we cite the D1S parametrization [11], which is considered the "standard" Gogny parametrization, thanks to its high predictive power in the region not too far from the stability valley. Additionally, the D1M parametrization [12] was fitted to reproduce nuclear masses with the same accuracy as the best liquid drop models available at the time. New parametrizations with modifications to the analytical form of the Gogny pseudopotential include the D2 [13] D3G3 [14] and DG [15] forms.

Within EDF, another possible approach is the covariant EDF methods [16, 17]. Its formulation is inspired by the original theory of Yukawa of the nucleon-nucleon interaction being mediated by pion exchange [18]. Relativistic energy density functionals are derived from an explicitly covariant Lagrangian, with the different terms containing the different possible couplings between the nucleon and meson fields. Point-coupling Lagrangians are also popular, where the meson exchange terms are substituted by contact terms between nucleons. The resulting mean-field formulation for the case of closed-shell nuclei is *Relativistic Mean-Field* (RMF). To account for pairing effects, the RMF EDF is complemented with a pairing term derived from a separable form that mimics the Gogny-D1S for the particle-particle channel. This results in the *Realativistic-Hartree-Bogolyubov*(RHB) models [19]. In both RMF and RHB, exchange or Fock terms are not explicitly included, with their effect being implicitly captured by the fitting of the Lagrangian to experimental data. Although *Relativistic Hartree-Fock-Bogolyubov* models do exist [20, 21, 22], their application has remained limited, as they involve a higher computational complexity and a refitting of the existing effective Lagrangians. On the other hand, RHB has been used extensively to calculate ground state energies and radii. Two examples of successful covariant Lagrangians are the DD-ME2 [23] and DD-PC1[24] parametrizations, which are meson-exchange and point coupling Lagrangians respectively. Both of them include density-dependent couplings, which take care of the effect of the nuclear medium. An example of the new generation of Lagrangians is the DD-PCX interaction, which has been fitted not only to ground state properties but also to the giant monopole resonance energy and dipole polarizability of ^{208}Pb [25].

[4] In nuclear physics, the loosely defined concept of *correlations* can be understood as the measure on which the nucleus escapes the description as a set of independent particles.

Ab initio approaches

A different approach is the use of the so-called *ab initio* methods [2, 26]. In EDF, the fact that correlations are captured in an uncontrolled way via the fitting of the free parameters of the energy functional is regarded as a limiting factor. On the other hand, the functional form of the EDF, although physically motivated, remains arbitrary, and there is no clear direction to follow to add new terms. *Ab initio* methods try to overcome this by using a *realistic description of the nuclear Hamiltonian* in combination with a many-body wave-function that can provide a controlled approximation to the exact solution to the Schroedinger equation. One of the main concerns of *ab initio* methods is to be able to give at each order an estimation of the uncertainties involved, which is possible only if both the interaction and the wave function are built in a systematically improvable manner. This points also at the final pillar of *ab initio* theories, which is to be able to provide a model-independent description of nuclear phenomena.

The modern way of obtaining nuclear Hamiltonians rooted in first principles is via chiral Effective Field Theory (χEFT) [27]. Effective field theories, which were introduced by Weinberg back in the late 1970s[28], are based on the separation of scales within a given physical theory. In the case of atomic nuclei, nucleons are confined systems of quarks and their internal structure is "invisible" below a certain energy threshold. Considering nucleons and pions as the relevant degrees of freedom of nuclear structure, the breakdown scale Λ_b of the effective theory lies on the order of the energy of the ρ meson ($\Lambda_b \sim 0.5 - 1$ GeV). In χEFT, one writes the most general Lagrangian compatible with the symmetries of the QCD, including its (broken) chiral symmetry[5]. By integrating out higher energy degrees of freedom, this results in internucleon interactions which are ordered in importance with respect to powers of Q/Λ_b, Q being a small momentum scale, typically identified with the mass of the smallest of the mesons, the π meson. This natural hierarchy gives Hamiltonians expanded to leading order (LO), next-to-leading order (NLO), next-to-next-to-leading order (N2LO), and so on. The interactions obtained via χEFT are called *chiral interactions*. Some examples of chiral Hamiltonians obtained in this way are the ones from references [29, 30, 26, 31].

Once a chiral interaction is obtained, the many-body method to use has to converge towards the exact solution of the A-body Schroedinger equation. *Exact diagonalization* methods such as no-core shell-model (NCSM)[32, 33] provide directly this solution, but their exponential scaling limits their applicability to the lightest nuclear systems. Expansion methods suppose a more computationally tractable solution, thanks to their polynomial scaling. The wave function in this context is built as an ordered series. Here, when mean-field descriptions are used, they provide the reference state on top of which the series is built. That can be the case in *Bogolyubov many-body perturbation theory* (BMBPT) [34, 35], *coupled cluster* (CC) [36, 37] and *in medium-similarity renormalization group* (IM-SRG) [38, 39] methods.

Gamma-ray strength functions

Up until now, we have focused on the description of the nuclear ground state via EDF or *ab initio methods*. However, information about nuclear spectroscopy is essential to describe a great deal of nuclear phenomena. One clear example of this is the modeling of r-processes, which is the mechanism by which around half of the nuclei of mass $A > 60$ are formed [40]. This is believed to happen in neutron-star mergers[41]. One of the main quantities that need to be evaluated to calculate the r-abundance distribution is the neutron capture rate, which highly depends on the electromagnetic

[5]Chiral symmetry is an exact symmetry of QCD only if the quarks have zero mass. In that case, pions appear as massless Goldstone bosons associated with the spontaneously broken chiral symmetry. However, up and down quarks have a mass of 2.3 and 4.8 MeV respectively, and subsequently result in massive pions

interaction. Thus, a fundamental ingredient for astrophysical models is the gamma-strength function, which measures the probability of exciting the nucleus for an incident photon of a given energy. Even if all electromagnetic multipolarities contribute, the electric dipole ($E1$) often dominates. Most of this strength is dominated by the *isovector giant dipole resonance* (IVGDR)[42], which corresponds to the high energy mode where protons and neutrons vibrate against each other. This resonance usually splits into two peaks for axially deformed nuclei and three for triaxially deformed ones. Being a quantity of such a big importance for the calculation of global abundances of elements in the Universe, having access to data for all nuclei is paramount. However, experimental data only exist for several hundreds of nuclei located in the stability valley [43]. Semi-empirical analytical models [44] like SMLO [45] are obtained by fitting experimentally known strengths with generalized Lorentzian curves and then expanded to the regions without experimental data by taking into account several physical arguments and theoretical predictions. However, for exotic nuclei, only microscopic models can provide predictions free of biases[6] coming from fitting such a small portion of all existing nuclei. On top of that, these simple models target only the reproduction of the GDR. However, the $E1$ strength has other important components, such as the pygmy resonance which is intimately related to the neutron-skin in neutron-rich nuclei [46, 47]. One of the most used methods to provide these strengths from a microscopic description is the *quasiparticle random phase approximation*, which we review in the next section.

Quasiparticle random phase approximation

The Quasiparticle Random Phase Approximation (QRPA)[7] is one of the most widespread methods to calculate *gamma*-ray strength functions. QRPA provides a way to access spectroscopy from an EDF at a tractable computational cost (although still big). In general, excited states can be accessed from an EDF by studying its behavior under a time-dependent external excitation. The resulting theory is *time-dependent Hartree-Fock-Bogolyubov* (TD-HFB). QRPA is the limit of small oscillations of TD-HFB. One of its advantages is that it can reproduce single-particle and collective states on the same footing. At the same time, QRPA takes into account correlations in the ground state neglected by HFB. Its main limitation is that, by construction, it is not able to reproduce large amplitude motion and rotational bands. For those cases, a multiconfiguration approach such as the *projectod generator coordinate method* (PGCM) is more appropriate. QRPA has extensively been used to reproduce giant resonances [48, 49, 50]. Another important application has been its use to model β-decay transitions in its charge-exchange formulation [51, 52]. Furthermore, a handful of QRPA studies exist that make use of chiral interactions [53, 54, 55, 56], although only for some limited cases. However, even if its formulation was relatively early in the life of the field [57], nuclear-chart-wide QRPA studies did not start appearing until the early 2000s [58, 59]. This is because the computational cost of QRPA is rather big, especially when considering explicitly pairing and a deformed mean field. A complete systematic study of deformed-QRPA E1 transitions did not appear until the mid-2010s [60, 61, 43]. This study was performed using the Gogny-D1M interaction, which was originally formulated as a mass model. To obtain a more complete knowledge, the performance of different EDFs should be studied, as well as the global performance of chiral interactions.

Luckily, the 2010s have also seen the development of several different methods attempting

[6] Of course, especially in the case of EDF, one can argue that similar biases come from the fact that the interactions themselves are fitted to experimental data. While true, in general, EDFs are fitted to more than just one kind of data, reproducing also properties of infinite nuclear matter. Moreover, some EDFs are fitted to a very large number of nuclei. That is the case for example of Gogny-D1M, fitted to reproduce more than 2000 nuclear masses

[7] For closed-shell nuclei, the method is referred to as RPA and it's built on top of an HF state.

to obtain certain QRPA results at a reduced computational cost. This has been achieved by the development of iterative QRPA methods, such as the Arnoldi [62, 63] or the Chebyshev kernel polynomial [64] methods. By far, the most widespread iterative method is the Finite Amplitude Method (FAM) algorithm [65, 66], which has been warmly welcomed by the community thanks to significantly reducing the computational cost for the evaluation of QRPA strengths. FAM has since been ingeniously used to extract QRPA amplitudes [67], moments [68] and density of states [69]. On top of that, the reduced computational effort needed in the FAM has allowed the development of triaxially deformed QRPA for the case of Skyrme interactions[70, 71], which are much more expensive in terms of memory and computing time in the traditional formulation of QRPA. In short, FAM lowers the barrier to performing large-scale QRPA studies, like the ones performed in this thesis. We give a first estimation of the order of magnitude of the QRPA correlation energies in EDF, with the future goal of adapting fitting protocols of effective interactions to account for QRPA correlation in the ground state.

This thesis

In this thesis, we focus on the extensive use of QRPA in its FAM formulation to produce E1-strength functions. Both the covariant EDF DD-PC1 and two different chiral interactions are used. This results in new global studies that explicitly take into consideration both paring and nuclear deformation. This constitutes the second global deformed-QRPA study up to date and the first chiral-QRPA study to treat all even-even nuclei for which there is experimental GDR data up to iron. Additionally, a new iterative algorithm to solve the QRPA equation for a few eigenvectors has been developed. Finally, a study on the ground state of QRPA is presented, with a new protocol to correct the well-known problem of double counting in QRPA ground state energies. The thesis is organized as follows:

- In **part 1** the QRPA formalism is presented. *Chapter 1* focuses on the formulation of QRPA from HFB, stressing its link to linear response theory. In *chapter 2*, the use of QRPA to calculate γ-strength functions is explained, alongside the Finite Amplitude Method (FAM).

- **Part 2** covers the different systematic studies of E1-strength functions performed in this thesis. In *chapter 3*, the covariant EDF DD-PC1 is used to perform calculations throughout the nuclear chart. Having access to a complete set of strength functions, the effect of deformation and shell closures on the response is studied. Extensive comparison to experimental data is done, with the strength in odd nuclei being calculated via an interpolation procedure. In *chapter 4* we show the results of the first systematic study of QRPA responses with chiral interactions for nuclei with mass up to iron. The chiral convergence of the QRPA response is assessed, and different chiral interactions are compared. Finally, in *chapter 5* the first-ever results of chiral QRPA using a triaxially deformed mean-field are presented, with calculations for ^{32}S and ^{24}Mg. We show that the chiral interaction from reference [29] produces an α-clustered solution for the HFB ground state of ^{24}Mg, compare the strength and characterize the importance of introducing triaxial deformation to reproduce experimental data.

- **Part 3** covers the new numerical and formal developments achieved in this thesis in the context of QRPA. This includes exploratory studies, where new methods are proposed that could be useful in future systematic studies. In *chapter 6* a new method is developed to obtain QRPA eigenstates in a fast way without having to build explicitly the QRPA matrix. This is done by using FAM to implement the Jacobi-Davidson algorithm for the very fast evaluation of QRPA eigenstates. This method shares a lot of the philosophy of the Arnoldi

method [62], while using FAM to evaluate the matrix-vector product of the *inverse* QRPA matrix. Its numerical performance is discussed, and several results are shown. To close the thesis, *chapter 7* deals with the question of the QRPA ground state. Several works exist [72, 73] citing the importance of correcting for double counting in the QRPA ground state. While several procedures have been proposed for the RPA case, no simple method has been developed for QRPA. In this chapter, we propose one by extending the prescription of [73] to the QRPA case, obtaining a simple formula to correct QRPA correlation energies.

Chapters are written so that they can be read independently, with the exception perhaps of chapter 2. To this aim, redundancy is preferred over ambiguity. The author has preferred to provide a succinct introduction of the theory rather than a full re-derivation. That way more emphasis is put into the original results of this thesis.

Part I

Theoretical background of QRPA

Chapter 1

The quasiparticle random phase approximation (QRPA)

In the field of nuclear structure, one aims at both a theoretical description of the ground state of the nucleus and its excitations. Ideally, the full description of the nucleus is obtained by diagonalizing the A-particle nuclear Hamiltonian exactly, with the ground state constituting the lowest-lying eigenstate. However, it is common practice to model the ground state as a wave function of independent nucleons embedded in a mean-field that results from the averaged interaction that each nucleon has with all the others. These kinds of methods are historically referred to as *mean-field-methods*. In the case of nuclear *Energy Density Functional* (EDF) theory, this state is meant to give a reliable description of the nuclear wave-function [5], with further correlations captured by an *effective internucleonic potential*, whose analytic form is proposed as an ansatz and whose parameters are fitted to experimental data. On the other hand, in the so-called *ab initio* methods, the mean-field wave function is taken as a first-order description in a series that converges towards the exact nuclear wave function while using a realistic interaction rooted in QCD [26]. The most general mean-field method is *Hartree-Fock-Bogolyubov* (HFB), which allows reproducing both long-range *particle-hole* correlations and *pairing* properties in nuclei, the latter being a key ingredient for a successful description of open-shell nuclei.

While HFB can give a relatively good description of the ground state, spectroscopic properties cannot be described as particle-hole excitations of the mean-field wave function alone. Many of the lowest-lying states in nuclei are collective states, which by definition require going beyond a single-particle picture, especially for even-even isotopes. *Quasiparticle Random Phase Approximation* (QRPA) is one of the conceptually simplest ways to describe both single-excitation and collective states built on top of an HFB state. In it, excited states are built as linear combinations of particle-hole (two-quasiparticle in the case of superfluid nuclei) excitations *and* deexcitations. This results in a generalized eigenvalue problem, which although very computationally heavy to solve, remains tractable.

In this chapter, we build QRPA from HFB. We show two different ways to derive the main equations of the formalism, which result in slightly different interpretations of the theory. The derivations presented follow the ones of the works [4, 5, 74].

1.1 Hartree-Fock-Bogolyubov

The main idea behind the Hartree-Fock-Bogolyubov (HFB) formalism is to describe the ground-state wave function of the nucleus as the vacuum of the *quasiparticle operators*, which are defined

as

$$\beta_\mu^\dagger = \sum_i U_{i\mu} c_i^\dagger + V_{i\mu} c_i, \tag{1.1}$$

with U and V complex matrices and $c^\dagger$, c are creation and annihilation[1] single-particle operators corresponding to an arbitrary basis[2] of the Hilbert space. If the resulting operators fulfill fermionic anticommutation rules

$$\left\{\beta_\mu, \beta_\nu^\dagger\right\} = \delta_{\mu\nu}, \quad \left\{\beta_\mu^\dagger, \beta_\nu^\dagger\right\} = 0. \tag{1.2}$$

then 1.1 is refered as a *Bogolyubov transform*. The anticommutation rules can be summarized in matrix form as

$$\begin{pmatrix}\beta & \beta^\dagger\end{pmatrix}\begin{pmatrix}\beta^\dagger \\ \beta\end{pmatrix} + \begin{pmatrix}\beta^\dagger & \beta\end{pmatrix}\begin{pmatrix}\beta \\ \beta^\dagger\end{pmatrix} = I, \tag{1.3}$$

where the unindexed $\beta, \beta^\dagger$ refer to vectors containing all the quasiparticle annihilation and creation operators

$$\begin{pmatrix}\beta & \beta^\dagger\end{pmatrix} = \begin{pmatrix}\beta_1 & \beta_2 \dots & \beta_N & \beta_1^\dagger & \beta_2^\dagger \dots \beta_N^\dagger\end{pmatrix}, \qquad \begin{pmatrix}\beta^\dagger \\ \beta\end{pmatrix} = \begin{pmatrix}\beta_1^\dagger \\ \beta_2^\dagger \\ \vdots \\ \beta_N^\dagger \\ \beta_1 \\ \beta_2 \\ \vdots \\ \beta_N\end{pmatrix}. \tag{1.4}$$

with N the total number of quasiparticle states. If we define the matrix

$$\mathcal{B} = \begin{pmatrix}U & V^* \\ V & U^*\end{pmatrix}, \tag{1.5}$$

we can then write the Bogolyubov transform as

$$\begin{pmatrix}\beta \\ \beta^\dagger\end{pmatrix} = \mathcal{B}\begin{pmatrix}c \\ c^\dagger\end{pmatrix}. \tag{1.6}$$

Then if the anticommutation rules are preserved, $\mathcal{B}$ is unitary $\mathcal{B}^\dagger\mathcal{B} = \mathcal{B}\mathcal{B}^\dagger = \mathbb{I}$. This leads to the following relations

$$\begin{aligned} U^\dagger U + V^\dagger V &= \mathbb{I}, \\ U^\intercal V + V^\intercal U &= 0, \\ U U^\dagger + V^* V^\intercal &= \mathbb{I}, \\ U V^\dagger + V^* U^\intercal &= 0. \end{aligned} \tag{1.7}$$

Let's now assume that there exists a *Hartree-Fock-Bogolyubov ground-state wave function* $|\mathrm{HFB}\rangle$ so that

$$\beta_\alpha |\mathrm{HFB}\rangle = 0 \quad \forall\alpha. \tag{1.8}$$

[1] Including both creation and annihilation operators breaks the particle-number symmetry. The breaking of fundamental symmetries of the Hamiltonian is a staple in EDF methods, and it is necessary to correctly capture enough correlations at the mean-field level.

[2] Generally solutions of the quantum harmonic oscillator

Thanks to this, we can define the density ρ and *anomalous density*[3] κ as

$$\rho_{ij} = \langle \text{HFB} | c_j^\dagger c_i | \text{HFB} \rangle , \quad \kappa_{ij} = \langle \text{HFB} | c_j c_i | \text{HFB} \rangle , \quad \kappa_{ij}^* = \langle \text{HFB} | c_i^\dagger c_j^\dagger | \text{HFB} \rangle , \tag{1.9}$$

It is easy to see that with this definition, the density and anomalous density are Hermitian and skew-symmetric respectively

$$\rho^\dagger = \rho, \quad \kappa^\intercal = -\kappa, \quad \kappa^\dagger = -\kappa^*. \tag{1.10}$$

Using equation 1.6, an inverse Bogolyubov transform can be obtained $\mathcal{B}^{-1} = \mathcal{B}^\dagger$. Writing the single-particle operators on the quasiparticle basis then

$$\rho = V^* V^\intercal, \quad \kappa = -U V^\dagger. \tag{1.11}$$

which, invoking the relations 1.7 gives

$$\rho^2 - \rho = \kappa\kappa^* \quad \rho\kappa = \kappa\rho^* \tag{1.12}$$

Thanks to these relations we can define the *generalized density matrix*,

$$\mathcal{R} = \begin{pmatrix} \rho & \kappa \\ -\kappa^* & 1 - \rho^* \end{pmatrix} \tag{1.13}$$

which, by virtue of equations 1.12, is idempotent

$$\mathcal{R}^2 = \mathcal{R}. \tag{1.14}$$

In the second quantization formalism, we can write a generic nuclear Hamiltonian with a two-body[4] density-dependent[5] interaction $\bar{v}_{ijkl}[\rho]$ as

$$H = \sum_{ij} t_{ij} c_i^\dagger c_j + \frac{1}{4} \sum_{ijkl} \bar{v}_{ijkl}[\rho] c_i^\dagger c_j^\dagger c_l c_k \tag{1.15}$$

We can define an energy functional by contracting the Hamiltonian with the HFB ground state. Applying Wick's theorem [4], then

$$E[\rho, \kappa, \kappa^*] = \langle \mathbf{HFB} | H | \mathbf{HFB} \rangle = \text{Tr}\left\{ t\rho + \frac{1}{2}\Gamma\rho - \frac{1}{4}\Delta\kappa^* - \frac{1}{4}\Delta^*\kappa \right\}. \tag{1.16}$$

Where introduce the *mean-field* Γ and *pairing* Δ matrices, which are defined as

$$\Gamma_{ij} = \sum_{kl} \bar{v}_{ikjl}\rho_{lk}, \quad \Delta_{ij} = \sum_{kl} \bar{v}_{ijkl}\kappa_{kl}. \tag{1.17}$$

For density-independent interactions, these correspond to the definition of the fields as

$$h_{ij} = \frac{\delta E}{\delta \rho_{ji}}, \quad \Delta_{ij} = \frac{\delta E}{\delta \kappa_{ij}^*}, \quad \Delta_{ij}^* = \frac{\delta E}{\delta \kappa_{ij}}, \quad h = t + \Gamma. \tag{1.18}$$

However, for density dependent-interactions, the mean-field Γ has to be modified with a *rearrangement* term

$$\Gamma \to \Gamma + \partial\Gamma, \quad \partial\Gamma_{ij} = \sum_{klmn} \frac{\delta \bar{v}_{knlm}}{\delta \rho_{ij}} \rho_{mn}\rho_{lk} \tag{1.19}$$

Now we have the building blocks for deriving the HFB equations. We would like to minimize the energy functional (1.16) with the constraint that:

[3] Also known as *pairing tensor*

[4] The formalism here laid out can be extended to three or more-body interactions.

[5] Although a density-dependent potential does not constitute a well-defined Hamiltonian, its use is widespread in the context of Energy Density Functionals, as it can take care of the interactions of nucleons with the nuclear medium without resorting to the introduction of three or more-body forces.

- The average number of particles for each isospin is Z, N, i.e.

$$\sum_{i_\nu} \frac{\langle \mathrm{HFB}| c^\dagger_{i_\pi} c_{i_\pi} |\mathrm{HFB}\rangle}{\langle \mathrm{HFB}|\mathrm{HFB}\rangle} = Z, \quad \sum_{i_\nu} \frac{\langle \mathrm{HFB}| c^\dagger_{i_\nu} c_{i_\nu} |\mathrm{HFB}\rangle}{\langle \mathrm{HFB}|\mathrm{HFB}\rangle} = N. \tag{1.20}$$

- The idempotency of the density matrix $\mathcal{R}$ is kept, i.e., $\mathcal{R}^2 = \mathcal{R}$, which means that the wave function is a vacuum of the quasiparticle states.

Using the Lagrange-multiplier method, this is equivalent to the minimization of the free energy

$$F = E[\rho, \kappa, \overline{\kappa}] - \mathrm{Tr}\left(\Lambda(\mathcal{R}^2 - \mathcal{R})\right) - \lambda_\pi \mathrm{Tr}_\pi \rho - \lambda_\nu \mathrm{Tr}_\nu \rho. \tag{1.21}$$

The variation of the energy functional plus the chemical potential λ terms gives

$$\delta\left(E[\rho, \kappa, \overline{\kappa}] - \lambda \,\mathrm{Tr}\,\rho\right) = \mathrm{Tr}\left(\mathcal{H}\delta\mathcal{R}\right), \tag{1.22}$$

with

$$\delta\mathcal{R} = \begin{pmatrix} \delta\rho & \delta\kappa \\ -\delta\kappa^* & -\delta\rho^* \end{pmatrix}, \quad \mathcal{H} = \begin{pmatrix} h - \lambda & \Delta \\ -\overline{\Delta} & -h^* + \lambda \end{pmatrix}. \tag{1.23}$$

By taking the full variation of the free energy δF, one obtains

$$\mathcal{H} = \Lambda\mathcal{R} + \mathcal{R}\Lambda - \Lambda, \tag{1.24}$$

which using $\mathcal{R}^2 = \mathcal{R}$ can be written as

$$[\mathcal{H}, \mathcal{R}] = 0, \tag{1.25}$$

Now, thanks to 1.12 it is easy to prove that in the quasiparticle basis, the generalized density $\mathcal{R}$ has the simple form

$$\mathcal{B}^\dagger \mathcal{R} \mathcal{B} = \begin{pmatrix} 0 & 0 \\ 0 & I \end{pmatrix}, \tag{1.26}$$

which is diagonal, which means that by equation (1.25), the HFB basis also diagonalizes the $\mathcal{H}$ matrix. This results in the *Hartree-Fock-Bogolyubov equation*

$$\begin{pmatrix} h - \lambda & \Delta \\ -\Delta^* & -h^* + \lambda \end{pmatrix} \begin{pmatrix} U_\mu \\ V_\mu \end{pmatrix} = E_\mu \begin{pmatrix} U_\mu \\ V_\mu \end{pmatrix}, \tag{1.27}$$

where U_μ and V_μ stand for the column vector $U_\mu = \begin{pmatrix} U_{1\mu} & U_{2\mu} & \dots & U_{I\mu} \end{pmatrix}^\intercal$. One can check that if U_i, V_i is a solution of the HFB equation with energy E_i, then V_i^*, U_i^* is also a solution with energy $-E_i$, This allows us to write equation 1.27 as

$$\mathcal{B}^\dagger \mathcal{H} \mathcal{B} = \begin{pmatrix} E & 0 \\ 0 & -E \end{pmatrix} \tag{1.28}$$

where E refers to the diagonal matrix with all the single quasiparticle energies.

1.1.1 Hamiltonian in the quasiparticle basis

After solving equation(1.27), we have a set of quasiparicle states. We can then express the general two-body Hamiltonian (1.15) in the quasiparticle basis

$$H = H^0 + H^{11} + H^{20} + H^{02} + H^{22} + H^{31} + H^{13} + H^{40} + H^{04}. \tag{1.29}$$

in which each superindex of the different terms stands for the number of quasiparticle creation (left) and annihilation (right) operators, e.g.

$$H^{11} = \sum_{ij} H^{11}_{ij}\beta^\dagger_i\beta_j, \quad H^{20} = \frac{1}{2}\sum_{ij} H^{20}_{ij}\beta^\dagger_i\beta^\dagger_j, \quad \dots \tag{1.30}$$

The HFB matrix can be written with the terms of the Hamiltonian in the quasiparticle basis

$$\mathcal{B}^\dagger\mathcal{H}\mathcal{B} = \begin{pmatrix} H^{11} & H^{20} \\ -H^{02} & -H^{11\intercal} \end{pmatrix} = \begin{pmatrix} E & 0 \\ 0 & -E \end{pmatrix}, \tag{1.31}$$

which means that the H^{20} and H^{02} terms vanish for the HFB solution and H^{11} become diagonal. We can then write 1.29 as

$$H = E_{\text{HFB}} + \sum_\mu E_\mu\beta^\dagger_\mu\beta_\mu + H_{int} \tag{1.32}$$

with H_{int} standing for the remaining terms with more than 2 quasiparticle operators.

1.1.2 Zero-pairing limit: Hartree-Fock

For a closed-shell nucleus, there is an unambiguous zero-pairing limit for the quasiparticle operators, which corresponds to the *Hartree-Fock* solution. This is obtained for a vanishing pairing density $\kappa \to 0$. In this case equation (1.25) becomes

$$[h, \rho] = 0. \tag{1.33}$$

This is automatically achieved if either the U or V coefficients are set to zero for each quasiparticle state. The particle operators can then be written like

$$a^\dagger_\alpha = \sum_i D_{i\alpha}c^\dagger_i, \tag{1.34}$$

which relate to the quasiparticle operators as

$$\beta^\dagger_i = \begin{cases} a^\dagger_p, & \text{for } E_i > \epsilon_F, \\ a_h, & \text{for } E_i \leq \epsilon_F. \end{cases} \tag{1.35}$$

with ϵ_F being the Fermi energy, i.e. the single particle energy of the last occupied state. As there is no longer mixing between creation and annihilation operators, particle number symmetry is not broken. The HF ground state can be then written like

$$|\mathbf{HF}\rangle = \prod_h a^\dagger_h|0\rangle\,. \tag{1.36}$$

1.2 Quasiparticle Random Phase approximation

HFB gives a reasonable first approximation of the nuclear ground state. However to get access to excited states, we need to go a step beyond, as two-quasiparticle excitations over the HFB state are not sufficient to describe the disparate nature of many of the nuclear excitations, many of them being highly collective. QRPA provides a method that allows the description of such states simply while also going beyond the independent-quasiparticle description. QRPA is used to describe states that can be understood as *small vibrations of the densities around the equilibrium shape*, while large-amplitude vibrations and rotations not being correctly characterized by it [4, 5]. Nevertheless, the fact that QRPA provides an unambiguous spectrum as long as it is used on top of an HFB state that minimizes the energy functional has made it a pretty popular method.

In this chapter, we present two different derivations of the QRPA equations: the linear response and the equations of motion method (sections 1.2.1 and 1.2.2 respectively).

1.2.1 Derivation from the linear response

One of the ways to derive QRPA is from the linear response formalism, which studies the evolution of a system under a weak external field. This particular formulation will allow us to make a bridge with the Finite amplitude method (FAM), which is laid out in chapter 2.

Starting from a generic 2-body Hamiltonian, let's introduce a perturbative term $F(t)$ representing the action of a time-dependent external field[6] on the nucleus

$$H \to H(t) = H + F(t), \tag{1.37}$$

which we assume to be a stationary harmonic perturbation of frequency ω

$$F(t) = F(\omega)e^{-i\omega t} + F^\dagger(\omega)e^{+i\omega t}. \tag{1.38}$$

In this work, the operator is taken as a one-body particle-number conserving Hermitian operator, so that

$$F(t) = \sum_{ij} f_{ij}(t) c_i^\dagger c_j. \tag{1.39}$$

This operator can be written in a matrix form as (see appendix A)

$$F(t) = f_0(t) + \frac{1}{2}\begin{pmatrix} c^\dagger & c \end{pmatrix} \underbrace{\begin{pmatrix} f(t) & \\ & -f^{\intercal}(t) \end{pmatrix}}_{\equiv \mathcal{F}^{\text{s.p.}}} \begin{pmatrix} c \\ c^\dagger \end{pmatrix} = f_0 + \frac{1}{2}\begin{pmatrix} \beta^\dagger & \beta \end{pmatrix} \underbrace{\begin{pmatrix} F^{11}(t) & F^{20}(t) \\ -F^{02}(t) & -F^{11\,\intercal}(t) \end{pmatrix}}_{\equiv \mathcal{F}^{\text{q.p.}}} \begin{pmatrix} \beta \\ \beta^\dagger \end{pmatrix} \tag{1.40}$$

where s.p. and q.p. refer to the operators written in the single particle and quasiparticle basis respectively. To transform the operators from one basis to the other, the transformation used is

$$\mathcal{B}^\dagger O^{\text{s.p.}} \mathcal{B} = O^{\text{q.p.}} \tag{1.41}$$

with O a generic operator matrix. Under the influence of the external perturbation $F(t)$, the single particle density is also modified

$$\mathcal{R} \to \mathcal{R}(t) = \mathcal{R}_0 + \delta\mathcal{R}(t), \tag{1.42}$$

$\mathcal{R}_0$ being the static HFB generalized density derived in the previous section. We can assume that at the equilibrium condition, the generalized density $\delta\mathcal{R}(t)$ follows the same time-evolution as the perturbation operator (1.38) i.e.

$$\delta\mathcal{R}(t) = \delta\mathcal{R}(\omega)e^{-i\omega t} + \delta\mathcal{R}^\dagger(\omega)e^{+i\omega t} \tag{1.43}$$

An important consideration in the linear response theory is that the generalized density matrix remains idempotent for all times so that the modified state remains an HFB state

$$\mathcal{R}^2(t) = \mathcal{R}(t), \forall t \tag{1.44}$$

We can then substitute here 1.42 and take only linear terms[7]. This yields

$$\delta\mathcal{R}(t)\mathcal{R}_0 + \mathcal{R}_0\delta\mathcal{R}(t) = \delta\mathcal{R}(t). \tag{1.45}$$

[6] The goal of this work is to model γ-transitions between the excited states and the ground state. Thus F will take the form of the electromagnetic multipole operator

[7] This and considering that the density remains idempotent are the two main approximations of QRPA. They are equivalent to the quasiboson approximation that is introduced in the equations of motion method.

In the quasiparticle basis, the static generalized density $\mathcal{R}_0$ has the form of equation 1.26. This implies that only the $\beta^\dagger\beta$ and $\beta\beta^\dagger$ are non-zero on such basis, obtaining

$$\delta\mathcal{R}(t) = \begin{pmatrix} 0 & W(t) \\ -W^*(t) & 0 \end{pmatrix}, \quad \text{q.p. basis} \tag{1.46}$$

where we have used the fact that $W(t)$ must be antisymmetric for $\mathcal{R}(t)$ to represent a fermionic density. By setting

$$W_{\mu\nu}(t) \equiv X(\omega)_{\mu\nu}e^{-i\omega t} + Y^*(\omega)_{\mu\nu}e^{+i\omega t} \tag{1.47}$$

one obtains

$$\delta\mathcal{R}(t) = \underbrace{\begin{pmatrix} 0 & X(\omega) \\ Y(\omega) & 0 \end{pmatrix}}_{\delta\mathcal{R}(\omega)} e^{-i\omega t} - \begin{pmatrix} 0 & Y^*(\omega) \\ X^*(\omega) & 0 \end{pmatrix} e^{i\omega t}. \tag{1.48}$$

Having established this, we would like now to solve the dynamics of the time-dependent generalized density $\mathcal{R}(t)$. In the Heisenberg picture, the time evolution of an operator $A(t)$ is determined by

$$i\partial_t A(t) = [H(t), A(t)] \tag{1.49}$$

Applying this to the quasiparticle states $\beta(t)$, we can derive the time-dependent HFB(TD-HFB) equation [4, 75]

$$i\partial_t\mathcal{R}(t) = [\mathcal{H}(t) + \mathcal{F}(t), \mathcal{R}(t)], \tag{1.50}$$

$\mathcal{H}(t)$ being the quasiparticle Hamiltonian matrix

$$\mathcal{H}(t) = \mathcal{H}[\mathcal{R}_0 + \delta\mathcal{R}(t)] = \mathcal{H}_0 + \delta\mathcal{H}(t), \tag{1.51}$$

with $\mathcal{H}_0$ being the HFB matrix of the static case (previous section). To obtain the linear response, we keep in 1.50 only the linear terms, which results in

$$i\partial_t\delta\mathcal{R}(t) = [\mathcal{H}_0, \delta\mathcal{R}(t)] + [\delta\mathcal{H}(t), \mathcal{R}_0] + [F(t), \mathcal{R}_0]. \tag{1.52}$$

By now taking explicitly the derivatives and keeping only the positive frequency terms, one obtains

$$\omega\delta\mathcal{R}(\omega) = [\mathcal{H}_0, \delta\mathcal{R}(\omega)] + [\delta\mathcal{H}(\omega), \mathcal{R}_0] + [F(\omega), \mathcal{R}_0] \tag{1.53}$$

The variation of the mean-field can be expressed as

$$\delta\mathcal{H}(\omega) = \begin{cases} \begin{pmatrix} \delta H^{11}(\omega) & \delta H^{20}(\omega) \\ -\delta H^{20}(\omega) & -\delta H^{11\intercal}(\omega) \end{pmatrix}, & \text{q.p. basis.} \\ \begin{pmatrix} \delta h(\omega) & \delta\Delta(\omega) \\ -\delta\Delta^*(\omega) & -\delta h^\intercal(\omega) \end{pmatrix}, & \text{s.p. basis.} \end{cases} \tag{1.54}$$

Expanding equation 1.53 in the quasiparticle basis gives

$$\omega\begin{pmatrix} 0 & X \\ Y & 0 \end{pmatrix} = \begin{pmatrix} 0 & EX + XE \\ -EY - YE & 0 \end{pmatrix} + \begin{pmatrix} 0 & \delta H^{20} \\ -\delta H^{02} & 0 \end{pmatrix} + \begin{pmatrix} 0 & \delta F^{20} \\ -\delta F^{02} & 0 \end{pmatrix} \tag{1.55}$$

Where the ω dependence was dropped for convenience. By checking component by component, two sets of equations are obtained

$$\boxed{\begin{aligned} (E_\mu + E_\nu - \omega)X_{\mu\nu}(\omega) + \delta H^{20}(\omega) &= -F^{20}(\omega) \\ (E_\mu + E_\nu + \omega)Y_{\mu\nu}(\omega) + \delta H^{02}(\omega) &= -F^{02}(\omega) \end{aligned}} \tag{1.56}$$

where an explicit ω dependence for the matrices is written as a reminder that these solutions only refer to a given frequency ω of the perturbation operator. These are the so-called *Finite amplitude method* equations. They will become useful in chapter 2 for the fast evaluation of γ-strength calculations. To make the equations simpler, the following condensed notation is introduced:

$$x = \begin{pmatrix} X(\omega) \\ Y(\omega) \end{pmatrix}, \quad \mathfrak{f} = \begin{pmatrix} F^{20}(\omega) \\ F^{02}(\omega) \end{pmatrix} \quad \delta\mathfrak{h} = \begin{pmatrix} \delta H^{20}(\omega) \\ \delta H^{02}(\omega) \end{pmatrix}, \quad \nu = \begin{pmatrix} I & 0 \\ 0 & -I \end{pmatrix} \quad \delta\mathfrak{h} = \begin{pmatrix} \delta H^{20}(\omega) \\ \delta H^{02}(\omega) \end{pmatrix}, \quad \epsilon = \begin{pmatrix} \varepsilon & 0 \\ 0 & \varepsilon \end{pmatrix} \tag{1.57}$$

Here ε is the diagonal matrix containing the energy of the quasiparticle pairs

$$\varepsilon = \begin{pmatrix} E_1 + E_2 & & & & & \\ & \ddots & & & & \\ & & E_1 + E_N & & & \\ & & & E_2 + E_3 & & \\ & & & & \ddots & \\ & & & & & E_{N-1} + E_N \end{pmatrix} \tag{1.58}$$

$x, f, \delta\mathfrak{h}$ are vectors of size N_{pairs} so that the each of the components corresponds to a quasiparticle pair with $\mu < \nu$. Then one can write the the FAM equation as

$$(\epsilon - \omega\nu)x + \delta\mathfrak{h} = -\mathfrak{f} \tag{1.59}$$

Now, one can also consider expressing the changes in the mean-field explicitly, i.e. [5, 74]

$$\delta H_{ab}(t) = \sum_{c \le d} \frac{\partial H_{ab}}{\partial \mathcal{R}_{cd}} \delta\mathcal{R}(t) \tag{1.60}$$

Substituting the resulting expressions in 1.56, one obtains

$$\boxed{\begin{pmatrix} \mathbf{A} & \mathbf{B} \\ \mathbf{B}^* & \mathbf{A}^* \end{pmatrix} \begin{pmatrix} X(\omega) \\ Y(\omega) \end{pmatrix} - \omega \begin{pmatrix} X(\omega) \\ -Y(\omega) \end{pmatrix} = - \begin{pmatrix} F^{20}(\omega) \\ F^{02}(\omega) \end{pmatrix}} \tag{1.61}$$

which is the so called *linear response equation*. It relates the perturbation operator F and its frequency ω to the change that it induces in the generalized density $\delta\mathcal{R}$, which is characterized by $X(\omega), Y(\omega)$. The $\mathbf{A}$ and $\mathbf{B}$ matrices are linear combinations of the interaction and the U and V quasiparticle coefficients. They fulfill

$$\mathbf{A}^\dagger = \mathbf{A}, \quad \mathbf{B}^\intercal = \mathbf{B} \tag{1.62}$$

By introducing

$$M = \begin{pmatrix} \mathbf{A} & \mathbf{B} \\ \mathbf{B}^* & \mathbf{A}^* \end{pmatrix} \tag{1.63}$$

then we can use our previously introduced notation to express the equation as

$$(M - \omega\nu)x = -\mathfrak{f} \tag{1.64}$$

By comparing to the condensed FAM equation (1.59), we see how the variation in the fields can be written in condensed notation as

$$(M - \epsilon)x = \delta\mathfrak{h} \tag{1.65}$$

Now that a theory of linear perturbations of the mean-field has been built one can ask oneself the question: What happens if the external field is turned off? If that is the case, the linear response equation becomes

$$\boxed{\begin{pmatrix} \mathbf{A} & \mathbf{B} \\ \mathbf{B}^* & \mathbf{A}^* \end{pmatrix} \begin{pmatrix} X^n \\ Y^n \end{pmatrix} = \omega_n \begin{pmatrix} X^n \\ -Y^n \end{pmatrix}} \tag{1.66}$$

This is the *QRPA equation*. The frequency ω_n and the X^n, Y^n coefficients have been scripted with an n to indicate that the equation has become an eigenvalue problem, so now ω is no longer a continuous variable but belongs to a discrete spectrum. If before the solutions were oscillations of the nuclear densities induced by an external field, now what is considered are oscillations of the densities induced by the nuclear field itself. The possible oscillatory solutions are quantized and thus are identified with the different excited states of the nucleus, each with energy $E_n = E_{\mathrm{GS}} + \omega_n$. In our condensed notation, the QRPA matrix becomes

$$Mx_n = \omega_n \nu x_n \tag{1.67}$$

The interpretation of the eigensolutions of the QRPA matrix as excited states becomes even more explicit in the derivation by the so-called equations of motion method, that we derive in the next section.

1.2.2 Derivation via the equations of motion

The equation of motion method is based on postulating that excited states can be modeled as excitation operators $Q_n^\dagger$ acting on the nuclear ground state of QRPA

$$|n\rangle = Q_n^\dagger |\mathbf{QRPA}\rangle\,, \tag{1.68}$$

with the excitation operator having the form

$$Q_n^\dagger = \frac{1}{2} \sum_{ab} X_{ab}^n \beta_a^\dagger \beta_b^\dagger - Y_{ab}^n \beta_b \beta_a. \tag{1.69}$$

This expression of the excitation operator is one of the simplest ways in which a collective excitation can be written. It merely consists of linear combinations of two-quasiparticle excitation and *deexcitations*, which allows to capture of additional correlations. We expect the Y amplitudes to be small, as they are, in a way, a measure of how much the QRPA ground state differs from the HFB one, which by construction should be similar in first order.

The equations of motion method consists of obtaining an explicit expression for X and Y by evaluating the identities

$$\begin{aligned} \langle \mathbf{QRPA}| \left[\beta_a^\dagger \beta_b^\dagger, \left[H, Q_n^\dagger\right]\right] |\mathbf{QRPA}\rangle &= \omega_n \langle \mathbf{QRPA}| \left[\beta_a^\dagger \beta_b^\dagger, Q_n^\dagger\right] |\mathbf{QRPA}\rangle \\ \langle \mathbf{QRPA}| \left[\beta_a \beta_b, \left[H, Q_n^\dagger\right]\right] |\mathbf{QRPA}\rangle &= \omega_n \langle \mathbf{QRPA}| \left[\beta_a \beta_b, Q_n^\dagger\right] |\mathbf{QRPA}\rangle \end{aligned} \tag{1.70}$$

which are known as the *equations of motion*. To evaluate the expectation values then one resorts to the *quasiboson approximation*, which consists in approximating $|\mathbf{QRPA}\rangle \approx |\mathbf{HFB}\rangle$ when evaluating 1.70. This approximation becomes an equality if one considers instead the quasiboson operator

$$Q_n^\dagger = \sum_\alpha X_\alpha^n A_\alpha^\dagger - Y_\alpha^n A_\alpha, \tag{1.71}$$

where we performed the substitution $\beta_a^\dagger \beta_b^\dagger \rightarrow A_\alpha^\dagger$, with $\alpha = a, b$ and $a > b$. The quasiboson operators $A^\dagger, A$ are then considered to obey bosonic commutation rules

$$\left[A_\alpha, A_\beta^\dagger\right] = \delta_{\alpha\beta}, \quad \left[A_\alpha^\dagger, A_\beta^\dagger\right] = 0, \tag{1.72}$$

and their vacuum is the HFB vacuum

$$A_\alpha \left|\mathbf{HFB}\right\rangle, \forall \alpha. \tag{1.73}$$

This allows us to interpret the QRPA operators $Q_n^\dagger$ as Bogolybov transformation of bosons, as the transformation 1.71 is formally identical to 1.1. Now, by considering the definition

$$\begin{aligned} A_{\alpha\beta} &= \langle \mathbf{QRPA} | \left[A_\alpha, \left[H, A_\beta^\dagger\right]\right] | \mathbf{QRPA} \rangle \\ -B_{\alpha\beta} &= \langle \mathbf{QRPA} | \left[A_\alpha, \left[H, A_\beta\right]\right] | \mathbf{QRPA} \rangle \end{aligned} \tag{1.74}$$

and evaluating the equations of motion, one obtains again the QRPA equation 1.66. For non-density dependent interactions, we can then express A, B matrices for $i > j$ and $k > l$ in terms of the quasiparticle Hamiltonian 1.29 as

$$A_{ijkl} = \varepsilon_{ijkl} + H^{22}_{ijkl} \quad B_{ijkl} = 4! H^{40}_{ijkl}, \tag{1.75}$$

with extra terms appearing for density-dependent interactions. Their complete expression can be found in, for example, reference [76].

1.2.3 Some properties of the QRPA eigensolutions

Being the solutions of a generalized eigenvalue problem, the solutions of the QRPA show several interesting properties. This arises mostly from the fact that M is Hermitian and positive definite [4]

Orthogonality of states

Theorem 1. *Let x_n, and x_m be eigensolutions of the QRPA equation associated to distinct QRPA eigenenergies $Mx_i = \omega_i \nu x_i$, for $i = n, m$. Then they are ν-orthogonal*

$$x_n^\dagger \nu x_m = 0 \tag{1.76}$$

Proof. We can prove this by checking

$$x_n^\dagger M x_m = \omega_m x_n^\dagger \nu x_m = \omega_n x_n^\dagger \nu x_m, \rightarrow x_n^\dagger \nu x_m = 0 \tag{1.77}$$

□

Remark. *By introducing the notation*

$$\mathbf{X} = \begin{pmatrix} X^1 & X^2 & \dots X^n \end{pmatrix} \quad \mathbf{Y} = \begin{pmatrix} Y^1 & Y^2 & \dots Y^n \end{pmatrix} \tag{1.78}$$

Then this translates into

$$\mathbf{Y}^\dagger \mathbf{X} = \mathbf{X}^\dagger \mathbf{Y} \tag{1.79}$$

Negative energy states

Theorem 2. *For each QRPA eigenstate $x_n = (X^n Y^n)$ with eigenenergy ω_n there exists another eigenstate with $\overline{x}_n = (Y^{n*} X^{n*})$ with opposite energy $-\omega_n$.*

Proof. The QRPA matrix is invariant under the transformation

$$\sigma M^* \sigma = M \tag{1.80}$$

with the matrix sigma defined as

$$\sigma = \begin{pmatrix} 0 & I \\ I & 0 \end{pmatrix} \tag{1.81}$$

Given that $\sigma \nu \sigma = -\nu$ and $\sigma^2 = I$, one can then see that

$$M x_n = \omega_n \nu x_n \rightarrow \sigma M^* \sigma \underbrace{\sigma x_n^*}_{\overline{x}_n} = \sigma \nu \sigma \underbrace{\sigma x_n^*}_{\overline{x}_n} \rightarrow M \overline{x}_n = -\omega_n \overline{x}_n \tag{1.82}$$

□

ν-norm of the states

Theorem 3. *The sign of the ν-norm of a given eigenvector $x_n \nu x_n$ coincides with the sign of the eigenvalue ω_n*

Proof. The fact that M is positive definite implies that $x_n M x_n > 0$. Then $x_n^\dagger M x_n = \omega_n x_n^\dagger \nu x_n > 0$ implies that ω_n and $x_n^\dagger \nu x_n$ have the same sign. □

Remark. *This allows us to define a normalization $x_n \rightarrow x_n / \sqrt{|x_n \nu x_n|}$, which by defining*

$$\mathcal{X} = \begin{pmatrix} \mathbf{X} & \mathbf{Y}^* \\ \mathbf{Y} & \mathbf{X}^* \end{pmatrix} \tag{1.83}$$

gives

$$\mathcal{X}^\dagger \nu \mathcal{X} = \nu \tag{1.84}$$

Which by using the fact that $\mathcal{X}^{-1} = \nu \mathcal{X}^\dagger \nu$, results in the relations

$$\begin{aligned} \mathbf{X}^\dagger \mathbf{X} - \mathbf{Y}^\dagger \mathbf{Y} &= I \\ \mathbf{X}^\dagger \mathbf{Y} - \mathbf{Y}^\dagger \mathbf{X} &= 0 \\ \mathbf{X}\mathbf{X}^\dagger - \mathbf{Y}^* \mathbf{Y}^\intercal &= I \\ \mathbf{X}\mathbf{Y}^\dagger - \mathbf{Y}^* \mathbf{X}^\intercal &= 0 \end{aligned} \tag{1.85}$$

which are equivalent to the relations 1.7, which is not surprising, as we had established that QRPA can be understood as a Bogolyubov transform of bosons.

Spurious QRPA states

Theorem 4. *For symmetry of the Hamiltonian H that is broken by the mean field, there is a zero-energy QRPA eigenpair.*

Proof. Let g be the generator of a symmetry group of the Hamiltonian so that

$$[H, g] = 0. \tag{1.86}$$

If g is not a symmetry of the mean field, then

$$[\mathcal{R}, g] \neq 0. \tag{1.87}$$

From equation 1.70, then if $\delta R \neq 0$, then $\omega_n = 0$. From (1.87) we know that $\delta \mathcal{R}$ cannot be zero, which proves that state exists. □

1.3 Conclusion and main formulae

In this chapter, QRPA has been built from HFB as a model able to describe excited states that account for internucleon correlations which are not present in HFB. This model will be used in the next chapters as the starting point for all the calculations.

In the following page, we show some reference tables summarizing the notation used. For concision, the ω dependence in the matrices is dropped.

Operator	Single particle basis	Quasiparticle basis
$\mathcal{H}$	$\begin{pmatrix} h & \Delta \\ -\Delta^* & -h^\intercal \end{pmatrix}$	$\begin{pmatrix} E & 0 \\ 0 & -E \end{pmatrix}$
$\delta\mathcal{H}$	$\begin{pmatrix} \delta h & \delta\Delta \\ -\delta\Delta^* & -\delta h^\intercal \end{pmatrix}$	$\begin{pmatrix} \delta H^{11} & \delta H^{20} \\ -\delta H^{02} & -\delta H^{11\intercal} \end{pmatrix}$
$\mathcal{R}$	$\begin{pmatrix} \rho & \kappa \\ -\kappa^* & 1-\rho^\intercal \end{pmatrix}$	$\begin{pmatrix} 0 & 0 \\ 0 & I \end{pmatrix}$
$\delta\mathcal{R}$	$\begin{pmatrix} \delta\rho & \delta\kappa \\ -\delta\overline{\kappa} & -\delta\rho^\intercal \end{pmatrix}$	$\begin{pmatrix} 0 & X \\ Y & 0 \end{pmatrix}$
$\mathcal{F}$	$\begin{pmatrix} f & 0 \\ 0 & -f^\intercal \end{pmatrix}$	$\begin{pmatrix} F^{11} & F^{20} \\ -F^{02} & -F^{11\intercal} \end{pmatrix}$

Equation	Traditional formulation	Condensed notation
QRPA equation	$\begin{pmatrix} \mathbf{A} & \mathbf{B} \\ \mathbf{B}^* & \mathbf{A}^* \end{pmatrix}\begin{pmatrix} X^n \\ Y^n \end{pmatrix} = \omega_n \begin{pmatrix} X^n \\ -Y^n \end{pmatrix}$	$Mx_n = \omega_n \nu x_n$
FAM equations	$(E_\mu + E_\nu - \omega)X_{\mu\nu}(\omega) + \delta H^{20}(\omega) = -F^{20}(\omega)$ $(E_\mu + E_\nu + \omega)Y_\nu(\omega) + \delta H^{02}(\omega) = -F^{02}(\omega)$	$(\epsilon - \omega\nu)x + \delta\mathfrak{h} = -\mathfrak{f}$
Linear response equation	$\begin{pmatrix} \mathbf{A} & \mathbf{B} \\ \mathbf{B}^* & \mathbf{A}^* \end{pmatrix}\begin{pmatrix} X(\omega) \\ Y(\omega) \end{pmatrix} - \omega \begin{pmatrix} X(\omega) \\ -Y(\omega) \end{pmatrix} = -\begin{pmatrix} F^{20}(\omega) \\ F^{02}(\omega) \end{pmatrix}$	$(M - \omega\nu)x = -\mathfrak{f}$

Chapter 2

Calculation of QRPA strength functions

In the previous chapter, the QRPA method, which models nuclear-excited states, was introduced. One of the main applications of QRPA has been the calculation of *γ-ray strength functions*, which are a measure of the probability of the nucleus to absorb an incident photon of a given energy [43]. Traditionally, the evaluation of strength functions has been made via the explicit diagonalization of the QRPA matrix. However, its high computational cost has limited its widespread use. In the last decade, the *finite amplitude method* has been developed, which solves the linear response equation without explicitly building the QRPA matrix [65, 66]. In this chapter, we present the finite amplitude method to calculate QRPA $\gamma-$ray strength functions.

2.1 Definition of the strength function

The γ-ray strength function $S(E;Q\lambda)$ associated to a given multi-polarity λ of the electromagnetic multipole expansion of the electromagnetic operator Q is related to the photoabsorption cross-section as

$$\sigma(E;Q\lambda) \propto \int_0^\infty dE\, S(E;Q\lambda) E^{2\lambda-1} \tag{2.1}$$

with the γ-ray strength function being defined as

$$S(E;Q\lambda) = \sum_n |\langle n|\, Q\lambda\, |\mathbf{GS}\rangle|^2 \delta(E - E_n). \tag{2.2}$$

Within the QRPA formalism, this quantity is readily available. Substituting in equation 2.2 the nuclear ground state by the QRPA one, and denoting the electromagnetic multipole operator as a generic perturbation F, then the QRPA strength function is defined as

$$S(E;F) = \sum_{n>0} |\langle n|\, F\, |\mathbf{QRPA}\rangle|^2 \delta(\omega_n - E) \tag{2.3}$$

where ω_n refers to the QRPA eigenenergies and $n > 0$ refers to the fact that we only sum over the positive energy states. The transition rates are evaluated within the quasiboson approximation, which gives

$$\langle n|\, F^\dagger\, |\mathbf{QRPA}\rangle = \frac{1}{2} \sum_{\mu\nu} \left(F^{20*}_{\mu\nu} X^n_{\mu\nu} + F^{02*}_{\mu\nu} Y^n_{\mu\nu} \right) = \mathrm{tr}\, \mathfrak{f}^\dagger x_n \tag{2.4}$$

In most of the applications, to compare with experimental data, the strength function 2.3 is convoluted with a normalized Lorentzian curve so that the evaluated strength function becomes

$$S(E;F) \to \sum_{n>0} |\langle n|\, F\, |\mathbf{QRPA}\rangle|^2 L(E;\omega_n,\Gamma) \equiv S(E;F,\Gamma/2) \tag{2.5}$$

were $L(E;\omega_n,\Gamma)$ stands for a Lorentzian distribution centered at ω_n and width at half-maxiumum Γ. Now, it can be proven [66, 67, 65] that the *not* smeared strength coincides with

$$S(E;F) = -\frac{1}{\pi}\lim_{\gamma\to 0}\mathrm{Im}\, I(\omega+i\gamma;F), \tag{2.6}$$

with I given with one of the following definitions, which can be proven to be equivalent

$$\begin{aligned} I(\omega,\gamma;F) &= \frac{1}{2}\sum_{\mu\nu} F^{20*}_{\mu\nu}X_{\mu\nu}(\omega+i\gamma) + F^{02*}_{\mu\nu}Y_{\mu\nu}(\omega+i\gamma) \\ &= \mathrm{tr}\Big\{\mathfrak{f}^\dagger x(\omega+i\gamma)\Big\} \\ &= \mathrm{tr}\Big\{f^\dagger \delta\rho(\omega+i\gamma)\Big\} \\ &= \sum_n \frac{|\langle n|\,F\,|\mathbf{QRPA}\rangle|^2}{\omega-E_n+i\gamma} - \frac{\left|\langle n|\,F^\dagger\,|\mathbf{QRPA}\rangle\right|^2}{\omega+E_n-i\gamma}, \end{aligned} \tag{2.7}$$

where we note that, except for the last line, *we refer to quantities calculated with the linear response equation evaluated at a complex energy* $\omega \to \omega + i\gamma$. It turns out that this strength is exactly the same as the one obtained via 2.6 but keeping γ at a finite value

$$S(E;F,\gamma) = -\frac{1}{\pi}\mathrm{Im}\, I(E+i\gamma;F) \tag{2.8}$$

This means that *by solving the linear response equation 1.61 at a complex energy* $\omega = E + i\gamma$ *we can obtain the QRPA strength at an energy* E *convoluted with a Lorentzian distribution of width at half-maximum* $\Gamma = 2\gamma$. The linear response equation can be evaluated in a fast manner via the Finite amplitude method, that we present now.

2.2 Finite amplitude method

In the finite amplitude method (FAM), one aims at solving the linear response equation

$$\begin{pmatrix}\mathbf{A} & \mathbf{B}\\ \mathbf{B}^* & \mathbf{A}^*\end{pmatrix}\begin{pmatrix}X(\omega)\\ Y(\omega)\end{pmatrix} - \omega\begin{pmatrix}X(\omega)\\ -Y(\omega)\end{pmatrix} = -\begin{pmatrix}F^{20}(\omega)\\ F^{02}(\omega)\end{pmatrix} \tag{2.9}$$

for a complex energy ω. This equation is completely equivalent to the FAM equation, that was derived in the previous chapter.

$$\begin{aligned} (\epsilon_\mu+\epsilon_\nu-\omega)X_{\mu\nu}(\omega) + \delta H^{20} &= -F^{20} \\ (\epsilon_\mu+\epsilon_\nu+\omega)Y_{\mu\nu}(\omega) + \delta H^{02} &= -F^{02} \end{aligned} \tag{2.10}$$

The key idea is to solve this equation iteratively. This can be achieved by the following steps, with a complex energy ω and a perturbation operator F:

1. Starting from an initial guess for the amplitudes X_0 and Y_0

$$\delta\mathcal{R}_0^{\text{q.p}} = \begin{pmatrix}0 & X_0\\ Y_0 & 0\end{pmatrix} \tag{2.11}$$

the induced densities are calculated as

$$\delta\mathcal{R}_0^{\text{s.p.}} = \begin{pmatrix}\delta\rho_0 & \delta\kappa_0\\ -\delta\kappa_0^* & -\delta\rho_0^{\mathsf{T}}\end{pmatrix} = \mathcal{B}\delta\mathcal{R}_0^{\text{q.p.}}\mathcal{B}^\dagger \tag{2.12}$$

2. With the induced densities, the induced fields are built via explicit linearization.[1] For a density-independent interaction, this amounts to

$$\delta h_{ij} = \sum_{kl} \bar{v}_{ikjl}\delta\rho_{lk}, \quad \delta\Delta_{ij} = \sum_{kl} \bar{v}_{ijkl}\delta\kappa_{kl}, \quad \delta\Delta^*_{ij} = \sum_{kl} \bar{v}_{ijkl}\delta\kappa^*_{kl}. \tag{2.13}$$

In the case of a density-dependent interaction, extra terms appear, but the philosophy is the same. In matrix form, the induced fields are

$$\delta\mathcal{H}_0^{\text{s.p.}} = \begin{pmatrix} \delta h_0 & \delta\Delta_0 \\ -\delta\Delta_0^* & -\delta h_0^\intercal \end{pmatrix} \tag{2.14}$$

3. The induced fields are transformed to the quasiparticle basis so that

$$\delta\mathcal{H}_0^{\text{q.p.}} = \begin{pmatrix} \delta H_0^{11} & \delta H_0^{20} \\ -\delta H_0^{20} & -\delta H_0^{11\,\intercal} \end{pmatrix} \tag{2.15}$$

4. The next iteration for the X and Y amplitudes is calculated via the FAM equation 1.56

$$\begin{aligned} \left[X_{\mu\nu}(\omega)\right]_1 + &= -\frac{F^{20}_{\mu\nu} + \left[\delta H^{20}_{\mu\nu}\right]_0}{(\epsilon_\mu + \epsilon_\nu - \omega)} \\ \left[Y_{\mu\nu}(\omega)\right]_1 + &= -\frac{F^{02}_{\mu\nu} + \left[\delta H^{02}_{\mu\nu}\right]_0}{(\epsilon_\mu + \epsilon_\nu + \omega)} \end{aligned} \tag{2.16}$$

so that

$$\delta\mathcal{R}_1^{\text{q.p}} = \begin{pmatrix} 0 & X_1 \\ Y_1 & 0 \end{pmatrix} \tag{2.17}$$

The process is repeated until convergence is achieved, i.e. $\left|\delta\mathcal{R}^{\text{q.p}}_{k+1} - \delta\mathcal{R}^{\text{q.p}}_k\right| <$`tol`, with `tol` a tolerance set by the user. With the obtained solution, the strength can be calculated by evaluating the quantity 2.8. Thus, calling the algorithm once at a given energy gives us the *folded* strength function calculated at such energy. The pseudocode of the FAM process can be seen in Algorithm 1. Solving FAM is substantially cheaper than filling and diagonalizing the QRPA matrix: the algorithm converges in 10-300 iterations while avoiding computing and storing the huge QRPA matrix.

2.2.1 GMRES method

While most of the implementations of the FAM algorithm use the Broyden iterations method [77] to achieve faster convergence, recently a new method to accelerate the FAM algorithm was developed [78], dubbed the GMRES method. It takes advantage of the fact that in all the steps of FAM, we are only performing linear transformation. Let's express the FAM equation in our condensed form

$$x_{k+1} = -\frac{1}{\epsilon - \omega\nu}\left(\delta\mathfrak{h} - \mathfrak{f}\right) \tag{2.18}$$

[1] In the first implementations of the FAM algorithm, the induced fields were calculated implicitly as $\delta h = \left(h\left[\mathcal{R} + \eta\delta\mathcal{R}\right] - h\left[\mathcal{R}\right]\right)/\eta$. This implies that the parameter η should be adjusted, which is avoided by explicit linearization.

Algorithm 1: Finite amplitude method-QRPA

Solves the linear response equation for a complex energy $\omega = E + i\gamma$ and calculates the QRPA response associated with an operator $\mathcal{F}$ at such energy built on top of an HFB state $\mathcal{B}$

Data: $\delta\mathcal{R}_0^{\text{q.p.}}, \omega, \gamma, \mathcal{F}, \mathcal{B}, k_{max}$,`tol`
Result: $\delta\mathcal{R}^{\text{q.p.}}, S(E,\gamma;\mathcal{F})$
$k \leftarrow 0$
while $k < k_{max}$ **do**
  $\delta\mathcal{R}_k^{\text{s.p.}} \leftarrow \mathcal{B}^\dagger \mathcal{R}_k^{\text{q.p.}} \mathcal{B}$;
  $\delta H_k^{\text{s.p.}} \leftarrow$ Result from equation using $\delta\mathcal{R}_k$;
  $\delta H_k^{\text{q.p.}} \leftarrow \mathcal{B}\delta H_k^{\text{s.p.}} \mathcal{B}^\dagger$;
  $\delta\mathcal{R}_{k+1}^{\text{q.p.}} \leftarrow$ result from FAM master equation (2.16);
  if $\left|\mathcal{R}_{k+1}^{\text{q.p.}} - \mathcal{R}_k^{\text{q.p.}}\right| <$`tol` **then**
    Solution found
    $\delta\mathcal{R}^{\text{q.p.}} = \delta\mathcal{R}_{k+1}^{\text{q.p.}}$
    $S(E,\gamma;F) \leftarrow$ strength calculated from equation 2.8;
    break ;
  $k \leftarrow k + 1$
end

As we said, obtaining the induced field $\mathfrak{f}$ from the previous iteration x involves only linear transformations. Multiplying $\mathfrak{f}$ by $(\epsilon - \omega\nu)^{-1}$ constitutes as well a linear transformation. This means that we can model them as a single operator $\mathbb{T}$ that acts over a given iteration x_k to account for all those transformations. Then one iteration of FAM amounts to

$$x_{k+1} = \mathbb{T}x_k - \underbrace{(\epsilon - \omega\nu)^{-1}\mathfrak{f}}_{\equiv \mathfrak{f}_0} \tag{2.19}$$

Convergence implies $x_{k+1} = x_k$, which results in the equation

$$(1 - \mathbb{T})x = -\mathfrak{f}_0 \tag{2.20}$$

With this, the FAM problem is turned into a system of linear equations, where $\mathbb{T}$ is not calculated exactly, but only its matrix-vector product is evaluated by performing all the steps listed before. Computationally, this is easy to solve using the iterative algorithm GMRES, which only requires the matrix-vector product of the matrix $\mathbb{T}$. As a part of this thesis, the GMRES-FAM algorithm has been implemented in the code `PAN@CEA`[79]. [2] This has been achieved using the GMRES implementation in the `eigen` linear algebra library. Figure 2.1 shows the number of iterations required to converge the FAM algorithm using Broyden mixing and GMRES for different values of the energy E and a constant $\gamma = 0.05$ MeV. Compared to Broyden mixing, GMRES is considerably fas8ter: around 3 times less iterations are needed in order to obtain the converged response. Additionally, its convergence pattern remains rather constant with the energy sampled, contrary to Broyden mixing, that shows some spikes in the number of FAM iterations.

In the rest of the thesis, FAM will be used to evaluate γ strength functions with different internucleonic potentials, focusing mostly on studying the $E1$ γ-transtion.

[2] The `PAN@CEA` code is a joint project between several CEA directions. It implements several many-body methods, between them QRPA-FAM, with Gogny and chiral interactions.

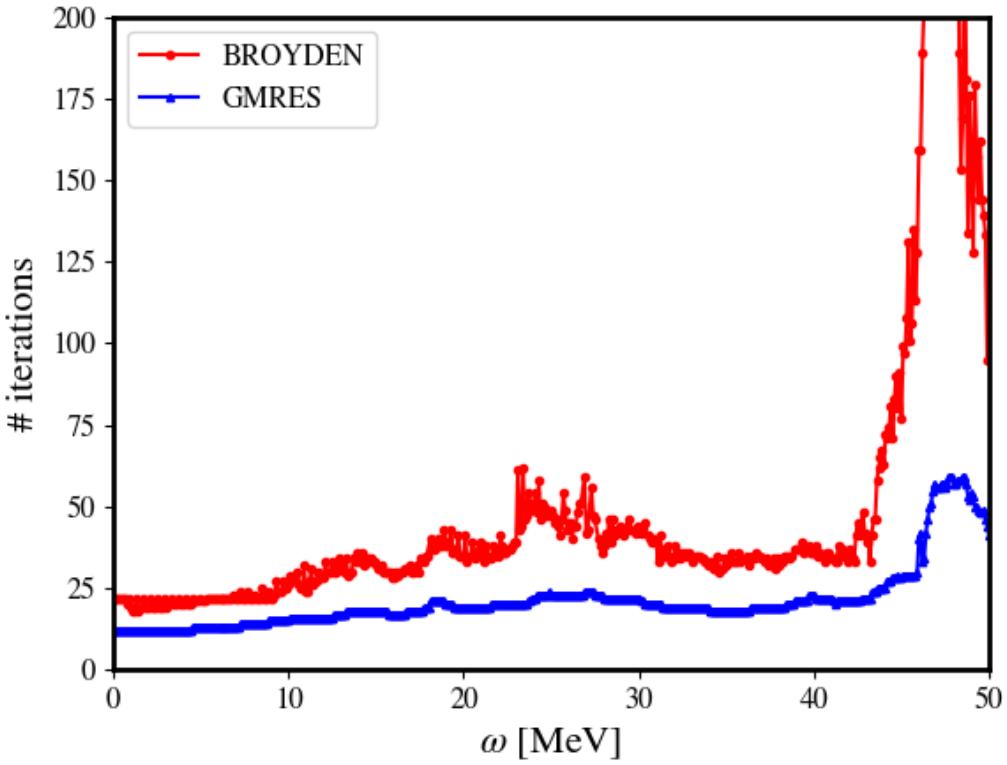

Figure 2.1: Iterations requiered for FAM to converge using the Broyden mixing and the GMRES algorithm for different values of the energy E and a constant $\gamma = 0.05$ MeV. The $E0$ response was calculated in ^{20}Ne with the interaction from reference [29] using 6 major harmonic oscillator shells.

Part II

Systematic QRPA studies

Chapter 3

Systematic QRPA calculations over all nuclei with covariant EDF

The photo-absorption cross-section is generally dominated by the $E1$ γ-transition. A correct characterization of this strength is thus essentail to model wide range of nuclear reactions, including those of importance for the r-process, which is responsible for the nucleosynthesis of a big portion of neutron-rich nuclei [40]. Despite their importance, the experimental measurements of strength functions are limited to a couple of hundred nuclei lying on the stability valley [43]. Their role as a fundamental ingredient of calculations of astrophysical interest has led to the development of a series of models trying to enlarge the information beyond the experimentally known data[44]. Although semi-empirical methods based on the use of analytical formulae such as the SMLO model [80, 45] are widely used, microscopic methods provide an increased predictive power that allows to study of more exotic parts of the nuclear chart. Valence space shell-model [81, 82] and PGCM [55] have been successfully used to describe γ-strength functions of different multipolarities for a restricted set of nuclei. However, up to date, the only microscopic method that has allowed for a systematic covering of the nuclear chart is QRPA. Currently, three QRPA γ-strength databases have been built and added to the `TALYS` reaction code [83], which we cite in chronological order: A first one using a series of Skyrme parametrizations [58, 59]. A second one using Relativistic mean-field + QRPA using the point coupling PCF1 Lagrangian [84]. Finally, a third one using the Gogny D1M interaction [60, 61, 85]. Of these three, only the last one uses a symmetry-breaking axially deformed mean-field, due mainly to the high computational cost of deformed calculations. For the other two, an empirical rule is used to reproduce the different peaks of deformed nuclei. In the three of them, empirical corrections are used *a posteriori* to better reproduce experimental data, which is justified by appealing to the missing physics of QRPA. This is especially the case for the low energy part of the $E1$ strength, as well as systematic shifts of the position of the maximum of the strength concerning experimental data.

In this chapter we show the results of a global study of $E1$ strength functions using the covariant DD-PC1 point coupling Lagrangian [24]. This constitutes the second time ever that a nuclear-chart-wide QRPA study has taken place using a deformed mean-field, and the first ever deformed covariant global study. To do so, we use the FAM-QRPA code `DIRQFAM` [86, 78]. This code is built on top of the relativistic-Hartree-Bogolyubov (RHB)[1] code `DIRHB` [87], and calculates the QRPA response on an axially deformed RHB state expanded in terms of eigensolutions of the quantum harmonic oscillator. The HO basis is transformed to the y-simplex basis, which makes it particularly efficient for the evaluation of electric responses. In the following pages, we show how

[1]The RHB formalism, although derived from an effective covariant Lagrangian plus a pairing EDF instead than an effective pseudopotential, results in a set of equations that are equivalent to the regular HFB case. We refer the reader to the references [17, 87, 5] for an in-depth review of the method.

to solve previously documented convergence issues with the code and compare the results with experimental photoabsorption data.

3.1 Optimization of the RHB state

As reported in reference [88], the mid-to-high energy-region of the strength functions generated with the `DIRQFAM` code do not converge with respect to the number of harmonic oscillator shells N_{HO}. In general, low-energy QRPA phonons are made up of just a few low-energy 2-quasiparticle excitations. However, the higher energy phonons, especially the ones making up the giant resonance, are very collective, made up of many individual 2qp excitations. Thus, small differences in the single-particle states add up, and they become more sensitive to the convergence of the underlying RHB state.

The `DIRQFAM` code implements the empirical formula [4, 89] for the harmonic oscillator frequency

$$\hbar\omega \approx 41A^{-1/3}\ \mathrm{MeV}, \tag{3.1}$$

which approximates rather well the mean-squared radius of the solutions of the harmonic oscillator potential to the measured data. An improved expression exists, the Blomqvist-Molinari formula [90], which reads

$$\hbar\omega \approx 45A^{-1/3} - 25A^{-2/3}\ \mathrm{MeV}. \tag{3.2}$$

However, when using EDFs with a wave function expanded in terms of HO eigensolutions, the mean-field solution is not necessarily optimized when using this value. This is our case with RHB calculations using the DD-PC1 Lagrangian. Figure 3.1 shows the dependence of the RHB binding energy for different numbers of major harmonic oscillator shells with respect to the oscillator frequency $\hbar\omega$. As is the case with HFB calculations with Gogny forces [11], several minima appear. For low values of $\hbar\omega$ a very pronounced minimum is observed. This is the case for all nuclei when a big enough number of shells is used. This minimum is very tight and the strength function calculated with a state on that minimum never converges. The former point is against the generally expected behavior of mean-field calculations, where the solution becomes independent of $\hbar\omega$ for a big enough space. Thus we can neglect such minimum as spurious. This is not the case for the minimum on the far-right of each curve, where we have a behavior that is more in line with what is expected. This minimum is not necessarily at the value given by the formula. In fact, in some cases, the RHB energy does not decrease with an increasing number of shells if the formula value is used, as illustrated in figure 3.2. For that reason, for the following of this work, the *physical* minimum is selected as the first minimum from the right.

The choice of this minimum is justified when launching a QRPA-FAM calculation starting from our optimized minimum, compared with using the original value for $\hbar\omega$. This is shown in figure 3.3. The results obtained using the empirical formula show the diverging behavior previously observed. However, for our optimized procedure, the strength function converges satisfactorily.

3.1.1 Global strategy

To be able to optimize the RHB state for all nuclei, the following procedure has been followed:

1. Starting with $\hbar\omega = 41A^{-1/3}$, potential energy surfaces were calculated with respect to the axial quadrupole deformation β_2. It is observed that in general, the position of the β_2 minimum does not depend dramatically on $\hbar\omega$, which justifies this step.

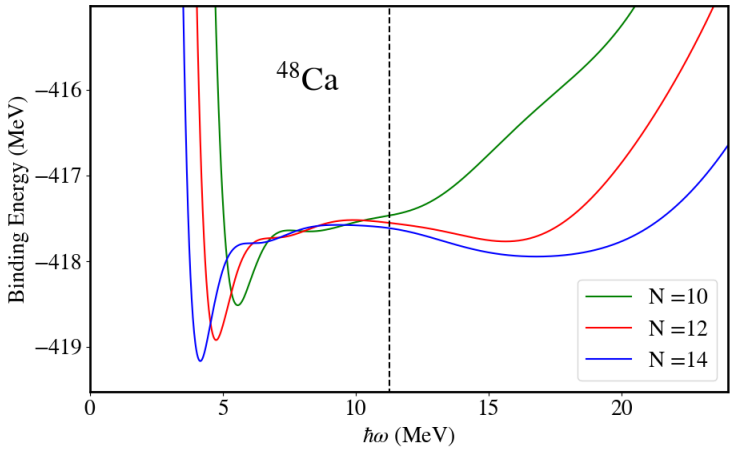

Figure 3.1: RHB binding energy as a function of the harmonic oscillator frequency $\hbar\omega$ for different sizes of the Harmonic Oscillator basis N_{HO} for ^{48}Ca. The dashed line corresponds to the value of the oscillator length given by $\hbar\omega = 41A^{-1/3}$. Figure taken from [91].

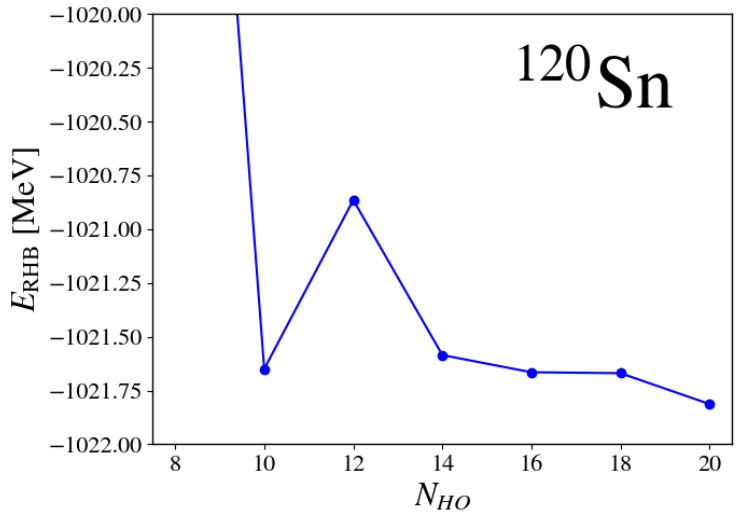

Figure 3.2: RHB binding energy as a function of the basis size for ^{120}Sn using the empirical formula for the harmonic oscillator frequency $\hbar\omega = 41A^{-1/3}$.

2. A curve of $\hbar\omega$ vs E_{RHB} like the one in figure 3.1 is calculated, with β_2 constrained to the minimum found in the previous step. The optimal $\hbar\omega$ is chosen as the first minimum from the right.

3. A second β_2 vs E_{RHB} potential energy surface is calculated, this time using the optimal $\hbar\omega$.

Following the example of AMEDEE [92], a maximum deformation of $\beta_2^{\max} = 0.75$ is chosen. The intervals $\beta_2 \in [-0.5, 0.5]$ and $\hbar\omega \in [2, 18]$ have been used for the PES calculations, with steps of $\Delta\beta_2 = 0.05$ and $\Delta\hbar\omega = 0.5$ respectively. For the last RHB calculation once the optimized minimum has been found, the constraint on β_2 is removed, and its optimal value is set as the initial deformation of the wave function. The model space size used is 14 harmonic oscillator shells for nuclei with $A < 100$, 16 for $100 < A < 150$, and 18 for the rest of the nuclei. However, for the nuclei for which those basis sizes are not enough for a clear physical minimum to appear, the number of shells is increased until it does. For the rare cases for which 20 harmonic oscillator shells are not enough, $\hbar\omega = 41A^{-1/3}$ and 20 shells are chosen.

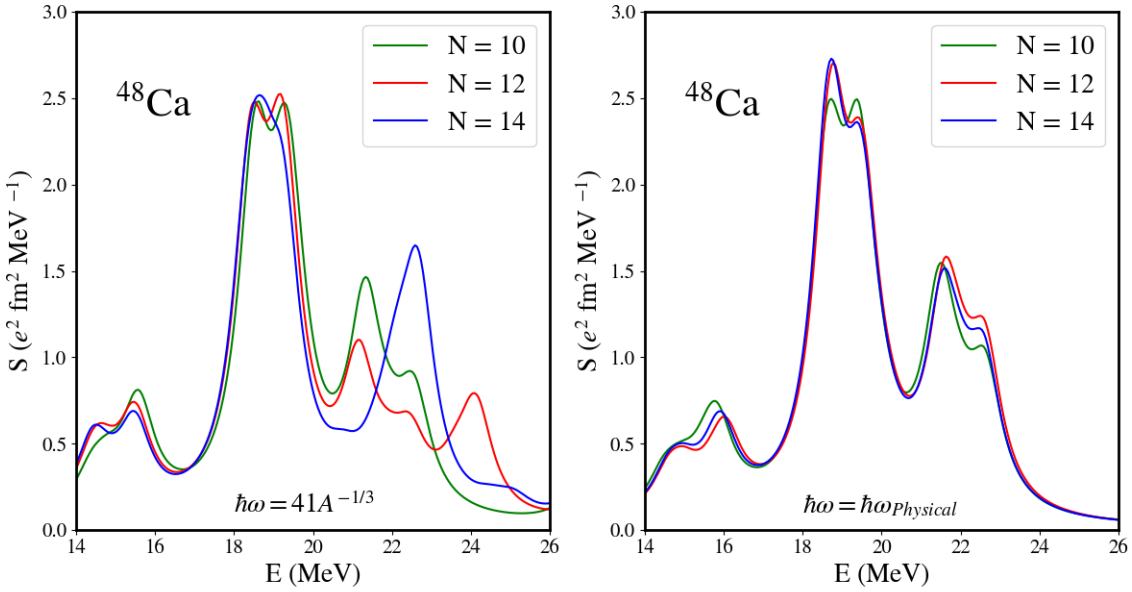

Figure 3.3: Evolution the E1 strength function in ^{48}Ca for different harmonic oscillator basis size with the default value of $\hbar\omega$ (left) and the one that minimizes the PES outside the spurious region (right). Figure taken from [91].

3.1.2 RHB results

In total, 1743 even-even nuclei were considered in our study. Figure 3.4 shows all nuclei, alongside the β_2 deformation of the RHB state predicted with the DD-PC1 Lagrangian, which is defined in terms of the expectation value of the quadrupole moment operator Q_{2M} as

$$\beta_2 = \frac{\sqrt{5\pi}}{3AR_0^2}\langle Q_{20}\rangle \tag{3.3}$$

with $R_0 = 1.2A^{1/3}$. The deformation landscape does not show a significant difference with the one obtained with Gogny D1M [92]: The changes in deformation are in general smooth, and safe for the small mass region. The nuclei are calculated from dripline to dripline from $Z \geq 6$, with it defined as the limit of negative two-nucleon separation energy.

Figure 3.5 shows the difference in calculated binding energies at RHB level to the experimental data compiled in the AME 2020 database [93, 94]. This database includes predictions for the masses of certain nuclei that were not measured experimentally. We did not include those in our analysis. The binding energies show big peaks corresponding to shell closures, as was already observed in reference [95]. Figure 3.6 shows the difference with experimental radii compiled in [96]. Charge-radii show an overall agreement up to 0.05 fm for most nuclei, with localized regions of bigger disagreement. To test whether our optimization procedure has a major impact on observables, table 3.1 shows the root mean square deviation to experimental data using our optimization procedure and using $\hbar\omega = 41A^{1/3}$. We can see that while binding energies have a slight improvement, charge-radii remain virtually identical. This is not in contradiction with the dramatic impact that it has on the QRPA response. As we will see in chapter 4, this is a general behavior of QRPA, which has to do with the amplifying effect that QRPA has on small static mean-field differences [97].

Having obtained an optimized RHB state for each nucleus, in the next section, we calculate the $E1$ QRPA response on top of it.

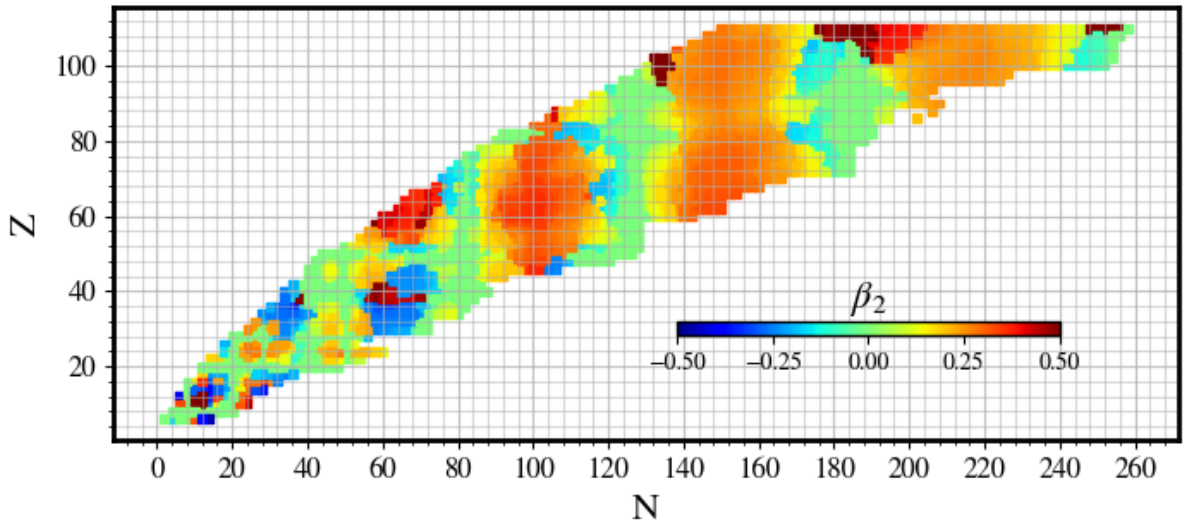

Figure 3.4: β_2 deformation calculated with the DD-PC1 relativistic Lagrangian for all nuclei considered in this work.

$\hbar\omega$ method	Optimized	Formula
ΔE_{rms} [MeV]	1.85	1.90
ΔR^c_{rms} [fm]	0.0339	0.0340

Table 3.1: Root mean square deviation of the binding energies and charge radii at RHB level calculated using the optimization procedure and with the empirical formula

3.2 Systematic E1 strength calculations with DD-PC1

In this project, the electric dipole strength is studied over the nuclear chart. This strength is characterized by taking as the perturbation the isovector electric dipole operator

$$F \rightarrow Q^{IV}_{1K}. \tag{3.4}$$

In general, the electric multipole operator for any multipolarity is written in the position basis as,

$$Q_{JK} = \sum_{i=1}^{A} f_{JK}(\mathbf{r}_i), \tag{3.5}$$

with

$$f(\mathbf{r}_i) = r_i^J Y_{JK}(\theta_i, \phi_i), \tag{3.6}$$

with $Y_{JK}(\rho, \varphi)$ the well known spherical harmonics. Specifically for the dipole isovector case, the operator takes the form

$$Q^{IV}_{1K} = e\frac{NZ}{A}\left[\frac{1}{Z}\sum_{i=1}^{Z} f_{1K}(\mathbf{r}_i) - \frac{1}{N}\sum_{i=1}^{N} f_{1K}(\mathbf{r}_i)\right]. \tag{3.7}$$

As the underlying RHB state is deformed, this means that the strength is split in two contributions, one for each projection of the total angular momentum projection, $K = 0$ and $|K| = 1$, so that

$$S^K_{E1}(E) = \sum_{n>0} \left|\langle nK|\, Q^{IV}_{1K}\, |\mathbf{QRPA}\rangle\right|^2 \delta(E - \omega_n) \tag{3.8}$$

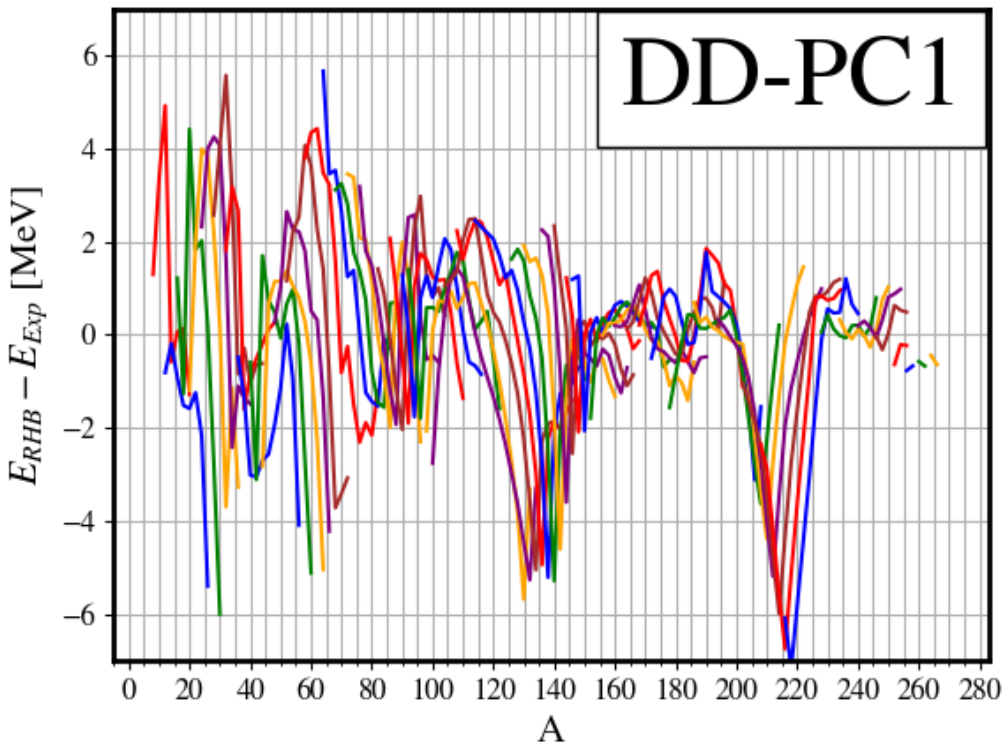

Figure 3.5: Difference between the binding energies of even-even nuclei calculated at RHB level with the DD-PC1 Lagrangian experimental data. Solid lines represent isotopic chains

The total strength is then calculated as $S_{E1}(E) = S_{E1}^{K=0}(E) + 2S_{E1}^{K=1}(E)$.

As we said before, being the dominant component of the photoabsorption cross-section, the calculation of $E1$ γ-strengths has been the main target of the other existing systematic QRPA studies [60, 61, 84, 58, 59]. Most of the sum-rule of the $E1$ response is exhausted by the giant isovector-dipole-resonance (GDR) [42], which is a vibrational mode where protons and neutrons oscillate against each other. There is a significant corpus of experimental data on the GDR, with the PSF database [43] having photonuclear data for 159 nuclei. A systematic rule for the energy average of the GDR exists [42], which reads

$$E_{GDR} = 31.2A^{-1/3} + 20.6A^{-1/6} \tag{3.9}$$

However, both sides beyond the stability valley remain uncharted territory, and only microscopic methods can give us some insight into the GDR landscape. In the following pages, we show the results of our new QRPA systematic study with the DD-PC1 interaction.

3.2.1 General considerations

To characterize the GDR, generally, its energy centroid and width are calculated. Within QRPA, these are calculated using the moments m of the operator characterizing the strength F, which are defined as [4]

$$m_k(F) = \sum_n E_n^k |\langle n| F |\mathrm{GS}\rangle|^2. \tag{3.10}$$

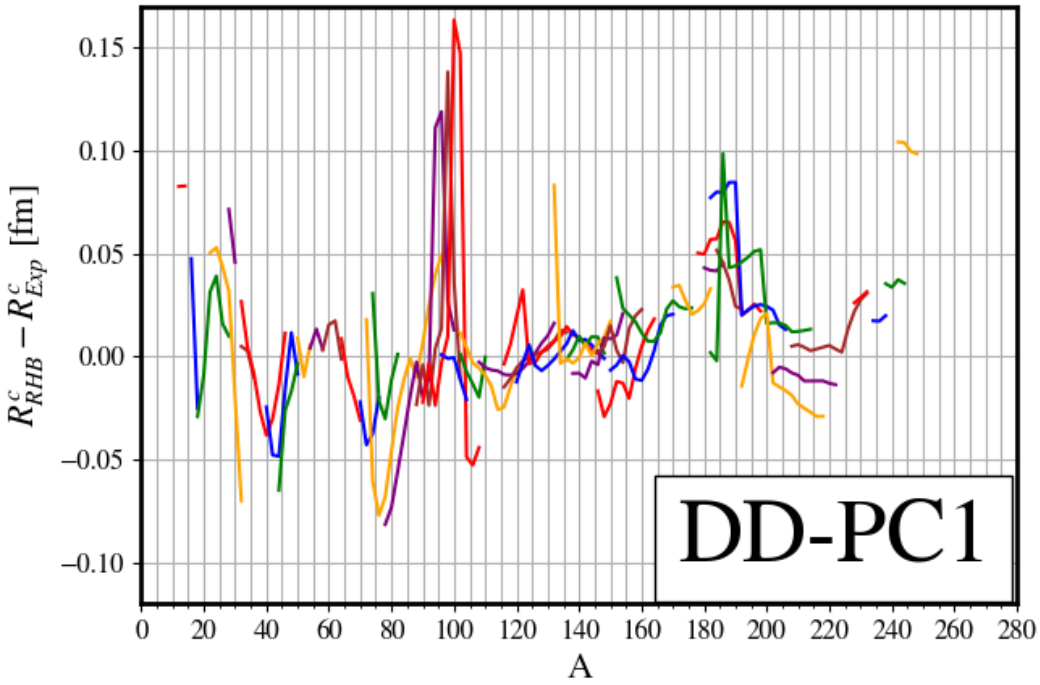

Figure 3.6: Difference between the charge radii of even-even nuclei calculated at RHB level with the DD-PC1 Lagrangian to experimental data from [96]. Solid lines represent isotopic chains

The centroid and width are then calculated as

$$\text{Centroid} = \frac{m_1}{m_0}, \quad \text{Width} = \sqrt{\frac{m_2}{m_0} - \left(\frac{m_1}{m_0}\right)^2}. \tag{3.11}$$

However, the giant resonance region shows a continuous spectrum in the strength. Thus, what is usually done to match theoretical predictions to experimental data is to convolute the discrete QRPA spectrum with a Lorentzian curve. In the present work, we use the FAM formulation of QRPA, where the FAM strength is immediately equivalent to the standard Lorentz-convoluted QRPA strength, as it was explained in chapter 2. The width of the Lorentz curve is $\Gamma = 2\gamma$, with γ being the imaginary part of the energy in FAM., Within this approach, it holds [68]

$$m_k(F) = \lim_{\gamma \to 0} \int_0^\infty dE\, E^k S_{FAM}(E; F, \gamma) \tag{3.12}$$

Nevertheless, due to practical considerations, and considering that the experimental data show a continuous spectrum, we will calculate the moments with the smeared strength function

$$m_k(F, \gamma) \equiv \int_0^{E_{max}} dE\, E^k S_{FAM}(E; F, \gamma), \tag{3.13}$$

with which we will calculate the centroids and widths. The following considerations are taken:

1. A constant $\gamma = 1.5$ MeV is chosen. This is justified by the good agreement with data that will be reviewed in section 3.2.4.

2. The strength functions are evaluated with a step of 0.1 MeV in an energy interval of [0,50] MeV.

The rather big smearing of the strength assures that most of the peaks are not lost by a small enough step.

3.2.2 Global results

The value for the centroids of the strength for all considered nuclei is shown in figure 3.7, alongside the predicted value for the GDR by the formula 3.9. We see that centroids in general follow the empirical rule. However, it is important to consider that although the GDR is the most important part of the $E1$ strength, there are other important components, such as the pigmy resonance. We can also observe that the centroids move softly within an isotopic chain. Table 3.2 shows the root mean square and mean deviations of the centroid and maximum of the strengths with the empirical formula. We can see that if we take the GDR energy as the centroid, it is in general overestimated, with a mean square deviation of a bit less than 1 MeV. The maxima seem to lie mostly below the value predicted by the rule, with a RMSD of around 1.3 MeV.

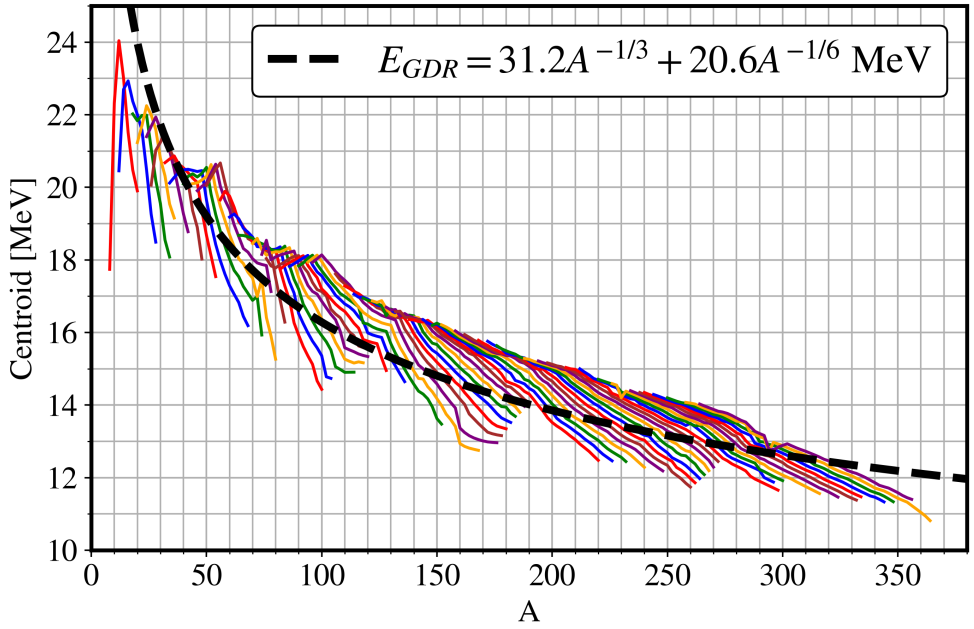

Figure 3.7: Position of the centroid for each nucleus as a function of the nuclear mass. The continuous lines represent each isotopic chain. The dashed line corresponds to the empirical rule for the position of the GDR.

$E1$ QRPA - GDR Formula			
Centroid		Maximum	
RMSD [MeV]	Mean deviation [MeV]	RMSD [MeV]	Mean [MeV] deviation
0.96	0.31	1.28	-0.75

Table 3.2: RMSD and mean deviation of the E1 centroid and maximum from the values predicted by the empirical formula 3.9 calculated with the DD-PC1 Lagrangian.

Widths are shown in figure 3.8. We can see that the strength function becomes narrower with increasing mass, with it reaching a mean value of around 5.5 MeV after $A = 100$, when most of the widths are contained within 5 and 6 MeV.

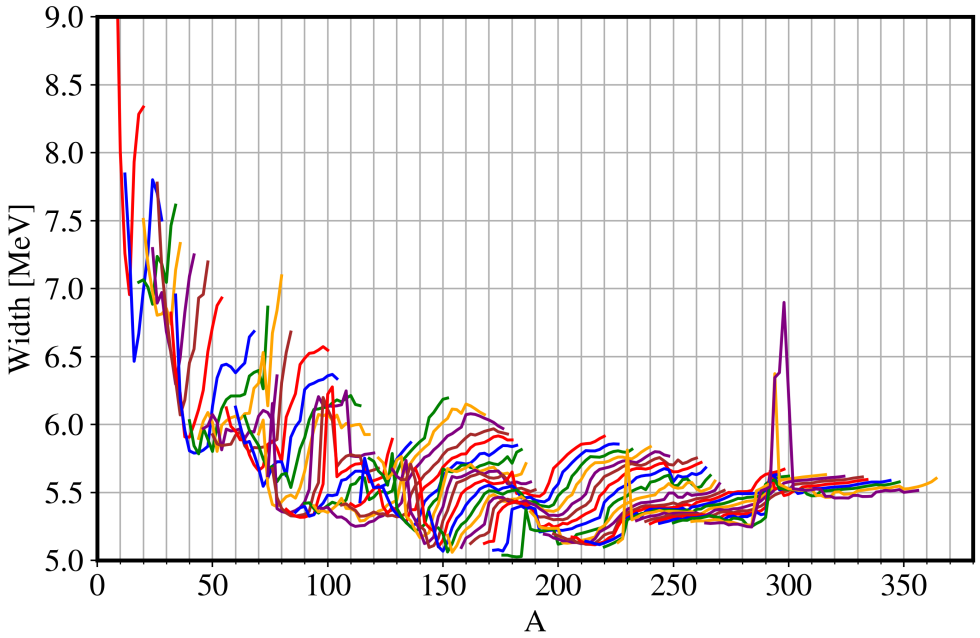

Figure 3.8: Width of the $E1$ strength for each nucleus as a function of the nuclear mass. The continuous lines represent each isotopic chain.

It is interesting to see which is the effect of shell closures on the bulk properties of the strengths. Figure 3.9 shows the position of the centroid as a function of the proton and neutron number. We can see that for both cases, shell closures bring a peak in the position of the strength functions. On the one hand, shell closure pushes the centroids of the strengths to higher energies. The effect on widths goes in the inverse direction, as we can see in figure 3.10, which are reduced which shell closures. In short, the strengths are pushed to higher energies and narrowed with shell closures. The reduced widths are explained by the fact that shell-closed nuclei show a reduced density of states with respect to their neighbors. On the other hand, with shell-closure excited states get pushed to higher energies, which explains the shift on the centroids.

3.2.3 Effect of the RHB deformation on the strengths

As we mentioned earlier, two of the existing QRPA databases [58, 59, 84] were created with a spherical basis. The splitting on the strength was then introduced by hand with the following rules [98]

$$3E_{E1} = E_{K=0} + 2E_{K=1} \tag{3.14}$$

$$E_{K=1}/E_{K=0} = 0.911\eta + 0.089 \tag{3.15}$$

Where η is the ratio of the diameters along the axis of symmetry to the diameter along a perpendicular axis. These rules, although formulated for the GDR region, are then applied to the full strength. Even though their success in reproducing experimental data is not questioned, proof that they can be derived from a microscopic principle is desirable. To do so, we study their applicability when considering the energies as the centroid energy and the maximum energy.

Figure 3.11 shows the value of the quantity $3E_{Total} - E_{K=0} - 2E_{K=1}$ with respect to the quadrupole deformation parameter β_2. This quantity should be 0 according to rule 3.14. When considering the maxima, it is not surprising that this does not yield 0, as the sum of two smeared strengths will usually result in a two-peaked strength. However, when considering the centroids, we see a clear

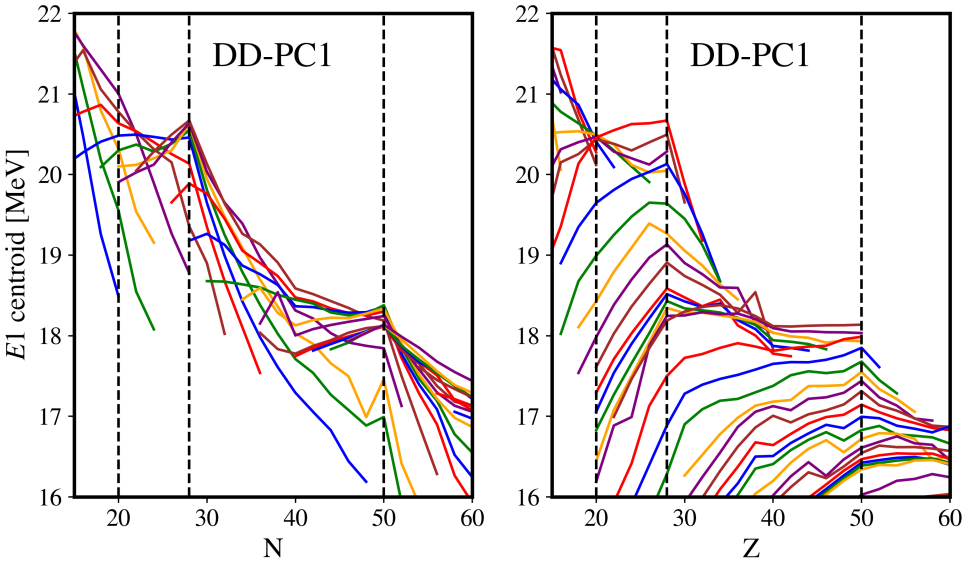

Figure 3.9: Position of the centroid for each nucleus as a function of the number of neutrons (left) and protons (right). The continuous lines represent each isotopic and isotonic chain respectively. The vertical dashed lines correspond to shell closures.

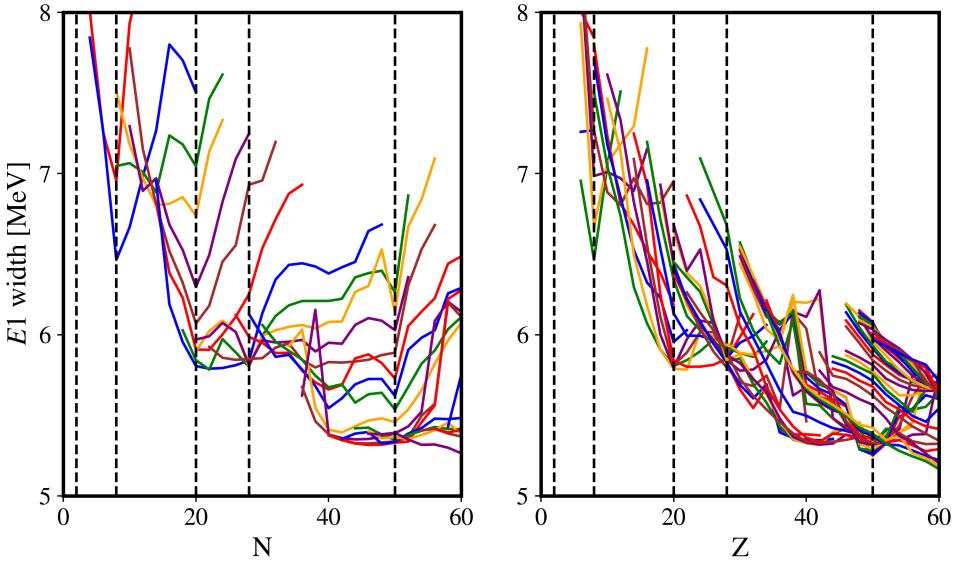

Figure 3.10: Width of the $E1$ strength for each nucleus as a function of the number of neutrons (left) and protons (right). The continuous lines represent each isotopic and isotonic chain respectively. The vertical dashed lines correspond to shell closures.

structure in the data. Up until a deformation of $|\beta_2| \approx 0.2$ the rule is fulfilled with a deviation of 0.25 MeV. However, there is a downward convex relation with the deformation, which means that the deviation to this rule is violated to a magnitude proportional to β_2^2. To validate 3.15, we plot on figure 3.12 the quotient between the energy of the $K = 1$ and $K = 0$ components of the strength with respect of the quadrupole deformation β_2, as it is intimately related to the η quotient. We find that indeed the results follow a linear distribution, with that being especially the case when considering

the strength centroids. The data of the centroids are fitted with a curve $(E_{K=1}/E_{K=0})_{\text{fit}} = \alpha\beta_2 + 1$, obtaining $\alpha = 0.735$.

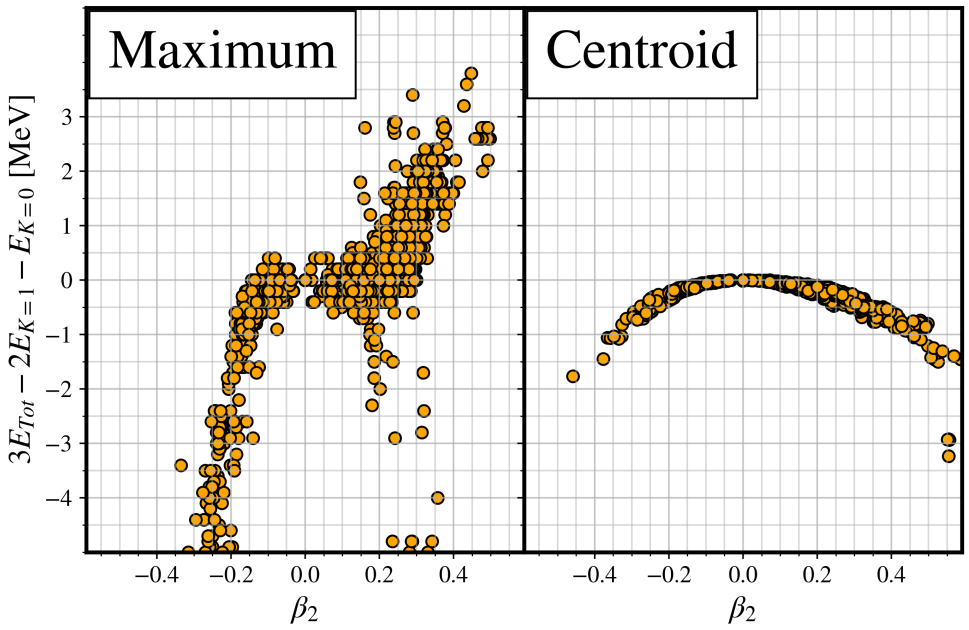

Figure 3.11: Value of the $3E_{\text{E1}} - E_{K=0} - 2E_{K=1}$ with respect of the β_2 deformation of the underlying RHB state. On the left, the energy of the resonance is taken as the maximum the strength, whereas on the left it is the centroid.

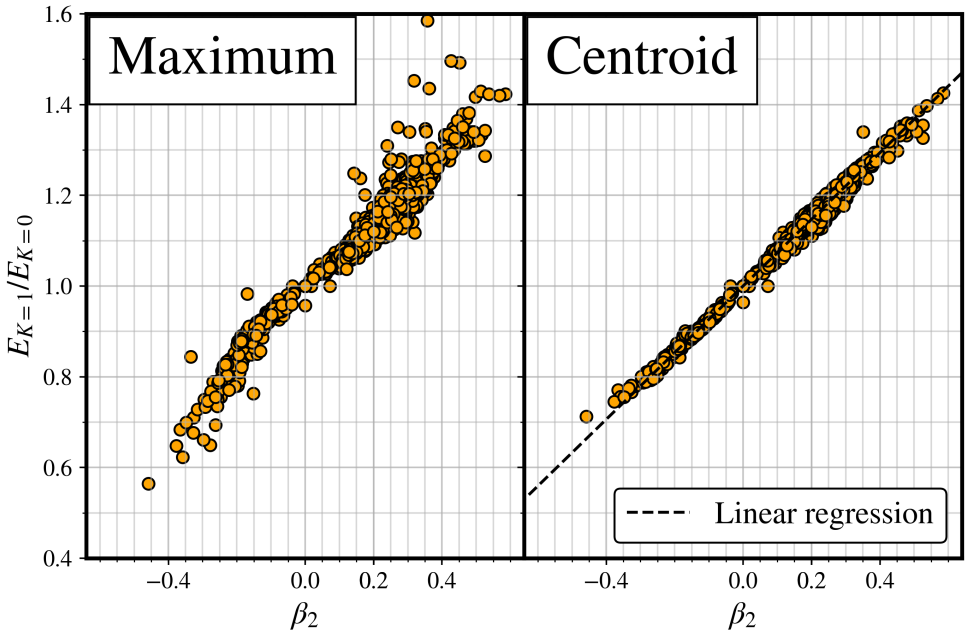

Figure 3.12: Value of the quotient of each of the components of the E1 strength $E_{K=1}/E_{K=0}$ with respect to the β_2 deformation of the underlying RHB state. On the left, the energy of the resonance is taken as the maximum of the strength, whereas on the left it is the centroid.

3.2.4 Comparison with photonuclear data

To compare the QRPA-FAM strength functions to photonuclear data, we must perform the following change of units [99]

$$f_{E1}\left[\mathrm{MeV}^{-3}\right] = \frac{1}{3\times 0.955\times 10^{6}}\left(S^{E1}_{FAM}(E,\gamma)\left[\mathrm{e}^{2}\mathrm{fm}^{2}\mathrm{MeV}^{-1}\right]\right). \tag{3.16}$$

A significant portion of the experimental data are odd nuclei. Although it is possible to calculate the response as them within the QRPA framework via blocking, in this work we use the approach used in reference [60], where the odd response is calculated as the geometric average of all the neighboring even-even nuclei. As an example, the strength of a nucleus with an odd number of neutrons, we have

$$S(E;Z,N) = \sqrt{S(E;Z,N+1)S(E;Z,N-1)}. \tag{3.17}$$

The results for nuclei with experimental data are plotted in figures 3.13-3.18. A first-sight good agreement between experimental data and our calculations is observed. We want to over-emphasize that apart from the interpolation of odd nuclei, our calculations do not include any kind of empirical correction. The GDR peak is significantly underestimated for low-mass nuclei, although this can be attributed to the model limitations of QRPA, which is based on a mean-field result that is not sufficiently justified for that mass range. To go to a more nuanced analysis, we need to compare experimental maxima, width, and centroids of the QRPA strength.

		Maximum	Centroid	Width
Even-even	RMSD [MeV]	1.64	0.66	0.42
	Mean deviation [MeV]	0.72	0.33	-0.03
All	RMSD [MeV]	1.75	0.64	0.41
	Mean deviation [MeV]	0.56	0.26	-0.01

Table 3.3: Root mean square and mean deviations of maxima, centroid, and width of the GDR with respect to the QRPA response. We differentiate the deviation with respect to the QRPA calculations(even-even) and the deviation with respect to QRPA calculations and odd interpolations (all).

Many of the nuclei in the photonuclear database include several measurements of the same nuclei, sometimes with contradictory results. In order to do one-to-one comparisons between the QRPA results and experimental data, the following considerations are taken:

1. The experimental centroids and widths of the experimental data are calculated by applying formulae 3.11. To calculate the moments of the experimental series, a trapezoid approximation of the integrals is performed. For nuclei with several experimental series, an average is taken for the final widths and centroids.

2. Only nuclei where the strength covers an interval of more than 10 MeV are considered. This avoids considering the nuclei where only the low-energy part of the GDR is measured.

3. The QRPA GDR centroids and widths are obtained by integrating only the energy range of experimental data. If several runs with different ranges exist, the ranges are considered from the minimum energy of all experiments to the maximum energy of all experiments.

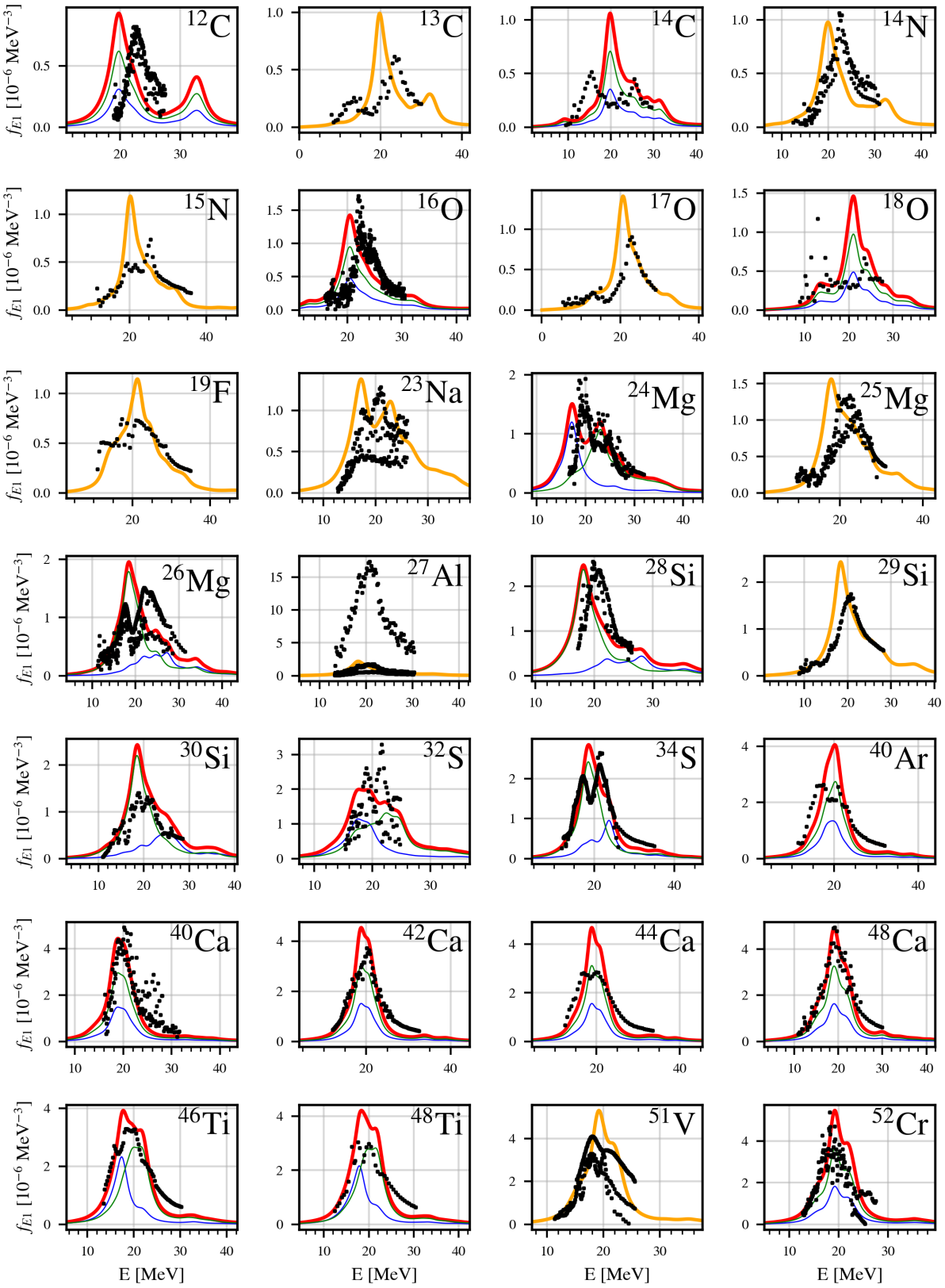

Figure 3.13: $E1$ QRPA strength function calculated with the DD-PC1 Lagrangian. For even-even nuclei, —: $K = 0$ component, —: $|K| = 1$ component, —: total response. For odd nuclei, — interpolated response. The black dots correspond to the photoabsorption data from [43]. (1/6)

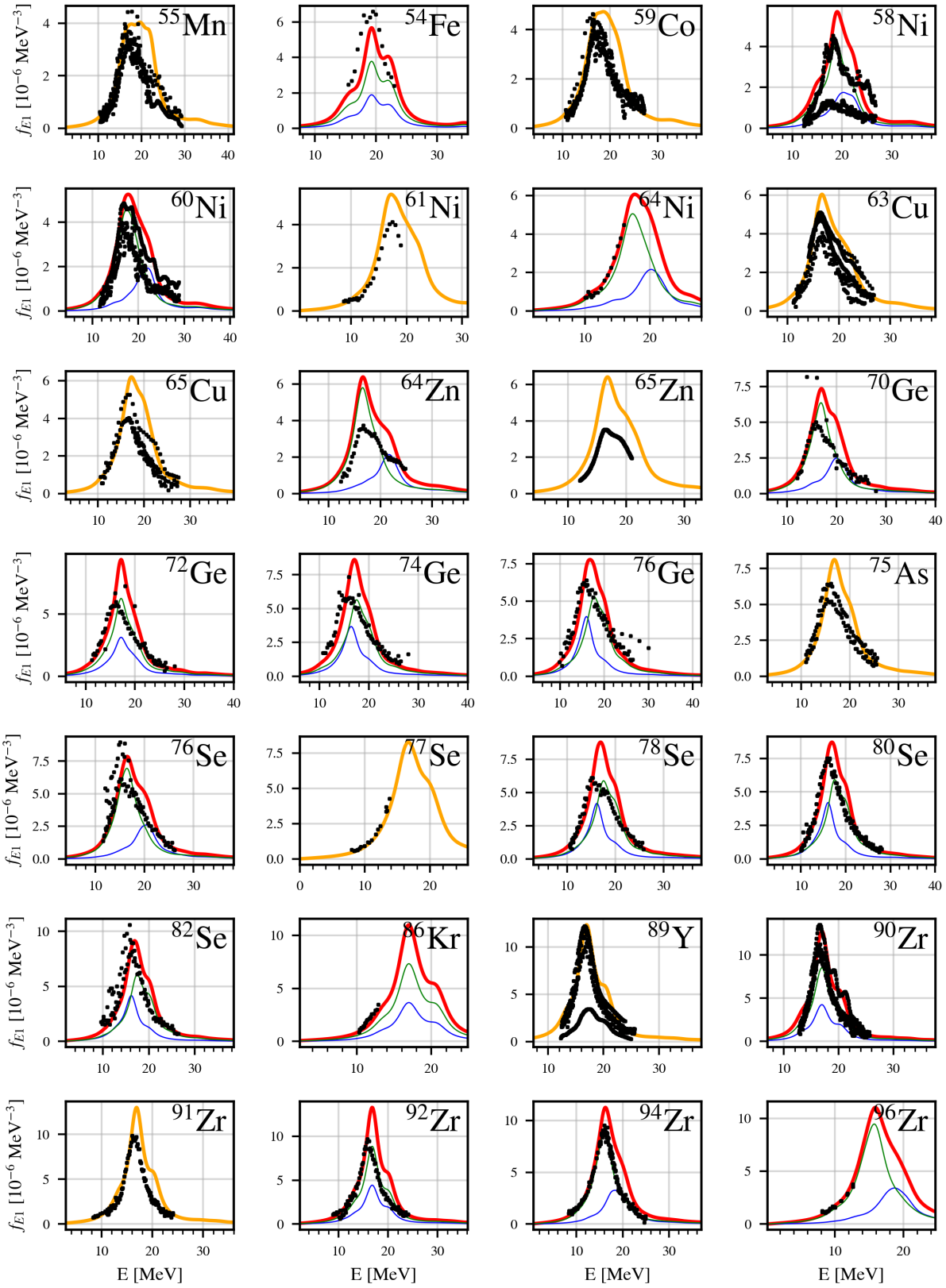

Figure 3.14: $E1$ QRPA strength function calculated with the DD-PC1 Lagrangian. For even-even nuclei, —: $K = 0$ component, —: $|K| = 1$ component, —: total response. For odd nuclei, — interpolated response. The black dots correspond to the photoabsorption data from [43]. (2/6)

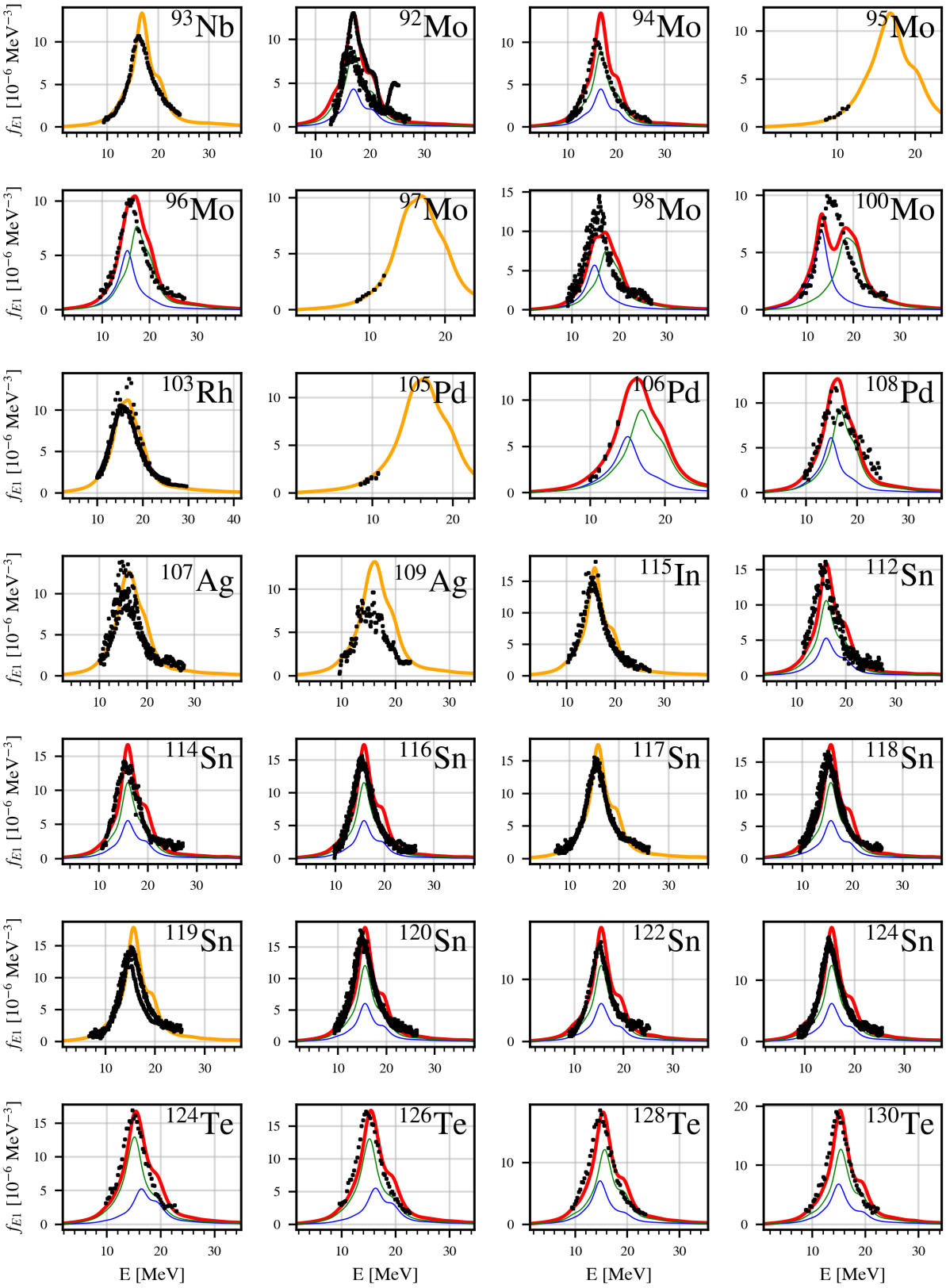

Figure 3.15: $E1$ QRPA strength function calculated with the DD-PC1 Lagrangian. For even-even nuclei, —: $K = 0$ component, —: $|K| = 1$ component, —: total response. For odd nuclei, — interpolated response. The black dots correspond to the photoabsorption data from [43]. (3/6)

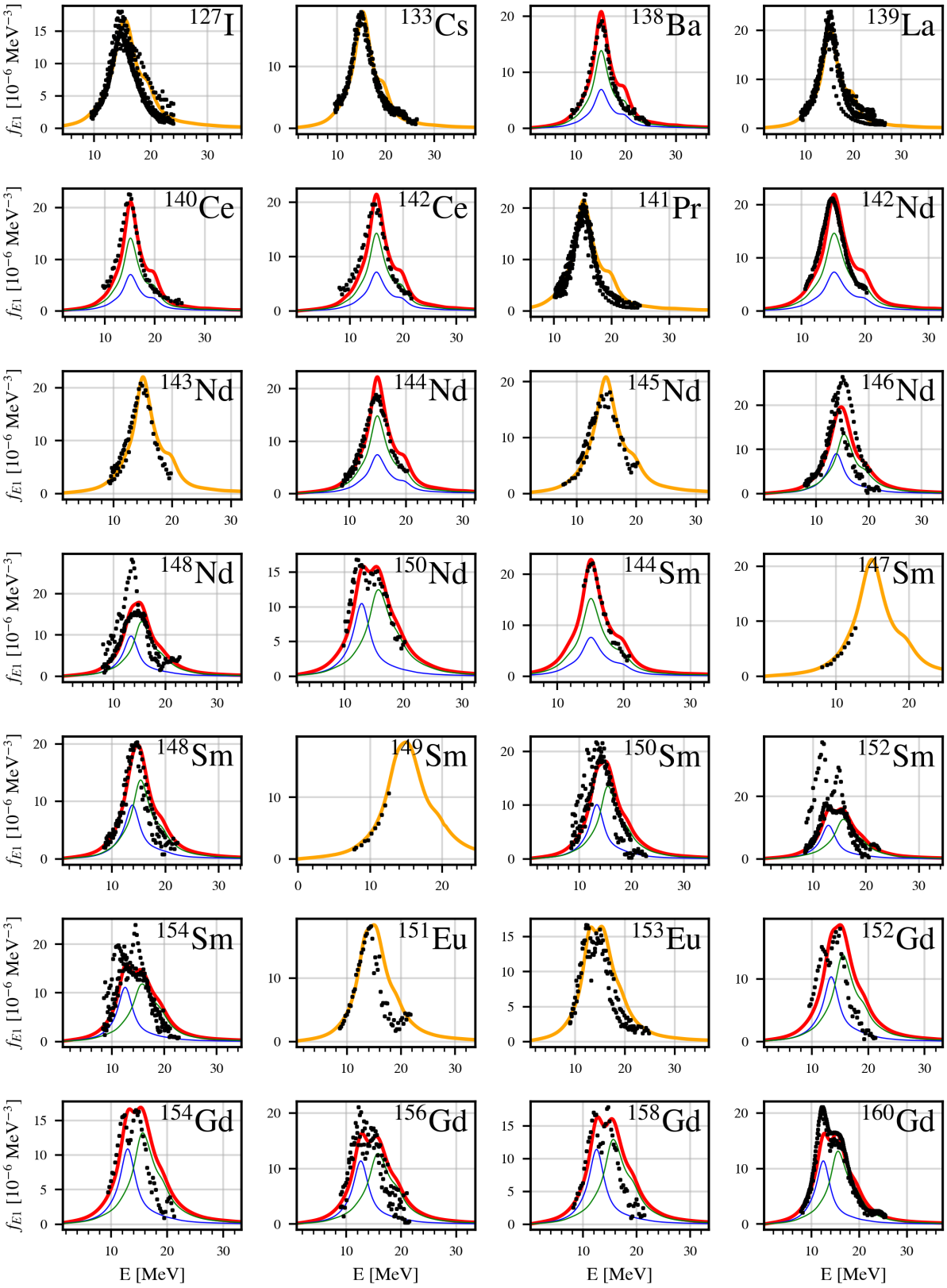

Figure 3.16: $E1$ QRPA strength function calculated with the DD-PC1 Lagrangian. For even-even nuclei, —: $K = 0$ component, —: $|K| = 1$ component, —: total response. For odd nuclei, — interpolated response. The black dots correspond to the photoabsorption data from [43]. (4/6)

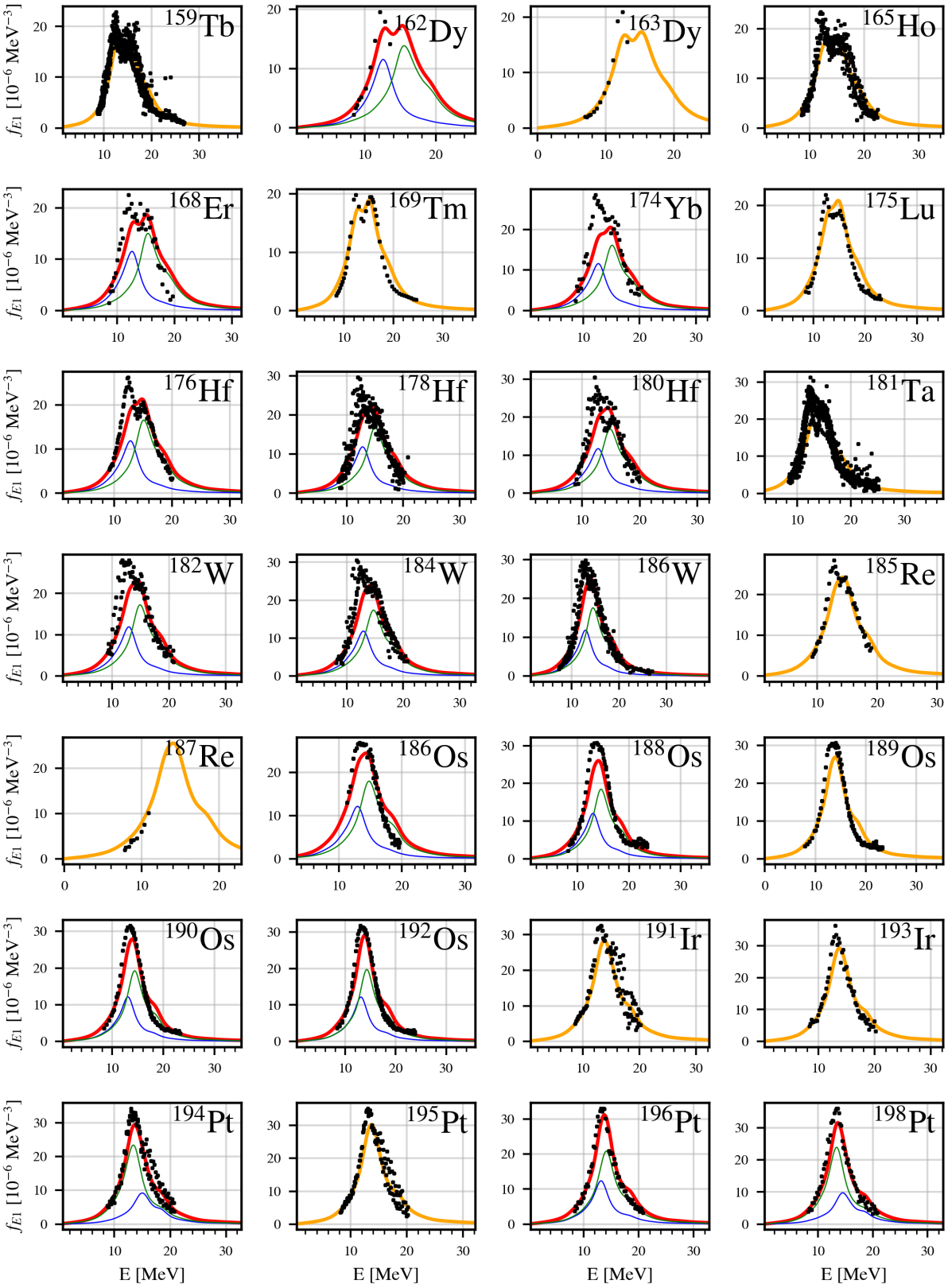

Figure 3.17: $E1$ QRPA strength function calculated with the DD-PC1 Lagrangian. For even-even nuclei, —: $K = 0$ component, —: $|K| = 1$ component, —: total response. For odd nuclei, — interpolated response. The black dots correspond to the photoabsorption data from [43]. (5/6)

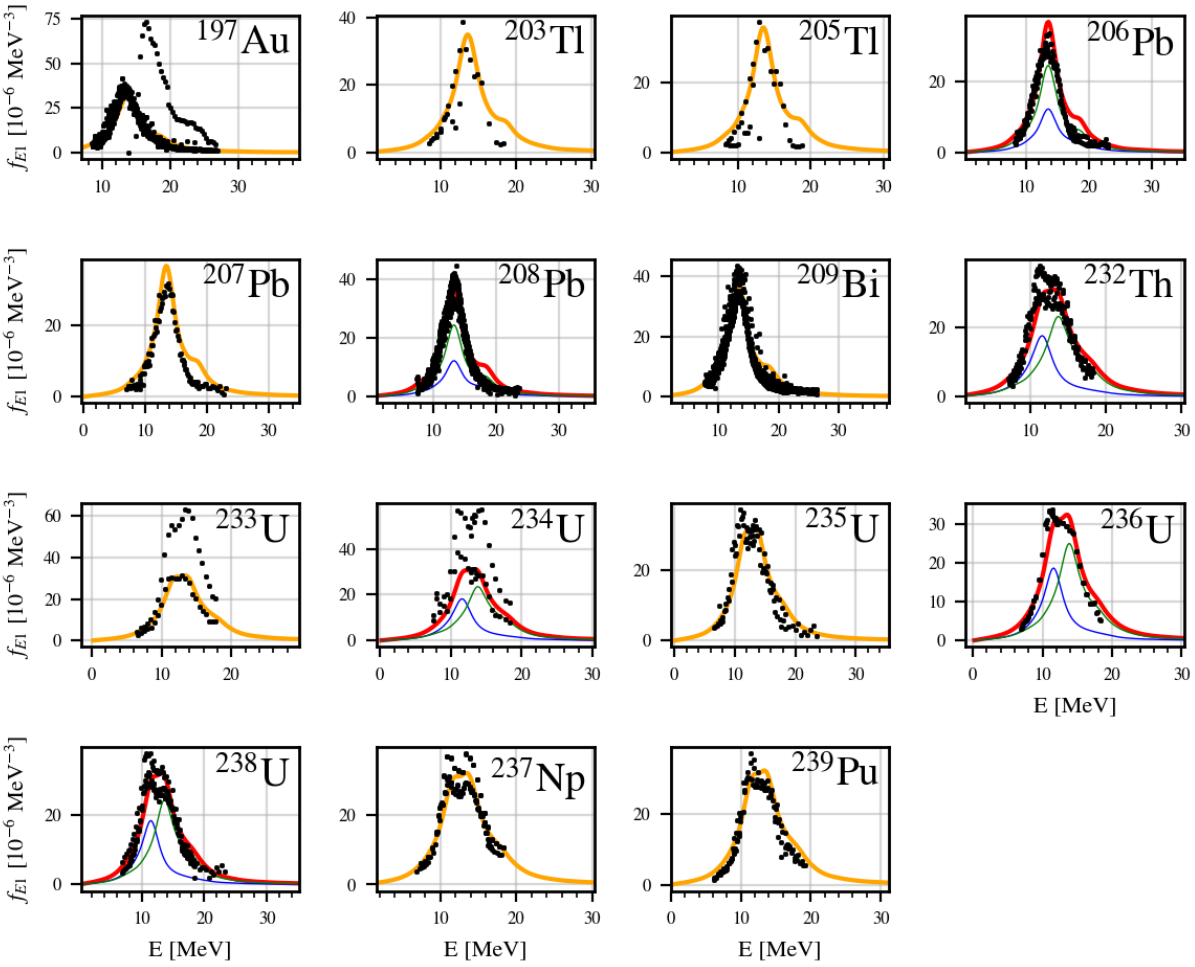

Figure 3.18: $E1$ QRPA strength function calculated with the DD-PC1 Lagrangian. For even-even nuclei, —: $K = 0$ component, —: $|K| = 1$ component, —: total response. For odd nuclei, — interpolated response. The black dots correspond to the photoabsorption data from [43]. (6/6)

The results for the position of the maximum, the centroids, and the width are plotted in figures 3.19, 3.20 and 3.21 respectively. Table 3.3 shows the deviation of the QRPA response to experimental data. We can see how the deviations change very little with the inclusion of the odd interpolation, which justifies our approach. From figure 3.19 we can see how the maxima are mischaracterized up to around mass 50, when the average deviation stays at around 0.5 MeV. This is the same that is observed with the centroid position in 3.20, although for this case the centroids seem to be better characterized in the low region mass. Although for the rest of the masses, the centroids show the 0.5 MeV overestimation, the maxima show big deviations between $A = 150$ and 200. This is because in general, the higher energy peak is almost always the dominant one no matter the deformation, even if the $K = 1$ and $K = 0$ components split roughly following the rules 3.15 and 3.14. This overestimation of the peak is most likely due to the fact that the smearing imposed on all peaks must be the same in the FAM approach. This, however, is not necessarily justified, and other QPRA models have played with energy-dependent smearing.

With respect to the withs, we can see how they are in general underestimated until around $A = 125$ and overestimated after $A = 140$. In any case, this underestimation is only bigger than 0.5 MeV for around $A < 50$.

In any case, we would like to highlight the very good agreement already obtained in this case with our approach. Previous studies with Gogny D1M imposed a global shift of the order of 2

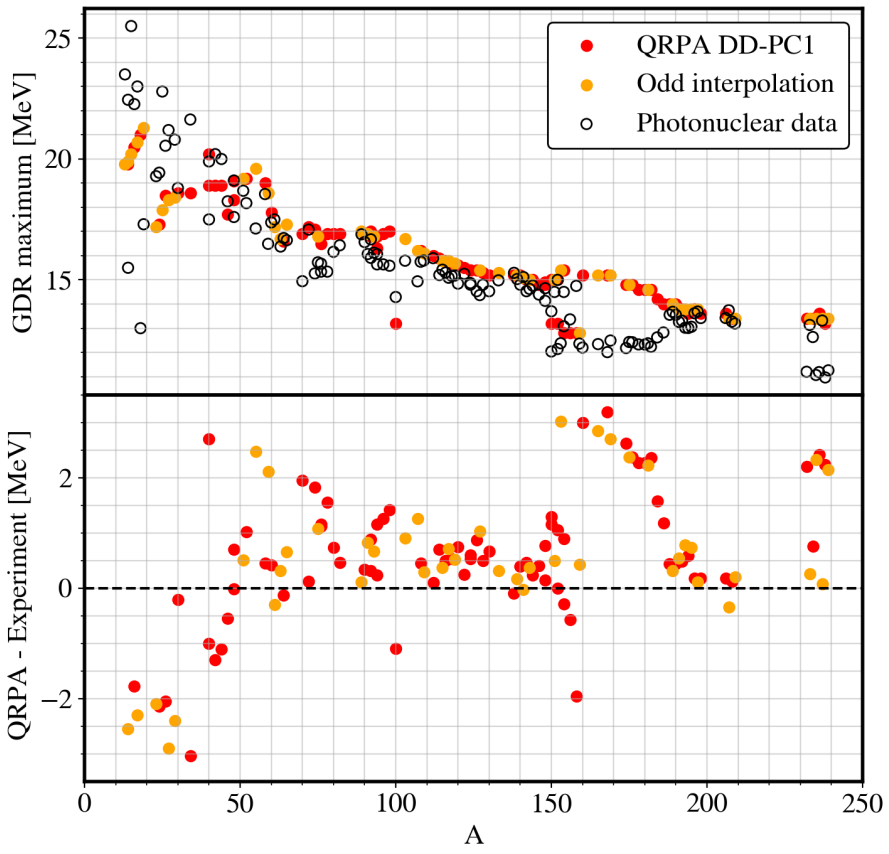

Figure 3.19: Position of the GDR maximum in experimental data and QRPA calculations.

MeV to the strength function to reproduce experimental data, while in our study a 0.5 MeV could be enough. In a future study, one possibility could be the use of empirical rules to obtain a good description of the low-energy strength.

3.3 Conclusion

The study just presented constitutes the second-ever QRPA large-scale calculation of $E1$ strength functions using an explicitly deformed mean field, and the first-ever deformed covariant QRPA global study. The DD-PC1 covariant effective Lagrangian was used. The following conclusions have been drawn:

- An issue with the convergence of the strength calculated with the `DIRQFAM` code has been solved. This was done by optimizing the harmonic oscillator length parameter $\hbar\omega$ to the *physical* minimum.

- The $E1$ strength functions calculated show to follow roughly the systematic rules for the position of the centroid. Deformation effects were shown to be in line with the empirical rules used in other QRPA studies for low deformations, whereas for high deformations quadratic deviations from one of these rules were observed.

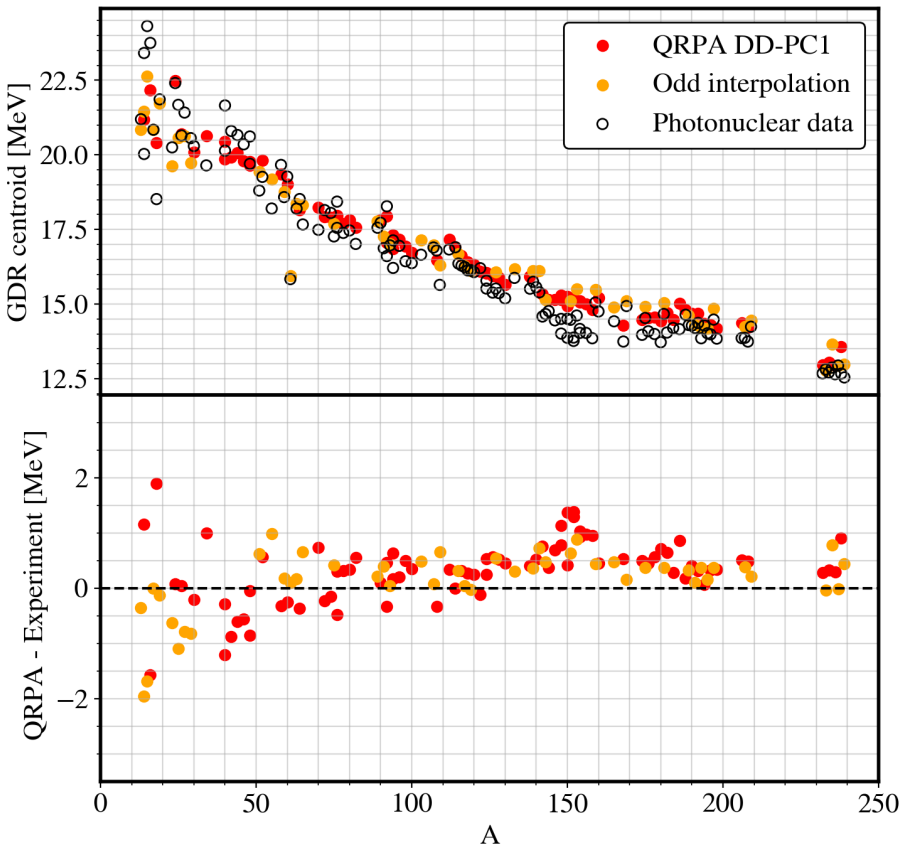

Figure 3.20: Position of the GDR centroid in experimental data and QRPA calculations.

- Shell closures were shown to push the strengths towards higher energies, while their widths are reduced.
- Surprisingly good agreement with data is found, with the exception of the smallest systems, where the predicted GDR strength is strongly shifted to low energies with respect to experimental data. For higher mass systems, a difference of only 0.5 MeV is found with respect to the centroid of the experimental data.

Having achieved a complete set of strengths and performed an analysis of their properties, the goal now would be to use them in future reaction calculations. On the one hand, the results here obtained will be used by the PANDORA [100] for the evaluation of the strengths in nuclei $A < 60$. On the other hand, its incorporation to the reaction code `TALYS` [83] is envisioned. For that, some empirical corrections like the ones used in the previous existing strength databases will be performed. Finally, a straightforward extension of the study is the calculation of more multipolarities, with the $E2$ and $M1$ strengths being strong candidates.

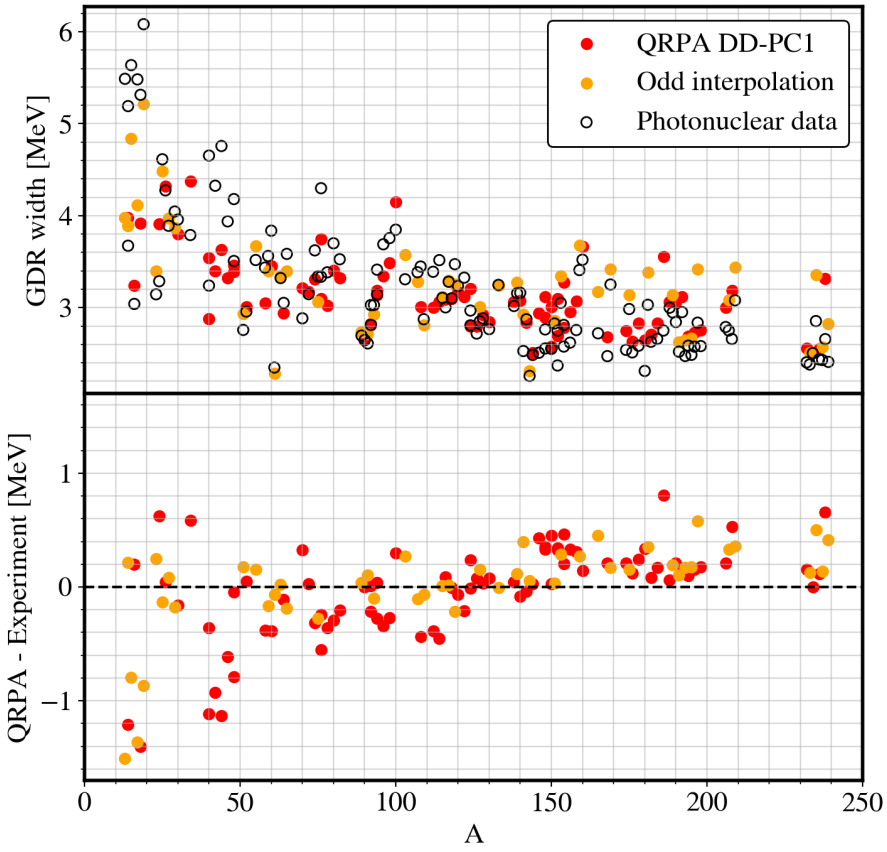

Figure 3.21: Position of the GDR width in experimental data and QRPA calculations.

Chapter 4

E1 strength functions for low and mid-mass nuclei with chiral interactions

The development of realistic internucleon interactions rooted in chiral EFT [27] has opened the way for the exploration of the performance of well-established many-body methods within the chiral approach. The main methodological advantage of these interactions concerning EDFs is that they provide a hierarchy of each of the terms in the Hamiltonian expansion via power counting. Thus, the interaction can be divided into LO (leading order) terms, NLO (next-to-leading order), N2LO (next-to-next-to-leading order), and so on. When these interactions are combined with a many-body method that provides a natural definition of a series expansion of the wave function, the resulting methods are often referred to as *ab initio* theories [2, 3]. Some examples of such methods are Bogolyubov Many-Body Perturbation Theory (BMBPT) [34] or Coupled Cluster (CC) [37]. The main defining factor of *ab initio* methods is that, at least in the ideal scenario, uncertainties coming from both the many-body method and the interaction are always properly accounted for, as both are represented by an order by order expansion. Thus, the subsequent methods are always systematically improvable. A number of *ab initio* studies exist where the E1-related observables, via CC [101, 102] and no-core shell-model (NCSM) [103]. However, these studies cover either just a few closed-shell studies systems or the lightest nuclei. Recently a study of open-shell systems using CC was published [104], although the systems studied are all spherical.

There has been a limited number of QRPA studies using chiral interactions [53, 54, 55, 56]. Whether QRPA in conjunction with chiral interactions can be considered an *ab initio* method is a contentious, but ultimately just semantical issue. One could envision for example QRPA as the $n = 1$ in a series where we model excited states as linear combinations of $2n$ qp excitations and deexcitations plus all the precedent terms, so that the second term is second-QRPA, followed by third-QRPA and so on [53]. On the other hand, the QRPA correlation energy can be related to the BMBPT series result up to second order [105], with the second order coinciding exactly and the first order being exactly three times bigger than the BMBPT one. In any case, in this work, we do not delve further into this question and we limit ourselves to evaluating the ability of chiral interactions to provide a converged QRPA response and to reproduce experimental data.

In this chapter, the chiral QRPA results for all nuclei with photonuclear PSF data of atomic number $6 \leq Z \leq 26$ are presented. We report here only the results for the axially deformed nuclei at HFB level, with the two triaxially deformed ones treated separately in chapter 5. The results with two chiral Hamiltonians are compared: A family of 2+3-body interactions up to N3LO in the chiral expansion[29], and the EM1.8/2.0 interaction[106, 30]. Convergence concerning chiral order and model space are discussed.

4.1 Methodology and interactions

4.1.1 Interactions and SRG evolution

Chiral-EFT-based interactions as the ones in this work are often too hard to be used within the context of many existing many-body methods. Some do not produce a bound state at mean-field for certain nuclei. To be able to capture as many correlations as possible in the HFB state, a unitary transformation is performed on the original Hamiltonian. This is the main idea of the similarity renormalization group (SRG) methods, which make the correlations tractable. This usually comes at the price of higher-body forces arising. Thus, the flow parameters of this transformation have to be optimized so that the most correlations are captured without the higher-body part becoming too dominant. Practical implementations are limited to two-plus-three-body forces. The family of Hamiltonians of reference [29] are evolved with a flow parameter[1] of $\alpha = 0.08\text{fm}^4$. The EM1.8/2.0 interaction uses a different evolution for the 2 and 3-body part, that being $\alpha = 0.0953$ fm^4 and $\alpha = 0.0625\text{fm}^4$ respectively (in terms of λ[2], 1.8 fm^{-1} and 2.0 fm^{-1}, hence its name). This particularity is often pointed at to characterize the EM1.8/2.0 interaction as "not *ab initio* enough" [2]. However, its general good properties have led to its widespread use by the community.

4.1.2 Treatment of the three-body part

The three-body sector of chiral interactions cannot be neglected, as it contributes to a significant portion of the binding energy. However, the computational power required to treat it explicitly becomes intractable pretty fast, especially when using a deformed harmonic oscillator basis. To make calculations doable, the two-plus-three body is approximated into a two-body interaction using the method outlined in reference [107]. This method has been tested to induce errors of around 2-3 % for a wide range of observables.

4.1.3 QFAM parameters

In this chapter, we show the results of $E1$ strength functions calculated via the QRPA-FAM formalism. The code `PAN@CEA` was used, which implements a symmetry-breaking Bogolyubov basis. The results shown in this section use an axially deformed basis for the HFB and FAM fields. A step of 0.5 MeV is used to evaluate the strength functions, from 0 to 50 MeV. As in the previous chapter, a global smearing $\gamma = 1.5$ MeV was chosen.

4.2 Convergence of with respect to model space truncation

4.2.1 Convergence of the HFB states

To perform the most converged possible QRPA calculations, the underlying HFB states are calculated with big enough basis parameters so that the model-space truncation induces errors lower than the keV in binding energies. To do so, calculations are done using reference values of $e_{max} = 12$, $\hbar\omega = 14$ and $e_{3max} = 18$ [3]. Previous studies [55] show that these values ensure properly converged observables for the mass ranges here considered.

[1] The flow parameter is a measure of how much the srg-evolved Hamiltonian differs from the bare Hamiltonian

[2] $\lambda = 1/\alpha^4$

[3] e_{max} here refers to the number of harmonic oscillator shells on which one and two-body operators are expanded, whereas e_{3max} refers to the truncation of the three-body operators induced introduced in the method from reference [107].

	Interaction	E_{HFB} [MeV]	β_2	r [fm]	E_{exp} [MeV]
^{12}C	N3LO	-50.154±0.002	-0.5096±0.0005	2.5103±0.0004	-92.1617
	EM1.8/2.0	-58.652±0.007	-0.4307±0.0015	2.3496±0.0023	
^{14}C	N3LO	-59.140±0.004	-0.0013±0.0038	2.5208±0.0001	-105.2845
	EM1.8/2.0	-70.492±0.002	0.0067±0.0012	2.3665±0.0000	
^{16}O	N3LO	-79.561±0.001	-0.0000±0.0000	2.5796±0.0003	-127.6193
	EM1.8/2.0	-90.312±0.001	0.0000±0.0000	2.4664±0.0004	
^{18}O	N3LO	-82.010±0.016	-0.0228±0.0005	2.7228±0.0013	-139.8078
	EM1.8/2.0	-95.354±0.397	-0.0433±0.0138	2.5921±0.0003	
^{26}Mg	N3LO	-124.496±0.002	0.5617±0.0000	3.0735±0.0002	-216.6806
	EM1.8/2.0	-147.582±0.005	0.4879±0.0003	2.9105±0.0004	
^{28}Si	N3LO	-135.717±0.001	-0.4439±0.0001	3.1068±0.0002	-236.5368
	EM1.8/2.0	-163.308±0.000	-0.3717±0.0001	2.9139±0.0001	
^{30}Si	N3LO	-145.761±0.272	-0.3632±0.0002	3.1437±0.0015	-255.6196
	EM1.8/2.0	-175.670±0.004	-0.2948±0.0000	2.9555±0.0005	
^{34}S	N3LO	-170.580±0.001	-0.2370±0.0003	3.2021±0.0001	-291.8390
	EM1.8/2.0	-204.597±0.019	-0.1662±0.0006	3.0233±0.0003	
^{40}Ar	N3LO	-206.316±0.009	-0.1571±0.0003	3.3332±0.0004	-343.8104
	EM1.8/2.0	-245.557±0.022	-0.1353±0.0007	3.1771±0.0007	
^{40}Ca	N3LO	-210.547±0.002	0.0000±0.0000	3.3199±0.0003	-342.0522
	EM1.8/2.0	-247.208±0.004	-0.0000±0.0000	3.1821±0.0004	
^{42}Ca	N3LO	-219.676±0.102	-0.0472±0.0118	3.3610±0.0005	-361.8957
	EM1.8/2.0	-259.756±0.013	-0.0213±0.0008	3.2155±0.0004	
^{44}Ca	N3LO	-229.981±0.004	0.1102±0.0003	3.4028±0.0001	-380.9598
	EM1.8/2.0	-274.323±0.026	0.1023±0.0016	3.2509±0.0007	
^{48}Ca	N3LO	-250.033±0.001	0.0002±0.0002	3.4653±0.0001	-416.0012
	EM1.8/2.0	-303.596±0.010	0.0000±0.0000	3.2959±0.0004	
^{46}Ti	N3LO	-237.186±0.004	0.2641±0.0003	3.4747±0.0003	-398.1973
	EM1.8/2.0	-286.111±0.008	0.2425±0.0001	3.3195±0.0003	
^{48}Ti	N3LO	-247.443±0.004	0.2320±0.0001	3.4982±0.0002	-418.7046
	EM1.8/2.0	-301.431±0.016	0.2049±0.0006	3.3294±0.0006	
^{52}Cr	N3LO	-266.870±0.003	0.3264±0.0001	3.5913±0.0002	-456.3517
	EM1.8/2.0	-329.302±0.026	0.3187±0.0006	3.4449±0.0010	
^{54}Fe	N3LO	-270.145±0.009	0.3724±0.0001	3.6465±0.0002	-471.7648
	EM1.8/2.0	-337.833±0.020	0.2960±0.0000	3.4611±0.0007	

Table 4.1: HFB binding energies, β_2 deformation, and radii calculated with N3LO and EM1.8/2.0 interaction. Reported values are taken as the mean value when performing calculations at e_{max} = 10 and 12 and $\hbar\omega$ = 12 and 14 MeV, while error bars are their standard deviation. A constant value of e_{3max} = 18 is used. Experimental energies E_{exp} are also reported [93]

Table 4.1 shows the HFB calculated values of binding energies, β_2 deformations, and mean radii with EM1.8/2.0. and the interaction of reference [29] at N3LO (from here on just refered as N3LO for convenience). To provide a measure of the uncertainty, the value shown is the mean value obtained with e_{max} 12 and $\hbar\omega$ = 12 and 14 MeV, with the error intervals being their standard deviation. The vast majority of nuclei show convergence up to the third decimal. The value of e_{3max} = 18 is kept fixed because it does not seem to have any impact at HFB and QRPA levels.

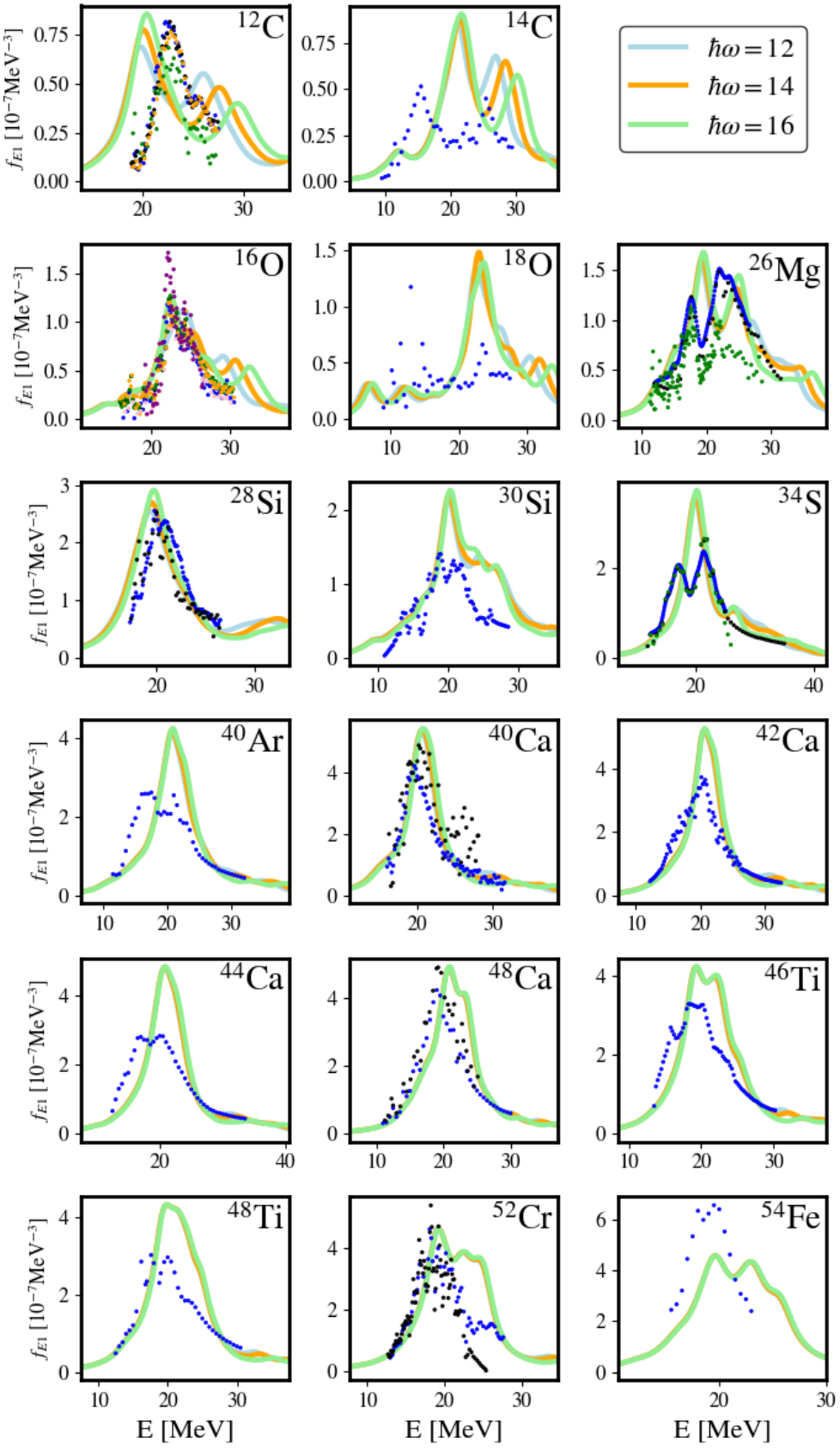

Figure 4.1: $E1$ QRPA strength function calculated with the interaction of reference [29] at N3LO level with $e_{max} = 12$ and $e_{3max} = 18$ for different values of the harmonic oscillator frequency $\hbar\omega$ parameter. Experimental data taken from [43].

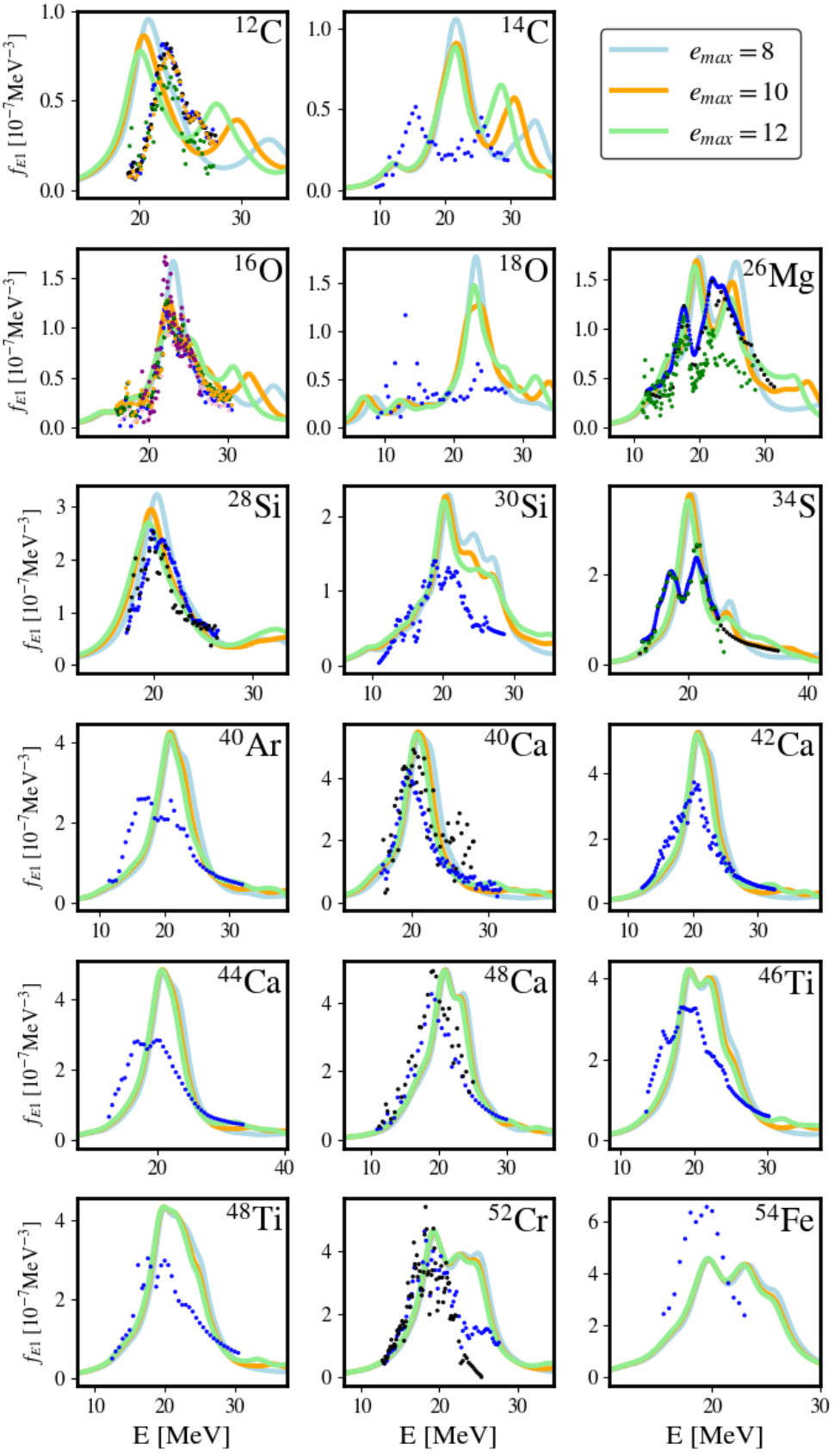

Figure 4.2: $E1$ QRPA strength function calculated with the interaction of reference [29] at N3LO level with $\hbar\omega$ = 14 MeV parameter and e_{3max} = 18 for different values of e_{max}. Experimental data taken from [43].

We can see clearly how the EM1.8/2.0 consistently predicts a lower nuclear radius with respect to N3LO, as it had already been observed. The fact that binding energies are so different is due to the fact that both interactions are evolved with different parameters. Contrary to EDFs, chiral interactions are not expected to give a very good description of the ground state at HFB level, leaving a big space to correlation energies with more sophisticated methods.

Having been able to establish that our HFB states are well converged, the QRPA-FAM response is studied.

4.2.2 Convergence of the QRPA response

Even though HFB states show good convergence properties, this may not be enough to produce converged strengths. As we saw in section 3.1, variations of the harmonic oscillator length may have big consequences at QRPA level. To check whether this is the case, we calculate the N3LO strength function for various kinds of model space truncation. Figure 4.1 shows the strength function for fixed $e_{max} = 12$ and $e_{3max} = 18$ and varying harmonic oscillator frequency $\hbar\omega$. We see that, somewhat counter-intuitively, lighter nuclei show a worse convergence than higher mass ones, which are virtually completely converged. The same is observed with the strength calculated with varying values of e_{max}, as seen in figure 4.2 and fixed $\hbar\omega = 14$ MeV. This bad convergence for small nuclei has also been observed using the EM1.8/2.0 for the extreme case of the deuteron [108], where up to $e_{max} = 20$ had to be used to obtain good results. In general, correlations in small systems do not average out at mean-field, hence their lower performance. We note that here a harmonic oscillator basis was used. Better convergence may be achieved by using the natural basis, which is the one diagonalizing the 1-body density, which was recently shown as a possibility for open-shell systems using chiral interactions [109]. Reducing the value of $e_{3max} = 16$ has no visible effect on the strengths.

In any case, the main peak seems to be very reasonably converged for all nuclei, save ^{12}C, while the high energy part shows more variation, which is mostly beyond the experimental values.

4.3 Impact of the chiral expansion

As mentioned earlier, chiral EFT gives us a natural hierarchy in terms of the Hamiltonian via power counting. To study the impact of the truncation of the Hamiltonian in the QRPA response, we compare the strengths produced at different chiral orders for the interactions in reference [29]. All strengths are calculated using $e_{max} = 12$. The e_{3max} and $\hbar\omega$ parameters are different for each order[4]. For the frequency, $\hbar\omega = 14$ MeV for N3LO , $\hbar\omega = 12$ MeV for N2L0 and $\hbar\omega = 16$ MeV for NLO are used. As for the value of e_{3max}, $e_{3max} = 18$ is used for N3LO and $e_{3max} = 14$ for the rest.Figure 4.3, displays the calculated strengths at each chiral order. As noted in reference [55], mean-field results produced at NLO are pretty different than the ones at N2LO and N3LO, which are pretty close. This is carried to and amplified in the QRPA response. The bulk NLO response lies at higher energies, which get pushed to the region of experimental data once we go to higher orders. Again, this is more clearly the case in higher-mass nuclei. We can see also how the N2LO and N3LO are pretty similar for the bigger nuclei. However, for the heaviest systems, one can see that the GDR is pushed to the right at N3LO, with the effect starting to be noticeable at ^{46}Ti and then getting more pronounced with a bigger mass. This is the main effect limiting the application

[4]This is mostly due to the number of interaction files available in our team being limited. However, having seen the little impact that $\hbar\omega$ has on the strengths for N3LO, it is safe to assume that the effect is not big in all but the smallest nuclei.

of QRPA with this interaction for higher masses and could be a signal of the need to go higher in the chiral expansion.

To make a more quantitative analysis, the GDR centroids, maxima, and widths are calculated following the same procedure as in section 3.2.4. Figure 4.4 shows their value for each nucleus, while 4.2 shows their root mean squared and mean deviations with respect to experimental photoabsorption data. The fact that we only integrate the strength in the experimental region may add a bias to the shown results. For example, the strength of ^{56}Fe can be seen to have a pretty different shape from the experimental data. However, as the shape is continued beyond the experimental region, the calculated experimental and QRPA centroids coincide. The calculation of the widths at NLO is also compromised, as a big portion of the strength is at high energy. While NLO produces data very far from the experiment, the performance with N2LO and N3LO is similar. This is a clear signal of convergence of the QRPA response with the chiral expansion. For all cases, N3LO shows a higher energy for the centroid and maximum. In fact, both are on average overestimated with respect to the experiment in N2LO and N3LO, with the RMSD being higher at N3LO than N2LO for both. On the other hand, it seems that widths are similarly reproduced in both cases.

Interaction		NLO	N2LO	N3LO	EM1.8/2.0
Centroid	RMSD [MeV]	4.88	0.99	1.23	1.91
	Mean deviation [MeV]	4.26	0.56	0.85	1.66
Maximum	RMSD [MeV]	11.27	3.68	3.18	4.18
	Mean deviation [MeV]	10.30	0.77	1.41	2.81
Width	RMSD [MeV]	0.54	0.60	0.57	0.64
	Mean deviation [MeV]	0.08	0.17	-0.01	0.18

Table 4.2: Values of the root mean square and mean deviations of the $E1$ strength centroids, maxima, and widths calculated with the different interactions considered in the study.

4.4 Dependence on the interaction

In order to compare the performance of at least two different chiral Hamiltonians, in this section we show the results obtained using the EM1.8/2.0 and N3LO interactions. In this case, we use for both interactions $e_{max} = 12$, $\hbar\omega = 14$ MeV and $e_{3max} = 18$. The strength functions calculated are shown in figure 4.5. As we can observe, the results obtained a similar overall shape, although the results with the EM1.8/2.0 interaction seem to be shifted towards higher energies. This is confirmed by looking at the numerical values for the centroids, widths, and maxima, which are shown in table 4.2 and figure 4.6. In all cases, maxima and centroids calculated with EM1.8/2.0 lie at higher energies than those from N3LO. It is noted that even though different deformations are predicted for several nuclei, such as ^{54}Fe, the QRPA responses have similar shapes. EM1.8/2.0 seem also to give an overall bigger width, this being mostly led by the higher high energy contribution of EM1.8/2.0.

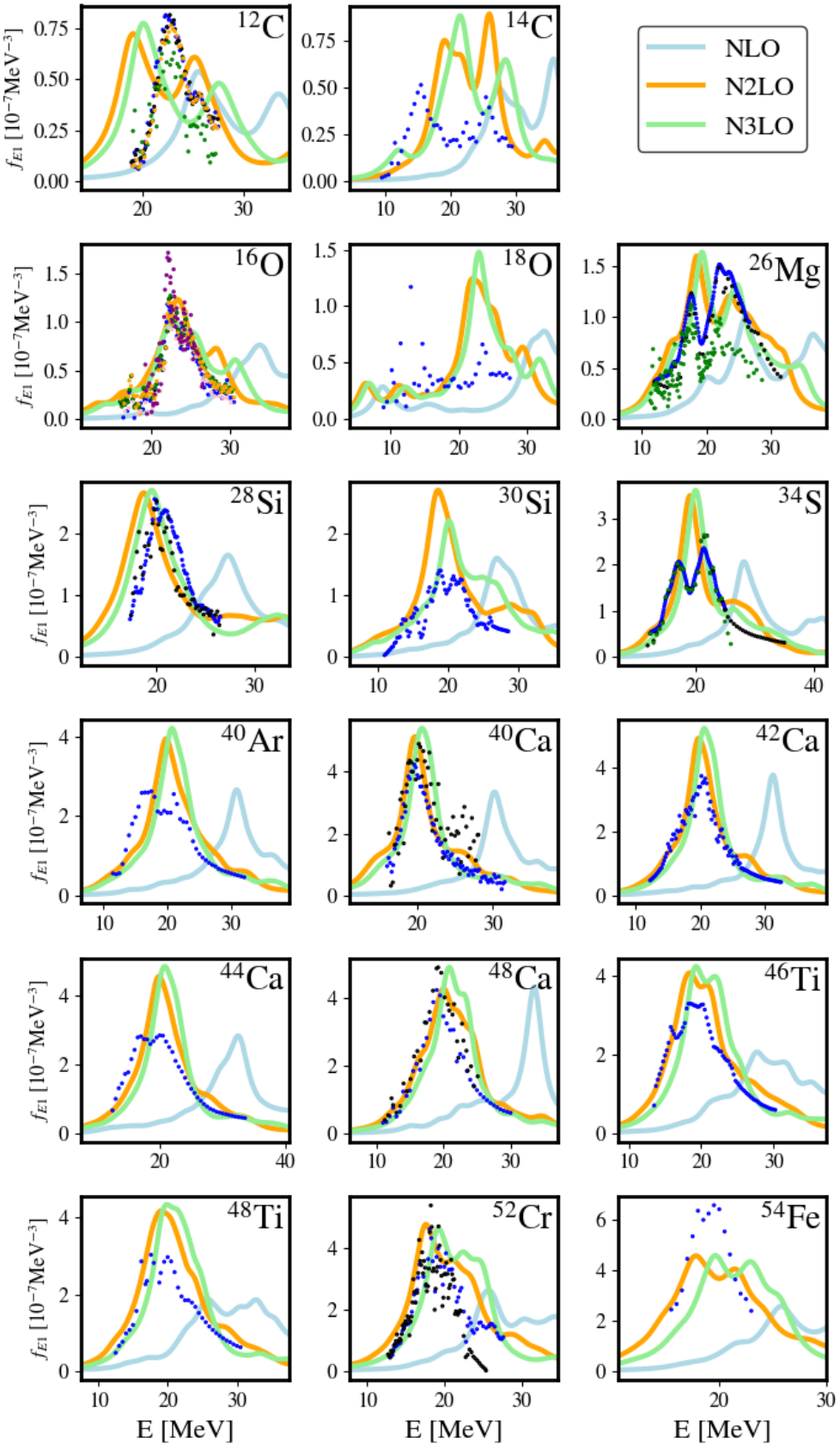

Figure 4.3: $E1$ QRPA strength function calculated with the interaction of reference [29] for different values of the chiral expansion.. Experimental data taken from [43].

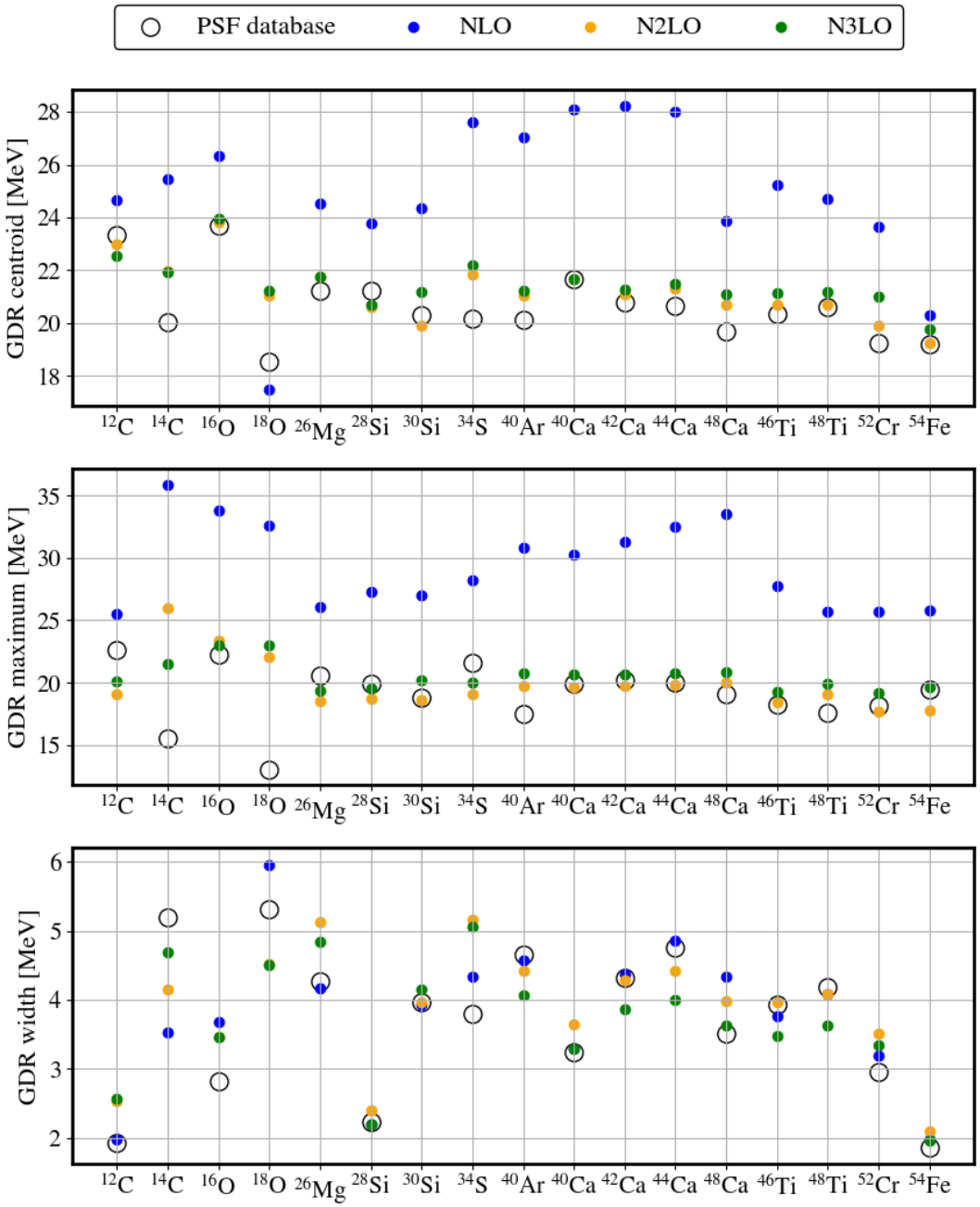

Figure 4.4: $E1$ QRPA strength function centroid, maximum and width for different chiral expansions of the interaction in reference [29]. Experimental data taken from [43].

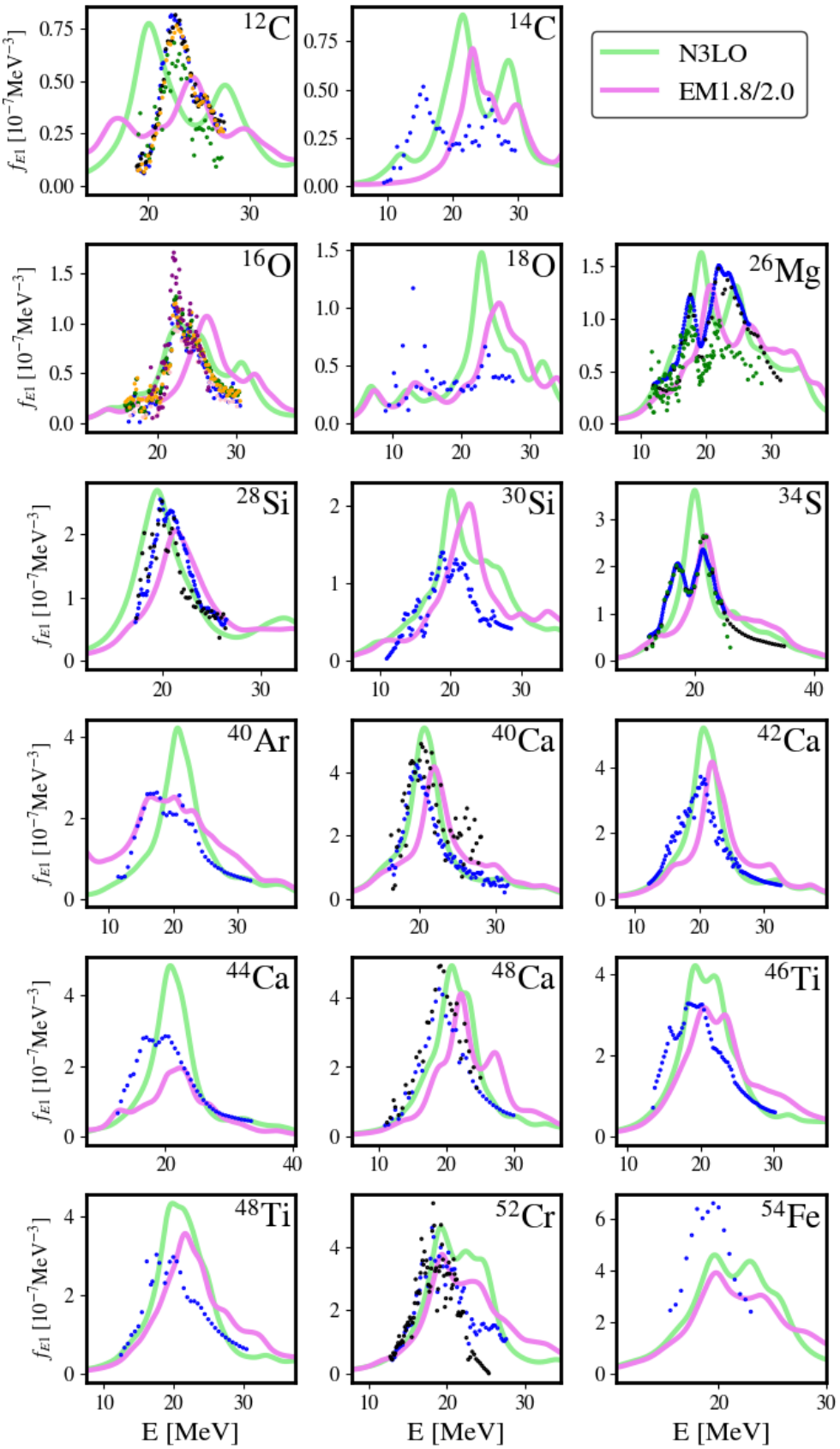

Figure 4.5: $E1$ QRPA strength function calculated with the interaction of reference [29] and EM1.8/2.0 using e_{max}=12,e_{3max}=18 and $\hbar\omega$ = 14 MeV. Experimental data taken from [43].

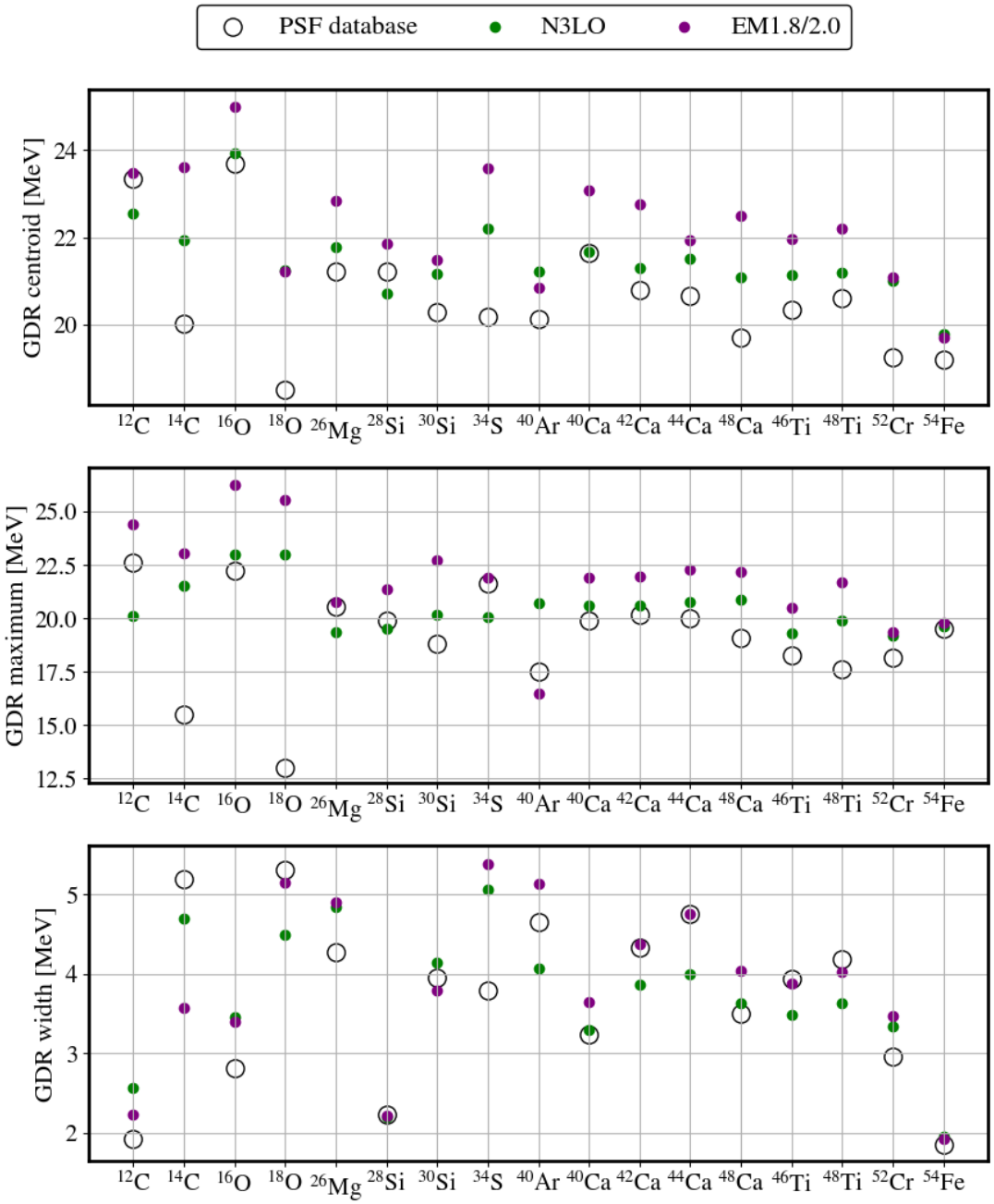

Figure 4.6: $E1$ QRPA strength function centroid, maximum and width for different chiral expansions of the interaction in reference [29]. Experimental data taken from [43].

4.5 Conclusion

$E1$ QRPA responses have been calculated for axially deformed nuclei for which there are experimental photonuclear data up to iron. This marks the first time that all nuclei with experimental data up to that mass have been studied using QRPA with chiral interactions. The following remarks can be made:

- QRPA strength functions are sensitive to variations of the model space even if the changes of the observables at the mean-field level are negligible. This effect is in concordance with what was found with covariant EDF. Light nuclei seem to be more affected by this.
- Using the interactions from reference [29], increasing the chiral expansion from NLO to N2LO produces a push towards the experimental region of the GDR. N2LO and N3LO produce similar responses, with N3LO being slightly pushed to higher energies, this effect increasing with the nuclear mass.
- The interaction from reference [29] and EM1.8/2.0 show similar performances, with EM1.8/2.0 predicting higher energies for the GDR centroid and maxima.

This study opens the way for the large-scale evaluation of QRPA strength functions of low to mid-mass nuclei. The results here correspond only to the nuclei for which there are experimental GDR data; a straightforward perspective would be to study to extend it to more nuclei in this region. Valuable predictions of the dipole polarizability [110, 111] could also be easily derived from chiral QRPA-FAM by simply evaluating the m^{-1} moment of the $E1$ strength, which is readily available with the data from this study.

Chapter 5

Role of triaxial deformation in the E1 response using QRPA with chiral interactions

Self-consistent mean-field methods allow the ground state wave function to break fundamental symmetries of the nuclear Hamiltonian. This allows to capture of additional correlations at the mean-field level while keeping a simple form of the wave function. HFB itself is a good example of this, as particle number is explicitly broken by the mean field to account for short-range pairing correlations. Additionally, to better grasp long-range correlations, it is common practice to use an axially deformed mean field, which implies the loss of the total angular momentum J as a good quantum number. This is the approach that was followed in chapters 3 and 4. However, symmetry-breaking puts a strain on computational cost, requiring working in increasingly bigger subspaces as more symmetries are broken. This gets further amplified when going to QRPA. As it was already mentioned in chapter 3, from the existing global QRPA studies, only the one using the Gogny-D1M interaction [85, 61, 60] implements a symmetry breaking axially deformed mean-field. Even in that case, triaxial deformation is not considered: The matrix formulation of QRPA is already very computationally expensive when the QRPA matrix is divided into K^π symmetry blocks[60]. Going triaxial implies only keeping parity π as a good quantum number. Nevertheless, the development and adoption by the community of the FAM approach have made this kind of computations feasible, with studies being published using Skyrme functionals [70, 71] and valence space interactions [112]. However, the novelty of the approach implies that not many avenues have yet been explored, as is the case of the use of chiral interactions.

In chapter 4, the chiral QRPA $E1$ gamma-ray strength function of axially deformed nuclei in the region $6 \leq Z \leq 22$ for which there exist photonuclear data of the giant resonance region was calculated. Such mass range also contains two nuclei that are clearly triaxially deformed at mean-field level using chiral interactions: ^{24}Mg and ^{32}S. Both these nuclei have been shown experimentally to be triaxially deformed in their ground states [113]. In the following pages, the first-ever results of triaxially deformed QRPA calculations using χEFT derived Hamiltonians are presented. As was the case in the previous chapter, the `PAN@CEA` [79] code was used. The family of chiral interactions at N3LO introduced in reference [29] is used for all the calculations. If not explicitly indicated otherwise, we make the same considerations as in chapter 4 to produce our strength functions and calculate their centroids and widths.

5.1 Triaxial chiral HFB results

To begin this study, the properties of the ground state at HFB level for ^{24}Mg and ^{32}S are analyzed. The same considerations as in chapter 4 are taken for the treatment of the chiral Hamiltonian, keeping fixed a value of the three-body truncation of $e_{3\max} = 18$.

5.1.1 Convergence of the HFB state

For a correct QRPA description, we must ensure that the HFB solution is correctly converged. To do so, the impact of the model space truncation on the HFB mean radius and energy is studied. The case of ^{24}Mg is taken as the reference, as we saw in chapter 4 that smaller nuclei show a less converged QRPA response for this mass range. The axial case, obtained by diagonalizing the HFB equation in K^π blocks, is compared to the triaxial result, where only π is kept as a good quantum number.

Figure 5.1 shows the result of the HFB energy for different values of number of harmonic oscillator shells e_{max} and harmonic-oscillator frequency $\hbar\omega$ in ^{24}Mg. A clear convergence tendency can be observed in $e_{\max}$, with the curve becoming essentially flat between $\hbar\omega = 12$ MeV to 16 MeV for $e_{max} = 12$. Additionally, all energy lines seem to converge towards the value of $\hbar\omega = 12$. The triaxial HFB states remain around 3 MeV more bound than the axial ones for all model space parameters, with convergence tendencies unchanged between both cases.

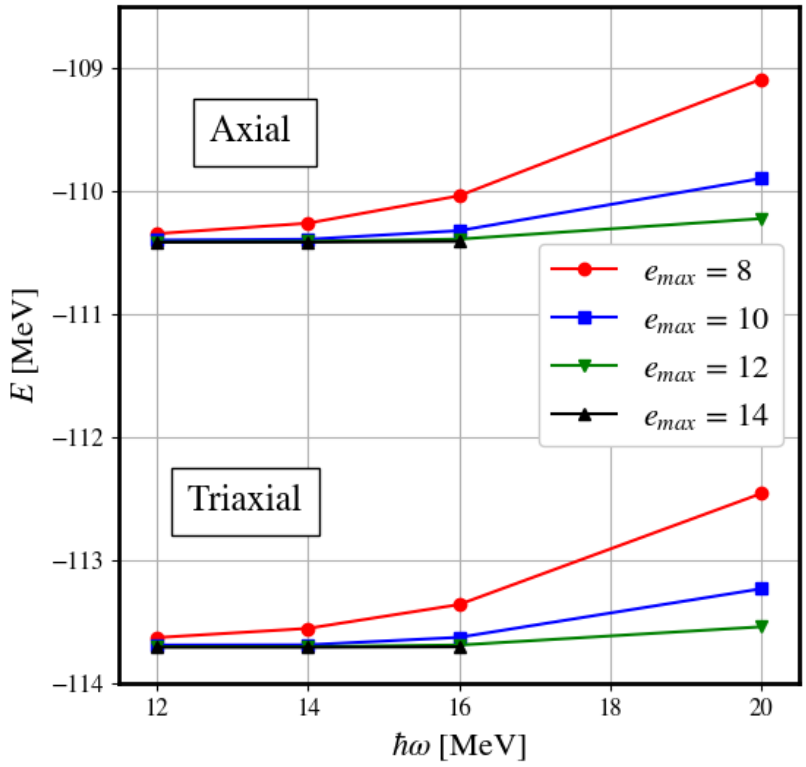

Figure 5.1: ^{24}Mg HFB energy for different values of e_{max} and mean radius.

On the other hand, the convergence of the mean radii can be seen in figure 5.2. Similar convergence tendencies are observed as in the case of the energy. However, in this case, a bigger sensitivity to $\hbar\omega$ is observed, with 12 MeV being the optimal value like before. It is seen that

triaxial deformation adds around 0.013 fm to the mean radius, which is to be expected. Having established this, a value of model space of $e_{\max} = 12$ and harmonic oscillator frequency $\hbar\omega = 12$ MeV are set for the rest of this study, which assures convergence at a reasonable computational cost.

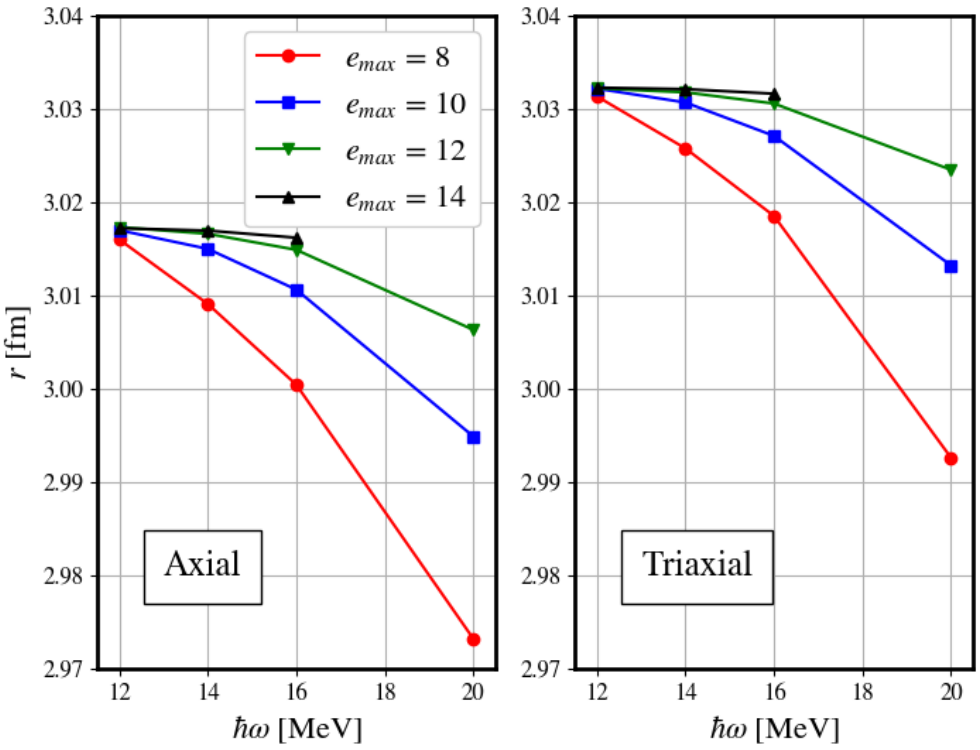

Figure 5.2: ^{24}Mg HFB mean radii for different values of e_{max} and mean radius.

5.1.2 Evolution with deformation of the HFB state

To characterize the deformation HFB state, the β, γ parameters are used, which are defined using the expectation value of the components of the electric quadrupole operator Q_{2K} as

$$\beta \equiv \frac{4\pi}{3AR_0^2}\sqrt{\langle Q_{20}\rangle^2}, \quad \gamma \equiv \arctan\left(\sqrt{2}\frac{\langle Q_{22}\rangle}{\langle Q_{20}\rangle}\right), \tag{5.1}$$

with $R_0 = 1.2A^{1/3}$. Axial prolate and oblate shapes of the nucleus correspond to the values of $\gamma = 0°$ and $60°$ respectively. Using the values of $e_{\max} = 12$ and $\hbar\omega = 12$ MeV, calculations for ^{32}S and ^{24}Mg are performed. The values obtained at the HFB minimum for the binding energy, deformation parameters, and mean radius are shown in the figure in table 5.1. Both nuclei show clearly triaxial deformation at the mean-field level, this being signaled by the values of the γ parameter, far from $0°$ and $60°$. To better understand the gradual effect of the deformation on the HFB state, the potential energy surfaces (PES) of both nuclei are calculated. This is done by launching a series of HFB calculations constraining (β, γ) to different values. The results are plotted in figure 5.3. Each of the levels of the figure represents an increase of 1 MeV in the energy with respect to the minimum. Although the minimum value for ^{32}S has a more pronounced triaxial value, with γ close to $30°$, its PES is softer, with the axial minimum at the prolate region being less than 2 MeV higher in energy.

In contrast, ^{24}Mg shows a more localized minimum, the axial value being around 3 MeV higher in energy. Additionally, the PES of ^{32}S shows a secondary minimum at a high prolate deformation of $\beta = 1.00$. This minimum is situated at an energy of -152.61 MeV, around 4 MeV above the main minimum.

Nucleus	E_{HFB} [MeV]	β	γ	r [fm]
^{24}Mg	-113.70	0.580	13.80°	3.014
^{32}S	-156.84	0.344	32.50°	3.188

Table 5.1: HFB energy, quadrupole deformation parameter β, triaxial deformation parameter γ and mean radius r calculated with the chiral interaction of reference [29] at N3LO.

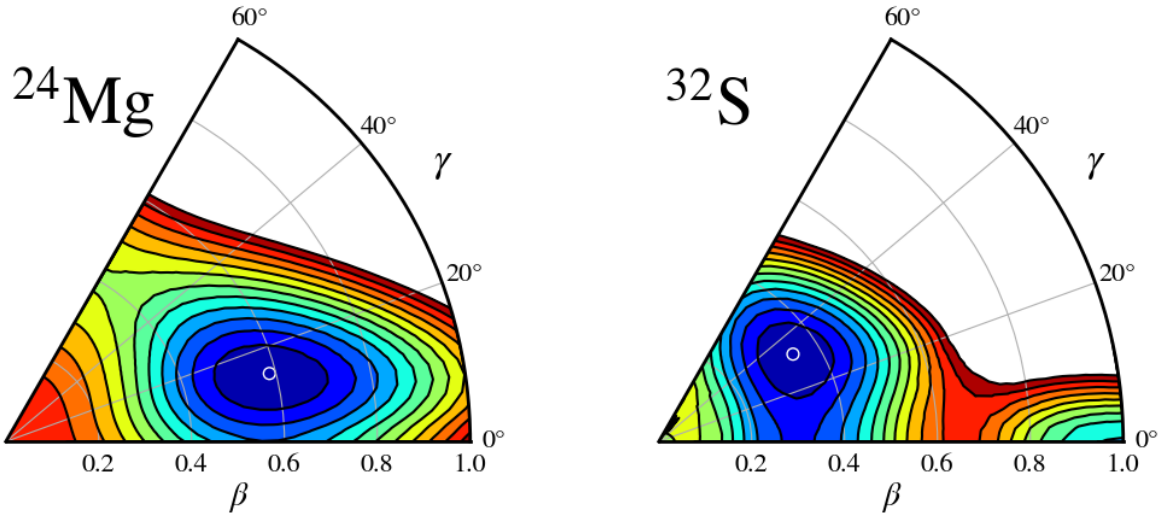

Figure 5.3: ^{24}Mg and ^{32}S HFB potential energy surfaces calculated with the chiral interaction of reference [29] at N3LO. Different levels represent 1 MeV energy steps with respect to the minimum, marked with a white circumference.

In order to have a better idea of what is happening at those minima, the one-body density will be explored, which will unveil clustering phenomena taking place in both nuclei.

5.1.3 α-clustering at mean-field level in ^{24}Mg

Low to mid-mass nuclei are known to be able to show molecule-like structures composed of clusters [114]. These structures can be considered as a transitional state between crystalline and quantum-liquid phases in finite nuclei [115]. One of the most famous cases of clustering in nuclei is the Hoyle state[1] [116], which is the first 0^+ state in ^{12}C and consists in a chain of α particles. Within the context of EDFs, the cluster composition of several nuclei has been shown to arise at mean-field level [115, 117, 118]. However, to do so, it is important to break as many symmetries of the mean-field as possible, so as to capture the long-range correlations involved in the process of clustering. Atomic nuclei with the same number of particles as multiples of ^{4}He are likely candidates to show an α clustered structure. This is the case for ^{24}Mg.

[1] The only named state in nuclear spectroscopy.

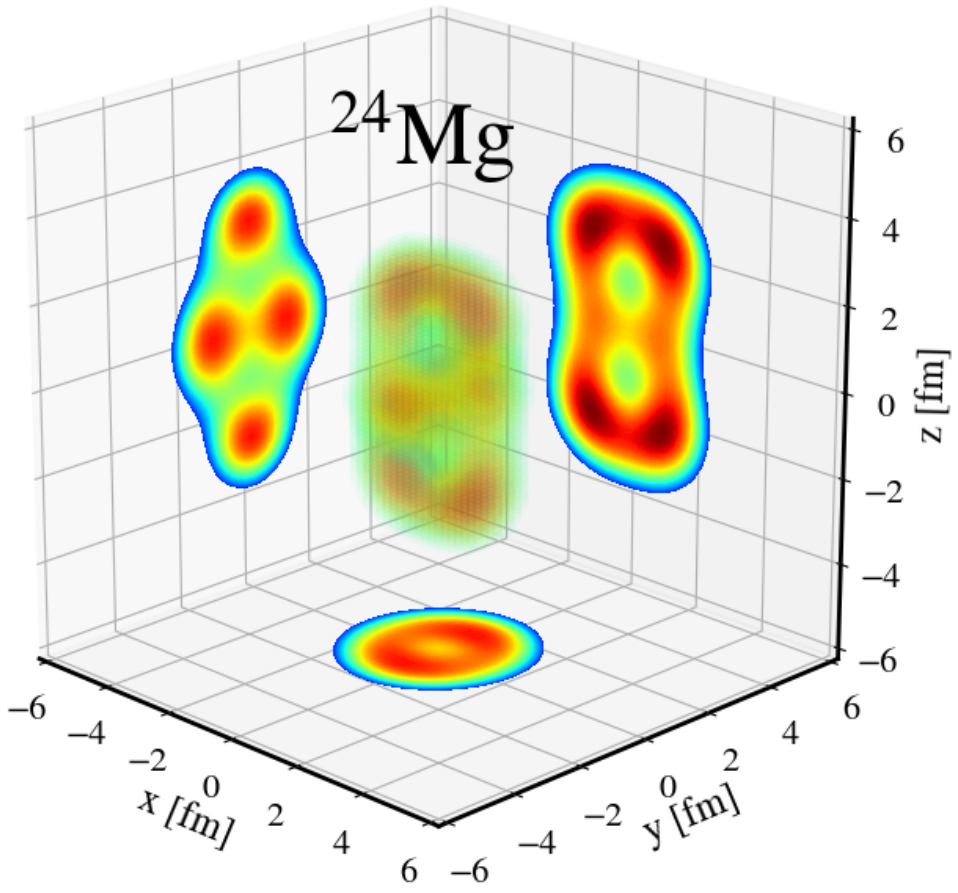

Figure 5.4: ^{24}Mg HFB one-body density. The plots at the planes show the value of the density at the origin.

The one-body density of ^{24}Mg at the triaxial minimum is sampled to investigate its ground state structure. The sampling boundaries are chosen as $[-10, 10]$ fm in every Cartesian direction, with a step of 0.1 fm. Figure 5.4 shows the density alongside its intersection with each of the Cartesian planes at the origin. Integrating all the density using the parallelepiped rule yields a value of 23.99985, which confirms that the integration limits are sufficiently big. From figure 5.4 we can see how at the naked eye 6 different clusters are formed. Such clusters can be divided into two opposing triangles, with two pairs of clusters centered at $z \approx \pm 2$ fm approximately forming the base of each triangle and the other two clusters showing at $z = 0$ fm and $y \approx \pm 1$ fm, which form the third vertex.

To confirm whether each of the vertices constitutes an α particle we integrate the one-body density first on the volume between $z = -1.05$ fm and $z = 1.05$ fm and then on the values $z > 1.05$fm. Table 5.2 shows the integration results, and figure 5.5 shows the integration limits superimposed to

Limits	$1.05\ \text{fm} \leq z \leq 1.05\ \text{fm}$	$1.05\ \text{fm} < z$	Total
$\int \rho(\boldsymbol{r}) d\boldsymbol{r}$	8.03	7.97	23.99

Table 5.2: Values of the integral of the one-body ^{24}Mg density for different integration limits

the HFB density at the origin planes. The results for each of the integration limits show essentially 8 particles per region. As parity is a good quantum number, $\rho(\boldsymbol{r}) = \rho(-\boldsymbol{r})$, so this confirms that each cluster is composed of 4 nucleons, which can be safely assumed to be α-clusters.

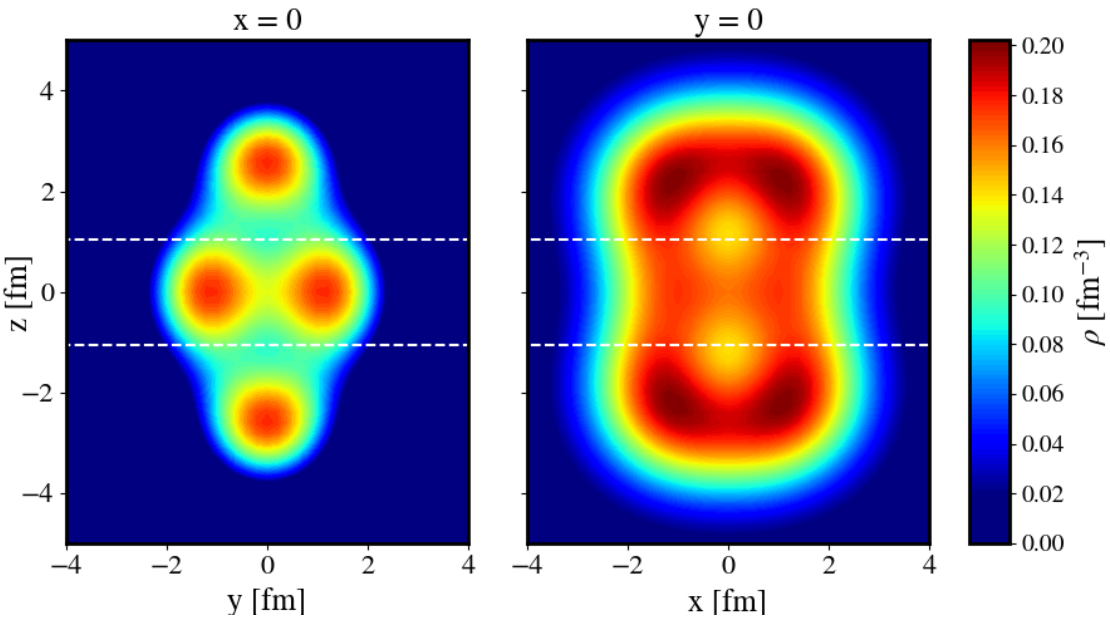

Figure 5.5: ^{24}Mg HFB one-body density at the x = 0 (left) and y = 0 (right) planes respectively. Dashed lines mark integration limits (see text for details).

A 6-α cluster structure like the one found cannot be reproduced with an axially symmetric solution. This makes triaxial deformation an essential ingredient for the HFB description of ^{24}Mg with this interaction.

5.1.4 Structure of the density in ^{32}S

The number of protons and neutrons in ^{32}S is the same as 8 times an α particle, which makes it also a likely candidate to show α-clustering. To check it, the HFB density is analyzed in the same way. The density at the global HFB minimum is plotted in figure 5.6. In this case, clustering phenomena do not manifest clearly. Indeed, the shape of the density is triaxial, with a central structure formed of six areas of higher density. Additionally, a halo-like structure forms at the $y = 0$ plane. However, the different structures are not well differentiated, with no integration limits found that result in an integer number of particles as was the case of ^{32}S.

The picture is however different if we check the density in the secondary minimum at $\beta = 1.00$. The density obtained at such minimum is plotted in figure 5.7. In that configuration, a clear $2 \times {}^{16}$O structure manifests. The two ^{16}O subunits show a blob over a halo-like circular structure. Although it would be tempting to identify the structure as an $\alpha + {}^{12}$C configuration, the integration of the density between $z = 0$ and $z = 2.2$ fm gives around 8 particles, which contradicts that description.

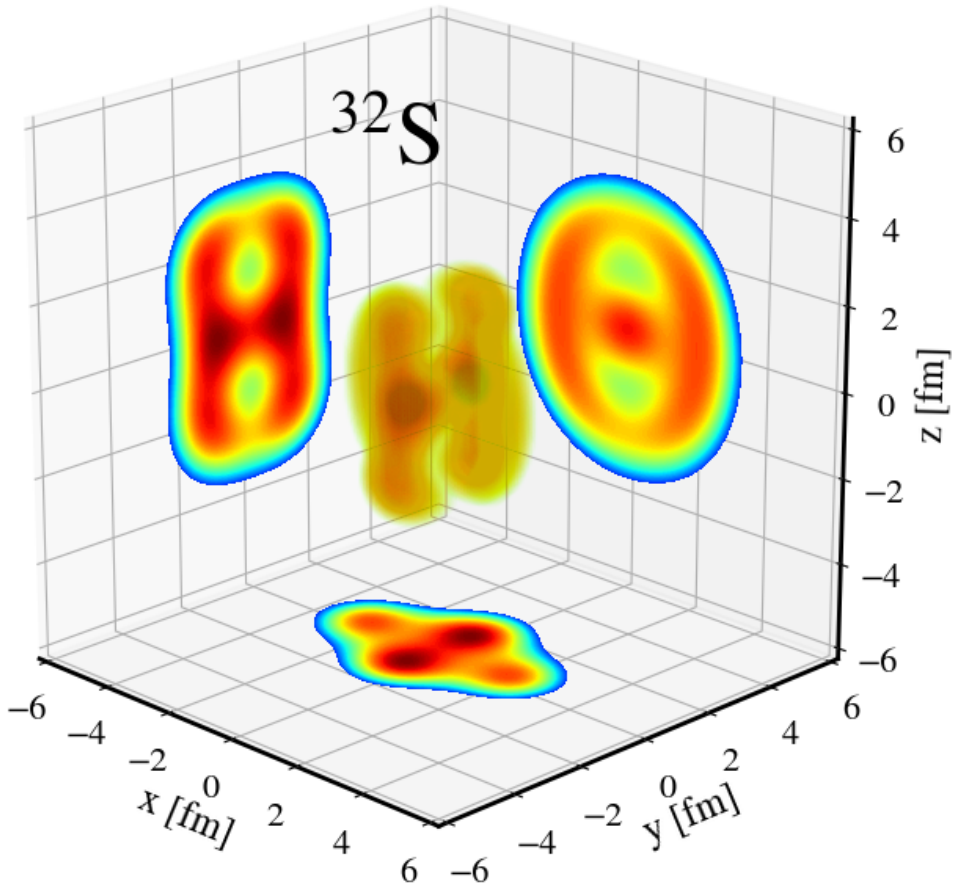

Figure 5.6: ^{32}S HFB one-body density at the absolute minimum of the PES. The plots at the planes show the value of the density at the origin.

Nevertheless, this is another example of a clustering phenomena, although for this one an axial description is sufficient to capture it. It remains to be seen whether breaking also parity could shed more light on the formed arrangements.

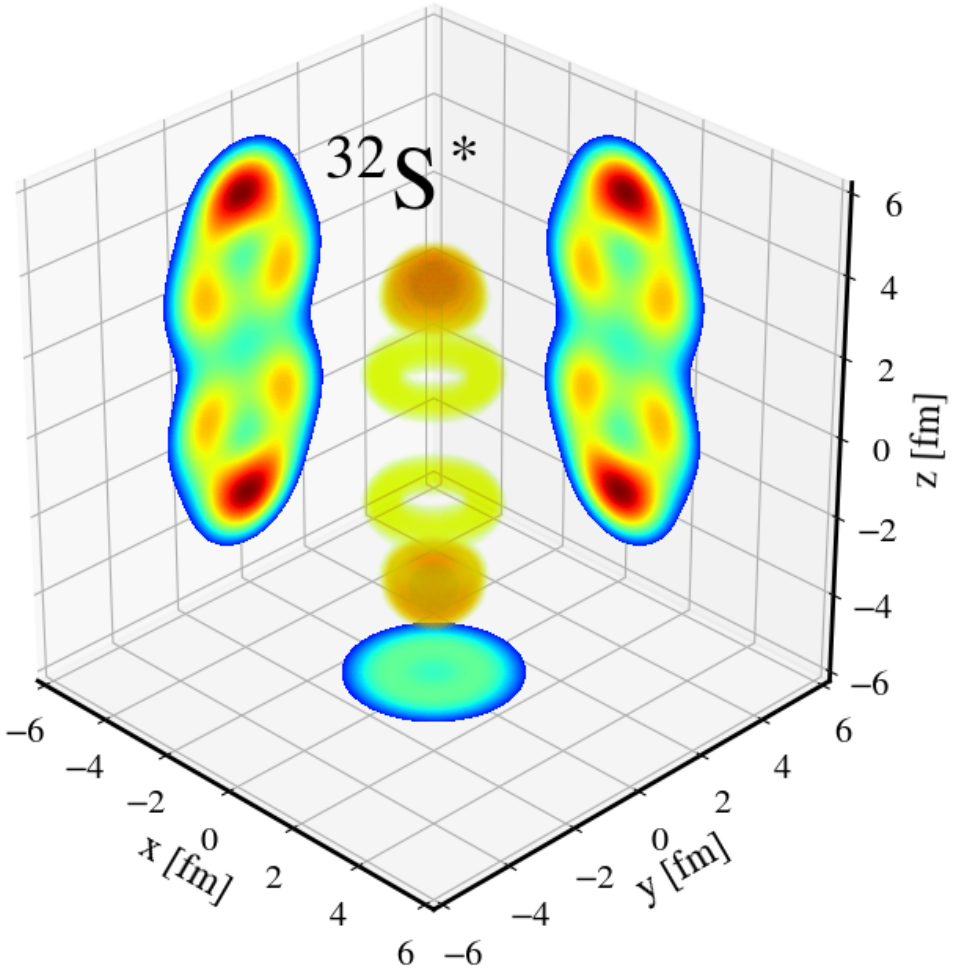

Figure 5.7: ^{32}S HFB one-body density at the second minimum of the PES. The plots at the planes show the value of the density at the origin.

5.2 Triaxial QRPA results

With a clearer picture of the crucial role of triaxiality in the mean-field description of these nuclei, its impact on the QRPA response can be better understood. QRPA calculations of the $E1-\gamma$ strength were performed in each of the nuclei, starting both at the triaxial minimum and the axial minimum[2]. The same considerations were used as in chapter 4, including the use of a smearing parameter of $\gamma_{smear} = 1.5$. Figure 5.8 shows the results, alongside the experimental data from [43].

First, a few words about the experimental data must be said: Only the data from referece [43] obtained after the year 2000 are shown. There is for both nuclei another measurement performed in the 1960s, but its shape is considerably different from the newer results, so it is omitted. The two different experimental series in ^{24}Mg show a similar distribution, with the three-peaked strength characteristic of triaxial nuclei [43, 119, 120]. ^{32}S displays multiple-peaked data as well, with at least four being identifiable.

The QRPA response in ^{24}Mg seems to, at least qualitatively, reproduce the shape of the strength of the experimental data, with the middle peak not being visible at least for the $\gamma_{smear} = 1.5$ MeV value used. That being said, the triaxial response better reproduces the hierarchy of the peaks and seems to push the strength towards the experimental data, especially when considering the low energy part. Meanwhile, in ^{32}S the improvement is not so clear. Both responses seem to consist of a main peak that does not change its position by much with different deformation.

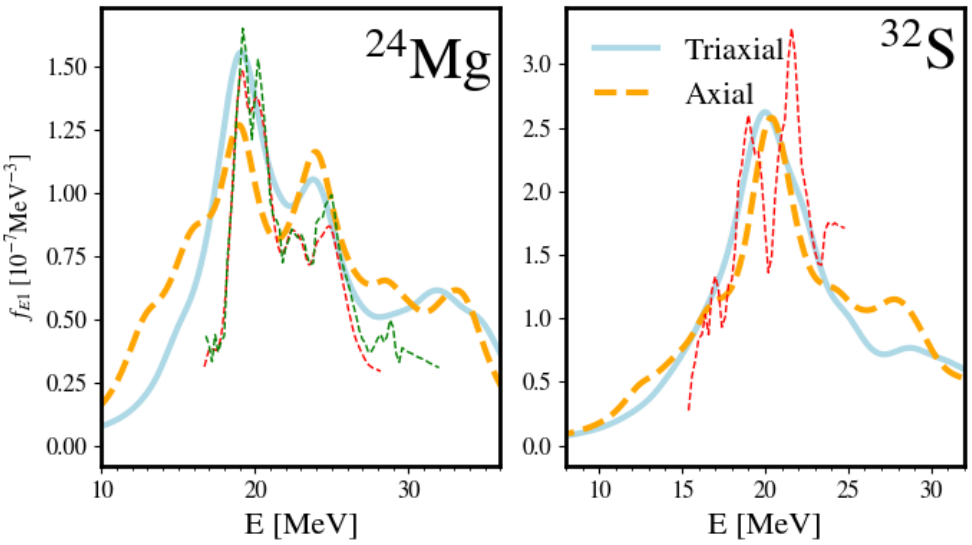

Figure 5.8: ^{24}Mg and ^{32}S E1 γ-strength function [29] at N3LO. Axial and triaxial results are compared. Experimental results from reference [43] measured after the year 2000 are shown as dashed lines.

For a more quantitative analysis, the value of the centroids, maxima, and widths of the strengths are compared in figure 5.9. For the case of ^{24}Mg, one can see that the centroid position is better reproduced, with the width of the strength over the experimental data and the maxima being almost unchanged. For ^{32}S, no quantitative improvement is observed. However, the strength in both cases has a complicated structure that gets hidden by the large smearing that is set on the FAM-QRPA calculation.

To disentangle the finer structure of the QRPA response, calculations with $\gamma_{smear} = 0.5$ MeV and an energy step of 0.1 MeV were performed. This, however, makes the maximum of the QRPA

[2]Minimum for $\gamma = 0$

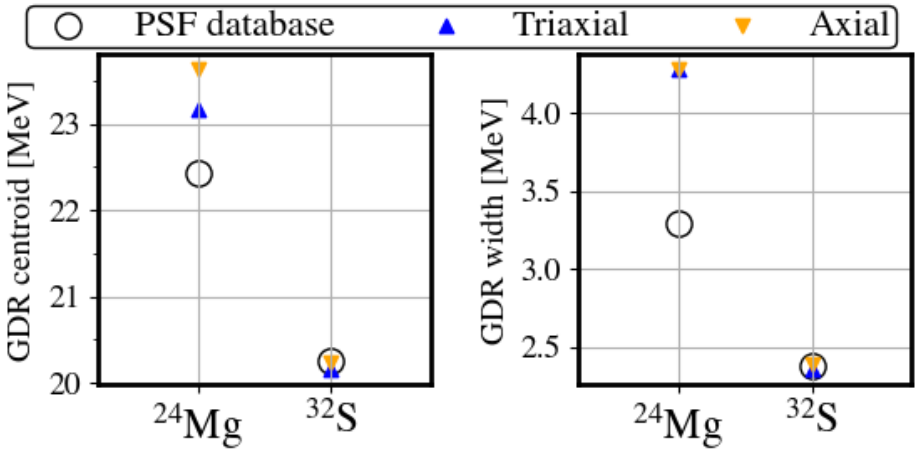

Figure 5.9: ^{24}Mg and ^{32}S E1 γ-strength centroid and width calculated with the chiral interaction of reference [29] at N3LO. Axial and triaxial results are compared.

strength much higher than the experimental data. To be able to compare them, the QRPA strengths are multiplied by an arbitrary 0.5 normalization factor.

The results for ^{24}Mg are plotted in figure 5.10 superimposed to the two most recent experimental series from the PSF database [43]. We can see how at this smearing it can be observed that the triaxial response shows a clearer third peak between the two main maxima. The maximum at 18 MeV is not composed of a single contribution. This is also the case in both experimental runs, where the maximum splits into two. The hierarchy of the two main peaks is also better reproduced with the triaxial response.

The modification of the strength in ^{32}S is much more obvious with this smearing. This can be seen in figure 5.11, where the strength is plotted. On the one hand, while the axial response shows a clear central single peak at around 20 MeV, the triaxial response splits, with two main maxima between 19 and 23 MeV. However, the hierarchy of both these peaks is inversed concerning the experimental response. Other maxima at 16.5 and 25 MeV appear for both symmetries which coincide with maxima in the strength function. However, while these two maxima are of the same height in the QRPA response, in the experiment the maximum at 25 MeV is much bigger. In short, although not providing a total reproduction of the strength, it seems that triaxiality allows for the capturing of important features, especially the maxima splitting.

5.2.1 Gradual evolution of the E1 response with the deformation

To conclude the study, to understand whether the change of the strength is gradual or sudden with deformation, different calculations of the strength were done for ^{24}Mg by constraining $\beta = 0.58$ and γ to different values from 0° to 14°. The resulting strengths are shown in figure 5.12. As we can see, the apparition of the third peak is rather sudden, happening near the triaxial minimum. The formation of a clear second peak does not happen until $\gamma >10°$. It has to be taken into account the fact that the strength at $\gamma =0°$ and the one shown in figure 5.10 are not the same, as β is slightly different between the two.

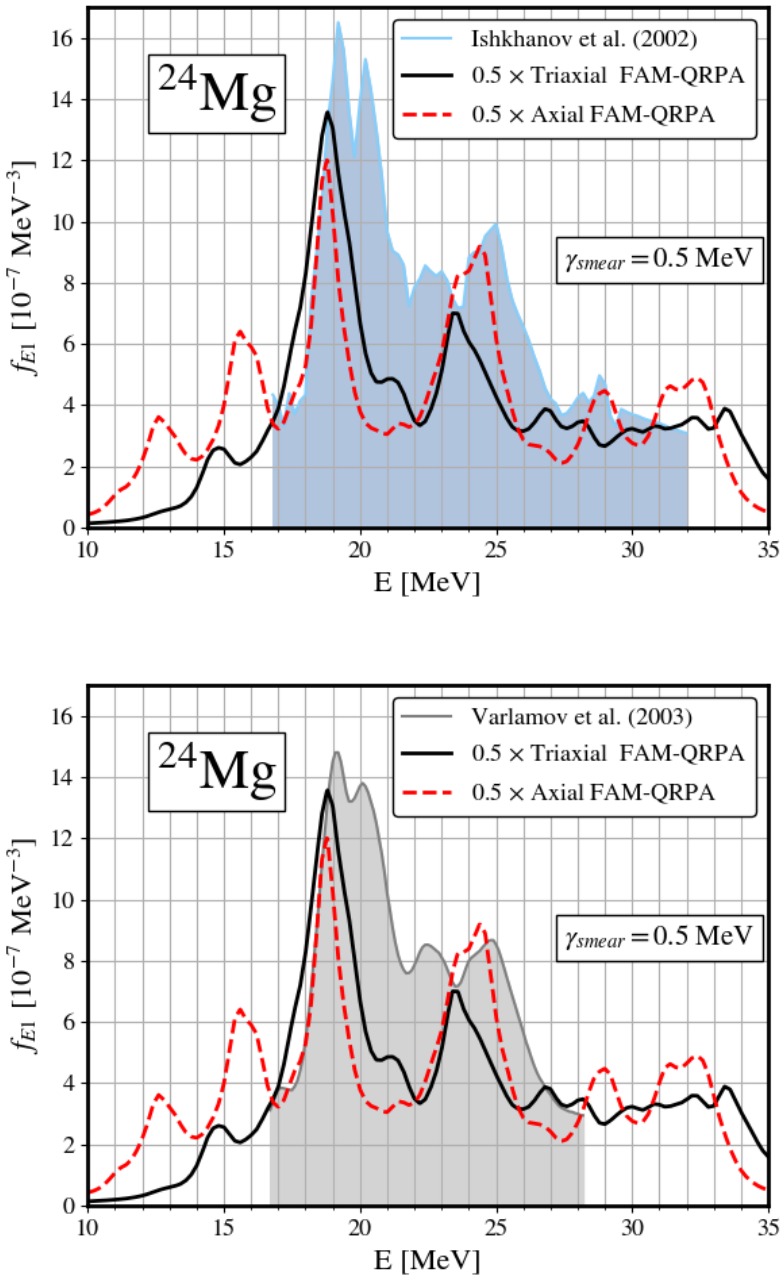

Figure 5.10: ^{24}Mg QRPA-$E1$ strength calculated using γ_{smear} = 0.5 MeV. The two more recent experimental measurements from [43], [121, 122] are shown.

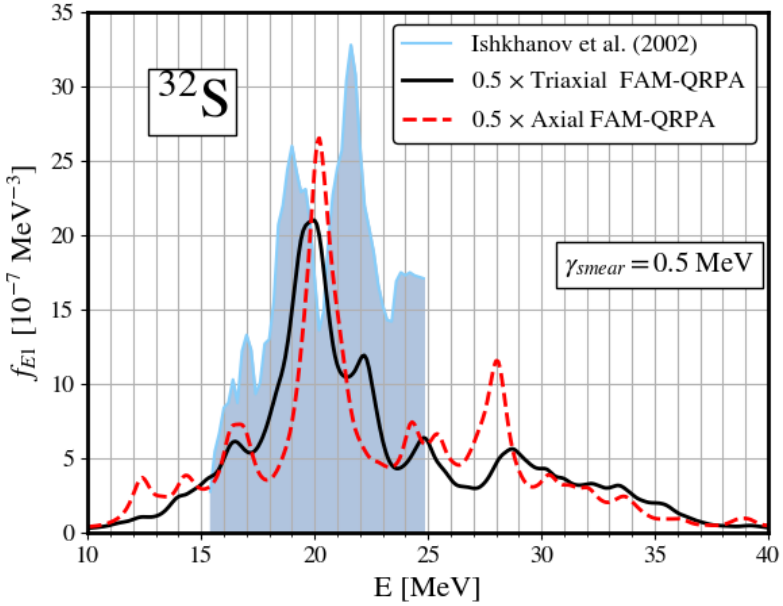

Figure 5.11: ^{24}S QRPA-$E1$ strength calculated using $\gamma_{smear} = 0.5$ MeV. The more recent experimental measurements from [43], [122] are shown.

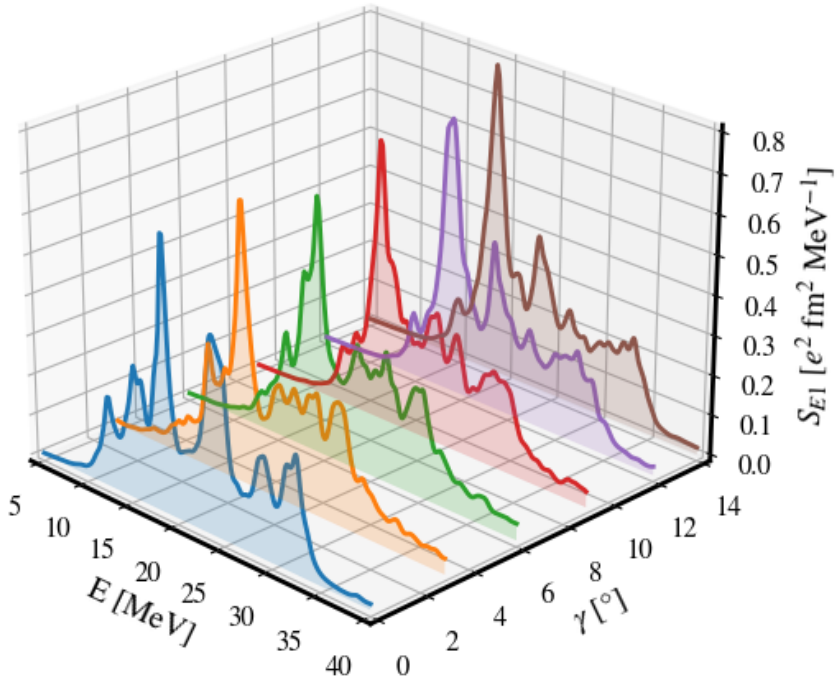

Figure 5.12: ^{24}Mg E1 γ strength at $\beta = 0.58$ for varying values of triaxial deformation parameter γ. $\gamma_{smear} = 0.5$ MeV is used.

5.3 Conclusions

In this chapter we have studied the impact of the consideration of triaxiality in the chiral HFB ground state and QRPA E1-strength of ^{24}Mg and ^{32}S using the interaction from reference [29]. This is the first time that this has been done using chiral interactions. The following conclusions have been drawn:

- Both ^{24}Mg and ^{32}S show a clear triaxial minimum in their chiral HFB PES. For ^{32}S, the potential is shown to be softer, with a smaller gap with respect to the axial minimum.
- Triaxial QRPA at a wide smearing of γ_{smear} = 1.5 MeV seems to better describe the centroid position of the E1 strength of ^{24}Mg. For ^{32}S, the improvement is not so clear using such a big smearing.
- The triaxial HFB ground state of ^{24}Mg has been shown to display a six-α cluster structure. In ^{32} S, although the HFB minimum does not show a cluster structure, the second minimum of the PES displays a $2 \times {}^{16}$O configuration.
- Using a finer smearing parameter it was observed how the experimental strengths were better reproduced in both cases. In the ^{24}Mg triaxial response a clearer third maximum appears between the two main peaks, while in ^{32}S the single dominant peak is split.

^{24}Mg and ^{32}S are only two examples of the many nuclei that display a triaxial HFB minimum in the current range of applicability of chiral interactions. An example is the Germanium isotopic chain, which was recently shown to contain many triaxialy-deformed nuclei at the HFB level with the EM1.8/2.0 interaction [123]. Moreover, the `PAN@CEA` code used in this work can break also parity, which could be used to further study the formation of clusters. The behavior of highly deformed chiral QRPA could then be assessed in a large quantity of nuclei.

Part III

New formal and numerical developments

Chapter 6

Exact Jacobi-Davidson-QRPA method

During this thesis, the finite amplitude method (FAM) has been used to evaluate QRPA γ-strength functions. Strength functions are just one of the observables that can be obtained from QRPA, others being low energy spectroscopy of collective states [85], correlation energies [105] (see chapter 6) and so on. FAM is the most popular of the iterative QRPA methods that have been developed in the last 15 years, alongside the *Arnoldi* [62, 63] and the *Chebyshev kernel polynomial* (CKP) [64] methods. All of them have in common that they can extract specific quantities without having to solve the full matrix-QRPA problem. In the case of FAM, CKP, and the first implementation of Arnoldi, the QRPA response is obtained in an iterative and fast way. In the second implementation of Arnoldi and the *complex plane integration*-FAM method [68], the extracted quantity is a bunch of the eigenpairs of the QRPA matrix, i.e. the X^n , Y^n amplitudes and the phonon energies ω_n. In all these cases this comes at a very reduced computational cost compared to the full matrix problem. These two last methods, although robust, can further be improved. On the one hand, complex plane integration-FAM requires a general idea of the location of the target eigenvalues before extracting them and has difficulties on the regions of the spectrum with many eigenvalues clustered together. On the other hand, the Arnoldi method does not exploit the fact that FAM gives us indirect access to the *inverse* QRPA matrix, which allows the possibility of applying some very powerful eigenvalue extraction methods.

In this chapter, a new method for the extraction of the QRPA amplitudes based on FAM is proposed. This method is not limited to a certain region of the spectrum and it does not require to know the position of the poles beforehand. Its core is the application of the Jacobi-Davidson method for the extraction of eigenvalues [124, 125]. Jacobi-Davidson does not require an explicit expression of the matrix to diagonalize, only its matrix-vector product. The fact that the matrix-vector product of both the QRPA matrix and its inverse are available through FAM is exploited. The method, modified for QRPA-like eigenvalue problems, is presented, and a proof of principle is performed.

6.1 Main idea: Matrix inversion through FAM

As it was introduced in chapter 1, the QRPA problem consists in solving the generalized eigenvalue problem

$$Mx_n = \omega_n \nu x_n. \tag{6.1}$$

where each of the terms stands for

$$M = \begin{pmatrix} \mathbf{A} & \mathbf{B} \\ \mathbf{B}^* & \mathbf{A}^* \end{pmatrix}, \quad x = \begin{pmatrix} X(\omega) \\ Y(\omega) \end{pmatrix}, \quad \nu = \begin{pmatrix} I & 0 \\ 0 & -I \end{pmatrix} \tag{6.2}$$

and the n index in x and ω standing for them being QRPA eigensolutions . On the other hand in the FAM algorithm, the value of x is solved from the equation

$$(\epsilon - \omega\nu)x + \delta\mathfrak{h} = -\mathfrak{f}, \tag{6.3}$$

for a given value of ω and $\mathfrak{f}$. Here $\mathfrak{f}$ and $\delta\mathfrak{h}$ stand for

$$\mathfrak{f} = \begin{pmatrix} F^{20}(\omega) \\ F^{02}(\omega) \end{pmatrix} \quad \delta\mathfrak{h} = \begin{pmatrix} \delta H^{20}(\omega) \\ \delta H^{02}(\omega) \end{pmatrix}. \tag{6.4}$$

and ϵ is the diagonal matrix containing *twice* all the two-quasiparitcle energies, which was defined in 1.57. The FAM master equation is nothing more than the linear response equation written in terms of a differential variation of the mean-field $\delta\mathfrak{h}$. This is easily seen by making the substitution $\delta\mathfrak{h} = (M - \epsilon)x$. Then equation 6.3 becomes

$$(M - \omega\nu)x = -\mathfrak{f}, \tag{6.5}$$

An important remark to be made here is that ν is not positive definite. This means that the product $u^\dagger \nu v$ is not necessarily positive and can be 0. This will have consequences in the extraction of the eigenvalues.

The main question that we want to answer in this chapter is: *Which are the ways in which FAM can help us to solve equation 6.1, at least for some eigenpairs?*. One possible answer is the pole integration of the FAM strength [67] or the Arnoldi method. Here, we propose to exploit the fact that *through FAM we have access to the matrix-vector product of the QRPA matrix and its inverse into any arbitrary vector*. This is achieved in the following way:

- Given an arbitrary vector u, $(M - \nu\omega)u$ can be evaluated by calculating the induced $\delta\mathfrak{h}$ associated to $x = u$ and then substituting it in 6.3.
- Given an arbitrary vector u, $(M - \nu\omega)^{-1}u$ can be evaluated by solving the FAM algorithm taking as the perturbation of the Hamiltonian $-f = u$.

Having established that this opens the way to use any of the well-known eigenvalue extraction algorithms for which only the matrix-vector product of the target matrix is needed, not its explicit form. The method chosen in this work is the Jacobi-Davidson method, which we describe in the next pages.

6.2 The Jacobi-Davidson method for QRPA matrices

The Jacobi-Davidson (JD) method was introduced in the seminal work by Sleijpen and van der Vorst [124]. One of its advantages over other iterative solvers such as Lanczos and Arnoldi is that it is particularly good at extracting interior eigenpairs [125]. The other aforementioned methods usually require to factorize the matrix, which may not be feasible in many cases. This is our case, as the QRPA matrix is not explicitly built. JD has been used for the diagonalization of sparse almost diagonal matrices in the context of quantum chemistry, which makes it suitable for the QRPA problem. The exact version of the Jacobi-Davidson method can be proven to converge at least cubically locally [126]. This is because JD can be proven to be equivalent to the well-known Rayleigh-Quotient-Iterations method (RQI) if we restrict ourselves to a search space spanned by a single vector. As understanding RQI can ease the comprehension of the main steps behind JD, we present it briefly in the following pages.

6.2.1 Rayleigh quotient iterations

Rayleigh Quotient Iterations (RQI) is an algorithm that finds an eigenpair (ω, x) of a given matrix pencil (M, ν) starting from a trial vector u_0. Given a matrix $M \in \mathbb{C}^{n\times n}$ and a pseudo-metric[1] $\nu \in \mathbb{R}^{n\times n}$, the *Ritz value* of a vector $u \in \mathbb{C}^n$ is defined as

$$\rho(u) = \frac{u^\dagger M u}{u^\dagger \nu u}. \tag{6.6}$$

The Rayleigh quotient method is based on the fact that $\rho(u)$ is stationary when $u = x_n$ is a generalized eigenvector of M, ν, with $\rho(x_n) = \omega_n$ being its correspondent eigenvalue (see appendix B). In other words, x_n is an extremum of $\rho(u)$. The main idea behind RQI is that if we start with a trial eigenvector u_0, then the iteration

$$u_{k+1} = (M - \rho_k \nu)^{-1} \nu u_k \tag{6.7}$$

converges cubically to a generalized eigenpair of M. A proof of this is shown in appendix B. Here we denoted $\rho_k \equiv \rho(u_k)$ for concision. Each of the pairs ρ_k, u_k in the iterative process is known as a *Ritz pair*. An example of an implementation of RQI is shown in algorithm 2. One of the shortcomings of this method is the fact that ν-normed vectors may have 0 norm even if $u_k \neq 0$. RQI cannot deal with this situation, and if the Ritz vector is 0 normed, then the algorithm fails.

Algorithm 2: Reyleigh quotient iterations-QRPA

Finds a QRPA eigenpair (ω, x) starting from the trial vector u_0 for a given tolerance `tol`.
If the number of iterations surpasses n_{max}, the algorithm fails.

Data: u_0, `tol`, n_{max}
Result: ω, x
$k \leftarrow 0$
$u_0 = u_0 / \sqrt{|u_0^\dagger \nu u_0|})$
while $k < k_{max}$ **do**
  if $|u_k \nu u_k|$ <`tol` **then**
    Algorithm fails
    break ;
  $\rho_k = u_k^\dagger M u_k / (u_k^\dagger \nu u_k)$;
  $r_k = (M - \rho_k \nu) u_k$;
  if $r_k^\dagger r_k$ <`tol` **then**
    Solution found
    $\omega = \rho_k$
    $x = u_k$
    break ;
  $u_{k+1} = (M - \rho_k \nu)^{-1} \nu u_k$;
  $u_{k+1} = u_{k+1} / \sqrt{|u_{k+1}^\dagger \nu u_{k+1}|}$;
  $k \leftarrow k + 1$
end

Although RQI has good convergence properties, it only calculates one eigenpair and then it stops. On top of that, there is no guarantee that the process will converge to the eigenpair that we are interested in. To have more control of the convergence, usually ρ_k is fixed to a target value τ for the first iterations of the process. The Jacobi-Davidson method is an improved version of RQI that can deal with the calculation of several eigenpairs.

[1] We call ν a pseudo-metric because it is not positive definite, which means that the product $u^\dagger \nu u$ can be smaller than 0.

6.2.2 Derivation of the Jacobi-Davidson method for QRPA matrices

Jacobi-Davidson (JD) is a *subspace* method. Such algorithms implement a two-stepped iteration: The subspace *extraction* and *expansion*. In the former, an estimate of the best solution for the eigenvector problem is proposed within a restricted subspace $\mathcal{U}$ of much lower dimension than the matrix to diagonalize. In the second step, the subspace expansion, a new basis vector for the $\mathcal{U}$ subspace is added most efficiently.

Extraction

We want to approximate the eigenvector as a linear combination of vectors in a search space $\mathcal{U}$ whose dimension is much smaller than n. This space is spanned by the k column vectors included in the matrix U so that $k \ll n$. The current approximation to the eigenvalue can be written as

$$u = Uc, \quad \text{with } c^\dagger c = 1. \tag{6.8}$$

We would like to optimize the vector within the search space, i.e. we would like to minimize the *residual*

$$r \equiv (M - \rho\nu)u. \tag{6.9}$$

To do so, we impose that the residual is Euclidean orthogonal to the search space

$$r \perp \mathcal{U} \rightarrow U^\dagger r = 0 \tag{6.10}$$

This is the so-called *Ritz-Galerkin condition*. Multiplying from the right 6.9 by $U^\dagger$ one then obtains

$$\underbrace{U^\dagger M U}_{\equiv H} c = \rho \underbrace{U^\dagger \nu U}_{\equiv N} c, \tag{6.11}$$

resulting in the $k \times k$ generalized eigenvalue problem

$$\boxed{Hc = \rho N c.} \tag{6.12}$$

What we obtain then is an optimized set of eigenvectors of M, ν. Normally, JD will target a specific part of the spectrum close to a target value τ. For the next iteration of the algorithm, Ritz pairs obtained from equation 6.12 are ordered with respect to their distance to τ and only the closest one is chosen.

Expansion

Now we would like to expand the search space. To do so, we consider the current Ritz vector u, and its Ritz value $\rho(u)$. We would like to find which is the Ritz vector t that when added to u results in an eigenvalue

$$M(u + t) = \omega_n \nu(u + t). \tag{6.13}$$

with the condition that $t^\dagger \nu u = 0$. We can write

$$(M - \rho\nu)\, t = -\underbrace{(M - \rho\nu)\, u}_{=r} + (\omega_n - \rho)\nu u + (\omega_n - \rho)\nu t, \tag{6.14}$$

Where we drop the u dependence of ρ for concision. In appendix B it is shown that, analogously to the RQI, the last term in the right-hand side decreases cubically as $\rho \rightarrow \omega_n$, so it can be neglected. Let $\eta_u = u^\dagger \nu u$. Multiplying on the left by the pseudoprojector $I - \eta_u \nu u u^\dagger$ one gets

$$(I - \eta_u \nu u u^\dagger)(M - \rho\nu)t = -r. \tag{6.15}$$

By using the condition $u^\dagger \nu t = 0$, then

$$(I - \eta_u \nu u u^\dagger)(M - \rho\nu)(1 - \eta_u u u^\dagger \nu)t = -r. \tag{6.16}$$

This is the so-called *correction equation*. If we now want to calculate several eigenvalues, we would like to ensure that the t vector is not only ν-orthogonal to the current Ritz vector but also all the already found eigenvalues. Let Q be the matrix of all found eigenvalues and Ξ the diagonal matrix of their norms. Let the $\tilde{Q}$, $\tilde{\Xi}$ matrices be defined as

$$Q = \begin{pmatrix} x_1 & x_2 & x_3 & \dots \end{pmatrix}, \quad \Xi = \begin{pmatrix} \eta_{x_1} & & & \\ & \eta_{x_2} & & \\ & & \ddots & \end{pmatrix}, \quad \tilde{Q} = \begin{pmatrix} u & Q \end{pmatrix}, \quad \tilde{\Xi} = \begin{pmatrix} \eta_u & \\ & \Xi \end{pmatrix}, \tag{6.17}$$

where this time the condition $\tilde{Q}^\dagger \nu t$ is fulfilled. This leads to the multiple eigenvalue form of the correction equation

$$\boxed{(I - \nu\tilde{Q}\tilde{\Xi}\tilde{Q}^\dagger)(M - \rho\nu)(1 - \tilde{Q}\tilde{\Xi}\tilde{Q}^\dagger\nu)t = -r} \tag{6.18}$$

In most of the applications of JD, the correction equation is solved only approximately. In that case, JD can be ensured to converge quadratically. However, thanks to the FAM, equation 6.18 can be solved exactly at the leading cost of a single FAM call, as equation 6.15 can be rendered into the form [124]

$$t = \alpha(M - \rho\nu)^{-1}\nu u - u. \tag{6.19}$$

with $\nu_u \alpha \equiv u^\dagger (M - \rho\nu)^{-1} t$, which in single-eigenvector case is a scalar. In appendix B it is shown how to exactly solve the correction equation for the multiple eigenvalue case with only one FAM call. If we ignore the optimization on the $\mathcal{U}$ space, then JD is as efficient as RQI, i.e. it converges cubically locally. This is because 6.19 is equivalent to an iteration of RQI. One can see this substituting $u_k = u$ and $u_{k+1} = u + t$ in equation 6.7, α becoming an unimportant normalization constant. By also including the subspace optimization, JD becomes an accelerated RQI which can take care of the calculation of several eigenvectors at the same time.

Orthogonalization

Having obtained a new search-space vector t, we would like to add it to U. To do so, it is necessary to ν-orthogonalize it with respect to all the vectors already included in U. We do this via a stable Gramm-Schmidt, which is laid out in algorithm 3.

Algorithm 3: νCGS stable indefinite Gramm-Schmidt

ν-orthogonalizes t with respect to all column vectors in the matrix U
Data: t,U, Ξ
Result: u, η_u with $U^\dagger \nu u = 0$
$u \leftarrow (I - U\Xi U^\dagger \nu)t$;
$u \leftarrow u / \sqrt{|u^\dagger \nu u|}$;
$\eta \leftarrow \text{sign}(u^\dagger \nu u)$

With all the different components on the table, the JD-QRPA can be built, as it is shown in algorithm 4. In our current implementation, no restarts of the algorithm are implemented, although many have been proposed in the literature [126]. To improve convergence, the Ritz value ρ is left fixed for the first iterations. This ensures that the eigenvalues found are located in the region of interest.

Having proposed a version of JD for QRPA, in the next section, we test its numerical feasibility.

Algorithm 4: Exact Jacobi-Davidson-QRPA

Finds the p closest QRPA-eigenvalues to target value τ from starting trial vector u_0

Data: u_0, p, τ, `tol`

Result: Ω, Q, with $\Omega = \left(\omega_1 \dots \omega_p\right)$ and $Q = \left(x_1 \dots x_p\right)$

$k \leftarrow 0$; $j \leftarrow 0$; $\Omega \leftarrow ()$; $Q \leftarrow ()$; $\Xi \leftarrow ()$;

$u_0 \leftarrow u_0 / \sqrt{\left|u_0^\dagger \nu u_0\right|}$; $U \leftarrow u_0$; $q \leftarrow u_0$;

$\eta_0 \leftarrow u_0^\dagger \nu u_0$; $\eta_q = \eta_0$; $\rho \leftarrow \eta_0^u \, u_0^\dagger M u_0$; $r \leftarrow (M - \rho\nu)u_0$;

while $k < p$ **do**

  $\tilde{Q}_k = (Q \; q)$; $\tilde{\Xi}_k \leftarrow (\Xi_k \; \eta_q)$;

  Solve $(I - \nu\tilde{Q}_k\tilde{\Xi}_k\tilde{Q}_k^\dagger)(M - \omega\nu)(I - \tilde{Q}_k\tilde{\Xi}_k\tilde{Q}_k^\dagger\nu)t = -r$;

  $u_{j+1}, \eta_{j+1} = \nu\mathrm{CGS}(U_j, \Xi_j, t)$;

  $U_{j+1} \leftarrow (U_j \, u_{j+1})$; $\Xi_{j+1} \leftarrow (\Xi_j \, \eta_{j+1})$;

  $H_{j+1} = U_{j+1}^\dagger M U_{j+1}$;

  $N_{j+1} = U_{j+1}^\dagger \nu U_{j+1}$;

  $j \leftarrow j + 1$;

  Solve $Hc_i = \tilde{\rho}_i N c_i$;

  Order $\{\tilde{\rho}_i, c_i\}$ by increasing distance of ρ_i to the target value τ

  for $i < j$ **do**

    $q \leftarrow U_{j+1} c_i$;

    $\rho \leftarrow \tilde{\rho}_i$;

    $r \leftarrow (M - \rho\nu) \, q$;

    if $r^\dagger r <$ `tol` **then**

      $k \leftarrow k + 1$;

      $\omega_p = \rho_i$; $x_p = q$;

      $\Omega = (\Omega \, \omega_p)$; $Q = (Q \, x_p)$;

    else

      break ;

    end

  end

  if $k = p$ **then**

    break ;

end

6.3 Numerical performance

As a part of this work, the JD-QRPA algorithm has been implemented in the `PAN@CEA` [79] code. The code solves the HFB and FAM equations with symmetry-breaking mean-fields. In our examples, the QRPA-FAM is built on top of an axially symmetric HFB, so that $\delta\mathfrak{h}$ is divided into K^π blocks. In the following, we show the results of several numerical tests.

6.3.1 General observations

The Jacobi-Davidson algorithm shows very high performance in extracting QRPA eigenvalues, with only a couple of iterations necessary on average per eigenvalue. The leading cost of each JD-QRPA iteration is the FAM call necessary to solve exactly the correction equation (6.18). Setting the ritz value constant $\rho = \tau$ for the first iterations greatly helps improve the convergence into the desired region of the spectrum. Nevertheless, there are two main pitfalls that may arise. The first is

that the spurious 0 energy solutions may induce numerical instabilities. This can be solved by any of the methods for the extraction of the spurious states that have been used in the other iterative methods [65, 69]. Second, whenever the Ritz vector is very close to an actual eigenvalue, the FAM algorithm may take way longer to converge. This can have a big impact on the efficiency. To deal with this, adding a small complex value to the Ritz vector seems to be enough to tame this, especially in the lower part of the spectrum.

6.3.2 Comparson with Shell-Model Matrix-QRPA

As a benchmark of the numerical accuracy of the method, the QRPA M1-strength of ^{20}Ne obtained with JD-QRPA has been compared with the one obtained with matrix-QRPA done on top of an HFB state obtained with the code `HF-SHELL`[127]. The *sd* valence space shell-model interaction USDB was used [128]. The results for several levels in each of the K blocks can be seen in table 6.1. As we can see, the results are identical within 5 decimal digits. It has to be noted that the model space of this calculation is very small. To prove that the same accuracy is obtained with bigger spaces, a comparison with FAM is performed.

K	E (JD) [MeV]	E (SM-QRPA) [MeV]	B_{M1} (JD) [μ_N^2]	B_{M1} (SM-QRPA) [μ_N^2]
0	10.406418	10.406417	0.000190	0.000190
0	10.949270	10.949270	0.096031	0.096031
0	13.298152	13.298153	0.000941	0.000941
0	14.525524	14.525526	0.334619	0.334622
1	8.898729	8.898731	0.783673	0.783673
1	9.536392	9.536393	0.000334	0.000334
1	11.172634	11.172633	0.028456	0.028456
1	12.586020	12.586019	0.000212	0.000212
1	14.835711	14.835712	0.014002	0.014002
1	15.163259	15.163258	0.000028	0.000028
1	16.503927	16.503927	0.025487	0.025487

Table 6.1: Energy of the QRPA states E and their corresponding magnetic transition calculated with the Jacobi-Davidson (JD) algorithm and with shell-model QRPA (SM-QRPA) using the `PAN@CEA` and `HF-SHELL` codes respectively. States are ordered with respect to their angular momentum projection K.

6.3.3 Comparison with FAM

As a proof of concept, a calculation of the monopole response in ^{20}Ne has been done using the JD algorithm and compared to the FAM result. This is shown in figure 6.1. The eigenvalues up to 50 MeV of the $K^\pi = 0^+$ block of the QRPA matrix were calculated using the JD-QRPA algorithm with the interaction of reference [29] expanded with $e_{max} = 6$. A tolerance of `tol`$= 10^{-5}$ was set. Then, the associated isoscalar-monopole response of each state is calculated for each peak and the obtained result is folded with a standard Lorentzian of half-width $\Gamma/2 = 0.5$ MeV. The FAM response was then calculated using the same parameters with a smear of $\gamma_{smear} = 0.5$ MeV. The results are shown to be identical apart from numerical noise. The number of FAM calls needed per eigenvalue is 1.4, which is much lower than with the method in reference [67] and [63], especially for the low-lying part of the strength. In this example, as a test, no small complex part was added to the sampled energy. Consequently, the number of iterations needed is much larger. This is shown

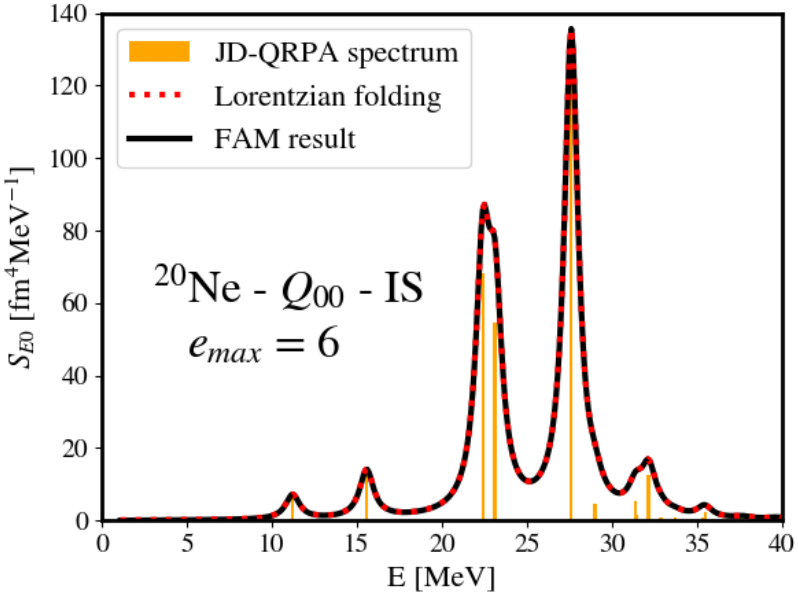

Figure 6.1: $E0$-QRPA response calculated via the FAM and the JD methods. The JD discrete spectrum has been folded with a standard Lorentzian of $\Gamma/2 = 0.5$ MeV, which is the same as the smearing chosen for the FAM calculation.

in figure 6.2, where the number of iterations in the FAM algorithm per sampled energy is shown. As we see, for high energies the number of iterations explodes. This may have to do with the fact that the QRPA spectrum is way more dense at those energies. However, for the low-lying spectrum, the number of iterations does not surpass 100 until the 11 MeV threshold, which makes the method better suited to extract low-energy collective states.

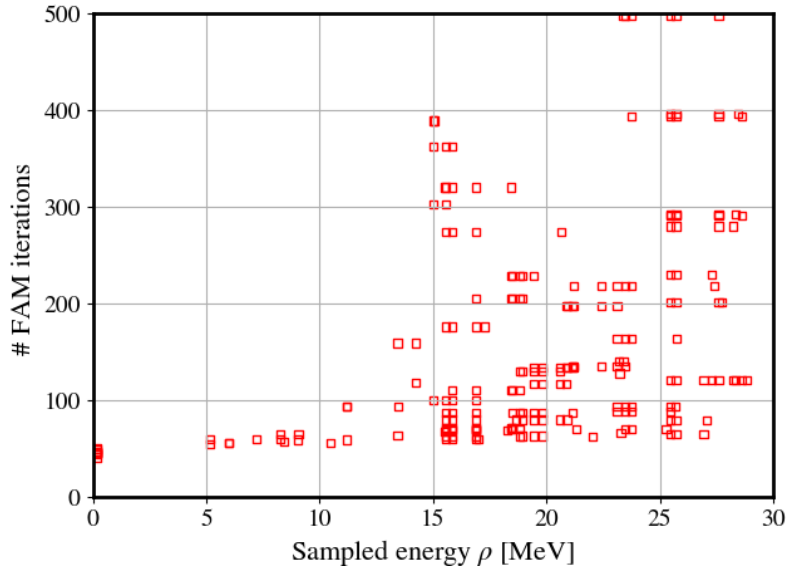

Figure 6.2: Number of FAM calls in each of the iterations of the JD-QRPA algorithm as a function of the sampled energy

Having been able to obtain a response equivalent to FAM-QRPA, we know to test the method

in a realistic case.

6.4 Application to a realistic case: ^{238}U

We would like to test now the ability of JD to produce some low QRPA energy levels as an alternative to matrix-QRPA. As an application to a realistic case, the first 10 0^+ eigenvalues were extracted for ^{238}U using the Gogny-D1M interaction with 13 major harmonic oscillator shells. A tolerance of `tol`$= 10^{-3}$ was set for the JD algorithm. Figure 6.3 shows the eigenvalues found alongside their value for the $E0$ strength transition. A small complex shift of 0.05 MeV was used to help convergence. [2]. The algorithm took 9 iterations to find the 10 eigenvectors, with an average of 55 FAM iterations per JD iteration. The small complex shift proved essential, as if not added the number of needed iterations increased tremendously even for the low spectrum. The full calculation was achieved in 1 CPU with a memory consumption of 6.8 GB in approximately 6 and a half hours. As a comparison, to obtain the full spectrum with the matrix formulation with the same model space size, reference [60] quotes that 45h with 1024 CPUs were needed with computers of the year 2016. This implies a reduction of computational resources necessary of several orders of magnitude. It has also to be taken into account that in many M-QRPA applications a cutoff on the energy of the quasiparticle pairs is imposed. This is done as a compromise to achieve numerical tractability. Our case is equivalent to not imposing any cutoff at all, so in a way, they are more precise than many matrix implementations.

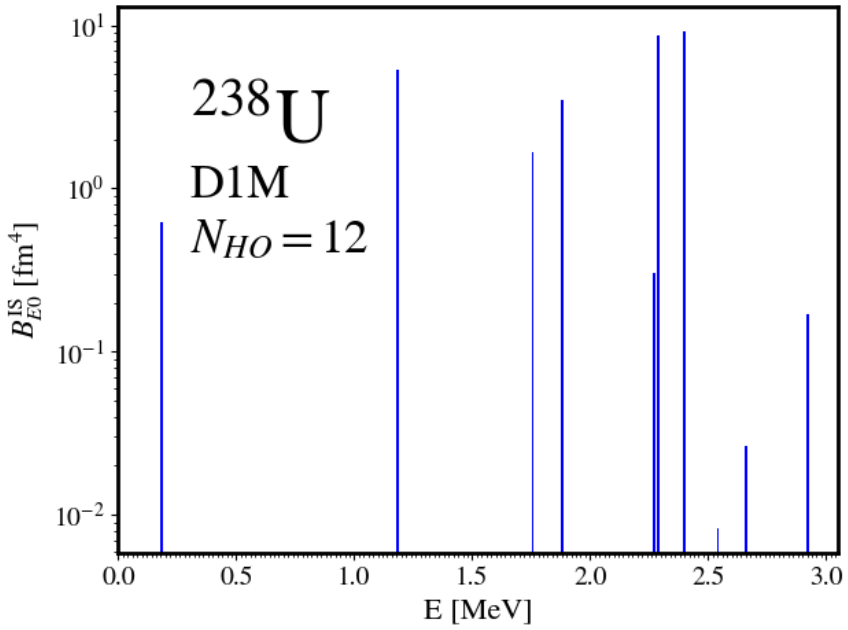

Figure 6.3: $E0$-QRPA response calculated JD method for ^{238}U using the Gogny D1M interaction and 12 main harmonic oscillator shells.

[2]The calculated spectrum is simmilar to that obtained with the D1S interaction [129]. As reviewed in [60], the results for heavy nuclei for D1S and D1M are qualitatively similar, which validates our spectrum extraction. A more precise one-to-one comparison between the results obtained with the different codes is underway.

6.5 Conclusion

In this chapter, we have proposed and tested the Exact-Jacobi-Davidson method for the resolution of the QRPA eigenproblem. The following points have been made:

- A version of the Jacobi-Davidson algorithm for QRPA-like matrices has been developed that exploits FAM to evaluate the matrix-vector product of the QRPA matrix and its inverse. The algorithm has been implemented in the `PAN@CEA` code.
- The algorithm has shown satisfactory performance when tested against FAM and matrix-QRPA implementations. A result of around 2 FAM calls per eigenvalue is obtained for the test cases that we have considered. This includes a realistic calculation in ^{238}U.
- The main numerical instabilities found in the algorithm may be related to the fact that zero QRPA spurious solutions may affect the convergence procedure. Also, for higher energy values, the number of FAM iterations needed in each global iteration increases dramatically. The first issue has been already covered in the literature and several solutions have been proposed. The second can be overcome with a small complex shift in the sampling energies.

The possibilities of applications of the JD algorithm are very varied, as they include the evaluation of nuclear spectroscopy at a very reduced computational price. This opens the way to the spectroscopy of all kinds of symmetry-breaking QRPA. Possible routes of improvement of the algorithm include the aforementioned removal of the spurious eigensolutions. Also, the extension of the algorithm to the simultaneous evaluation of several eigenvalues is being envisioned. Finally, this method can be used to calculate the contribution of the lowest-lying QRPA states to the ground-station correlation energy, which will be the topic of chapter 7.

Chapter 7

A Pauli correction to the QRPA ground state wave-function

During this thesis, QRPA has been used to investigate the spectroscopic properties of atomic nuclei. However, no attention has been put to how QRPA changes the ground state wave function with respect to HFB. The fact that QRPA excitations are written as linear combinations of two-quasiparticle excitations *and deexcitations* implies that the ground-state wave function is no longer just an HFB state. Within the quasiboson-approximation (QBA), an explicit expression for such wave-function can be written[130]. However, using the QBA breaks the Pauli principle, as we are neglecting the fermionic nature of the QRPA excitation operators. This induces a double-couting which overestimates correlations in the ground state. Several methods have been proposed in the literature to compensate for this in the case of ground-state observables. In reference [131], the RPA correlation energy is proposed to be divided by 2, whereas in [72] half of the first-order HF-perturbation energy is subtracted from it. In [73], a correction to the ground-state itself is derived, which results in the ground-state single-particle occupations being reduced by one-half. Additionally there exist other works also covering particle-particle RPA [132, 133]. Unfortunately, these correction methods are limited in the literature to RPA (no Q) with J preserving bosonic excitations. Nevertheless, the QRPA ground state has been used in the context of double-beta decay [134] and to calculate correlation energies [105]. Thus, obtaining a similar correction could be useful.

The goal of this chapter is to use the expresion of the ground-sate wave function given by QRPA to calculate observables. One clear example would be the calculation of nuclear masses: QRPA provides an extra correlation energy to be added on top of the HFB energy. For that, in this chapter, a Pauli correction to the QRPA ground-state wave function is derived. To do so, we generalize the work [73] to the QRPA case. The resulting correction results in dividing the standard QRPA correlation energy by three. This result is consistent with the Bogolyubov Many-Body Perturbation Theory (BMBPT) at first order [63]. As a preliminary test of how working with QRPA correlation energies would look like, its behavior is studied for some selected cases. In both RPA and QRPA, the correlation energy with Gogny D1M EDF is evaluated, which shows that QRPA correlation energies diverge unless a cutoff in phonon energy is set. The evaluation of different cutoff procedures that will give us concrete predictions will be the focus of a future work.

7.1 The QBA (Q)RPA ground state wave function

In QRPA and RPA (dubbed (Q)RPA when considered simultaneously) we model n-th collective excited state as linear combinations of the elementary excitations of the underlying mean-field

$$|n\rangle = Q_n^\dagger \,|\textbf{(Q)RPA}\rangle\,, \quad Q_\nu^\dagger = \sum_\alpha X_\alpha^n A_\alpha^\dagger - Y_\alpha^n A_\alpha \tag{7.1}$$

where $|\textbf{(Q)RPA}\rangle$ refers the (Q)RPA ground-state wave function. The elementary excitation operator $A_\alpha^\dagger$ is defined as

$$A_\alpha^\dagger = \begin{cases} a_p^\dagger a_h & \alpha = ph \text{ in RPA,} \\ \beta_i^\dagger \beta_j^\dagger & \alpha = ij, \quad i > j \text{ in QRPA.} \end{cases} \tag{7.2}$$

With RPA and QRPA built on top of the HF and HFB ground states respectively, which fulfill

$$a_p \,|\textbf{HF}\rangle = a_h^\dagger \,|\textbf{HF}\rangle = 0, \forall p, h \tag{7.3a}$$

$$\beta_i \,|\textbf{HFB}\rangle = 0, \forall i \tag{7.3b}$$

The commutator of the elementary excitation operator 7.2 can be written as

$$\left[A_\alpha, A_\beta^\dagger\right] = \delta_{\alpha\beta} + \Delta_{\alpha\beta}, \tag{7.4}$$

with the second term fulfilling

$$\Delta_{\alpha\beta}\,|\textbf{HF(B)}\rangle = 0, \quad \langle\textbf{HF(B)}|\,\Delta_{\alpha\beta} = 0, \quad \forall\alpha,\beta. \tag{7.5}$$

One of the main approximations of (Q)RPA is the so-called *quasiboson approximation*, in which we neglect the contribution to expectation values arising from the $\Delta_{\alpha\beta}$ term in equation 7.4. If we approximate $\Delta_{\alpha\beta} \approx 0$, then the elementary excitation operator obeys bosonic commutation rules. Thus, the HF(B) state(equation 7.3) becomes a boson vacuum, as it is annihilated by A_α. This allows us to interpret the (Q)RPA operators (7.1) as a Bogolyubov transformation of Bosons [4]. Assuming $\langle\textbf{(Q)RPA}|\textbf{HF(B)}\rangle \neq 0$, we can then apply the Thouless theorem for bosons, so the (Q)RPA wave function can be expressed as [130]

$$|\textbf{(Q)RPA}\rangle = N_0\, e^S\, |\textbf{HF(B)}\rangle\,. \tag{7.6}$$

with S the correlation operator,

$$S = -\frac{1}{2}\sum_{\alpha\beta} C_{\alpha\beta} A_\alpha^\dagger A_\beta^\dagger, \tag{7.7}$$

and $C_{\alpha\beta}$ being the *correlation matrix*, which needs to be symmetric. As the (Q)RPA ground state wave function is defined by the condition

$$Q_n \,|\textbf{(Q)RPA}\rangle \equiv 0, \forall n, \tag{7.8}$$

then we can find an explicit expression for the correlation matrix by applying the Baker-Campbell-Hausdorff formula, which reads

$$e^{-Z} W e^Z = W + [W, Z] + \frac{1}{2!}[[W, Z], Z] + ... \tag{7.9}$$

for any operators W, Z. Applying this in equation (7.6), then

$$Q_n \,|\textbf{(Q)RPA}\rangle = N_0 e^S \sum_\alpha \left(Y_\alpha^{n*} - \sum_\beta C_{\alpha\beta} X_\beta^{n*} \right) A_\alpha^\dagger \,|\textbf{HF(B)}\rangle = 0. \tag{7.10}$$

which can only be fulfilled if

$$Y_{\alpha}^{\nu *} - \sum_{\beta} C_{\alpha\beta} X_{\beta}^{\nu *} = 0, \tag{7.11}$$

which in matrix form can be written as

$$\mathbf{Y} = \mathbf{C}^{*}\mathbf{X}. \tag{7.12}$$

This equation can be solved in several ways The most straightforward is by calculating the matrix $\mathbf{X}^{-1}$, which can be analytically derived (see appendix C for details). However, we can also derive a self-consistent expression for $\mathbf{C}$. To do so we define $\overline{\mathbf{A}} = \mathbf{A} - \varepsilon$, with $\mathbf{A}$ one of the subcomponents of the (Q)RPA matrix and ε the diagonal matrix containing the energy of the elementary excitations i.e.

$$\varepsilon_{\alpha} = \begin{cases} E_p - E_h, & \text{in RPA,} \\ E_i + E_j, & \text{in QRPA.} \end{cases} \tag{7.13}$$

Substituting (7.12) in the (Q)RPA equation(1.66), multiplying the first row by $\mathbf{C}^{*}$ on the left and then adding both lines results in

$$C_{\alpha\beta}^{\mathrm{QBA}} = -\frac{1}{\varepsilon_{\alpha} + \varepsilon_{\beta}} \left(\mathbf{B} + \overline{\mathbf{A}}\mathbf{C}^{\mathrm{QBA}} + \mathbf{C}^{\mathrm{QBA}}\overline{\mathbf{A}}^{*} + \mathbf{C}^{\mathrm{QBA}}\mathbf{B}^{*}\mathbf{C}^{\mathrm{QBA}} \right)_{\alpha\beta}. \tag{7.14}$$

which allows us to express the correlation matrix $C_{\alpha\beta}$ exclusively in terms of the (Q)RPA $\mathbf{A}$ and $\mathbf{B}$ matrices and the elementary excitations energies.

7.2 Corrections to the ground state correlations

The problem with the expression of the (Q)RPA ground state is that it is well known to overestimate ground state correlations. One of the possible culprits for this is that the QBA was considered in the derivation of $\mathbf{C}$. To partially restore the Pauli principle, we follow the procedure outlined by [73] and extrapolate it to the QRPA case. This protocol can be summarized as follows:

- The QRPA wave function (7.6) retains the same exponential form while still fulfilling the condition $Q_{\nu} \left| \mathbf{(Q)RPA} \right\rangle = 0$ at first order in $\mathbf{C}$.
- The contribution arising from the Δ_{ij} factor in (7.4) is not neglected when evaluating the commutators in equation 7.9.

By doing this the fermionic structure becomes relevant, so the QRPA and RPA cases need to be considered separately. In both cases, the terms arising in each of the commutators increase significantly, making their evaluation rather cumbersome. These commutators are evaluated here using the second quantization module of the `SymPy` symbolic calculation library [135].

7.2.1 Correction to the QRPA ground state

When written in terms of single-quasiparticle operators, the correlation operator takes the form

$$S = -\frac{1}{2^3} \sum_{ijkl} C_{ijkl} \beta_i^{\dagger} \beta_j^{\dagger} \beta_k^{\dagger} \beta_l^{\dagger}, \tag{7.15}$$

where now the correlation matrix becomes the C_{ijkl} tensor, which is fully antisymmetric under any permutation of the quasiparticle indices. This new ground state wave function shares the functional

form of a coupled-cluster state with doubles [136]. This connection was already explored for the RPA case in reference [137]. We can now introduce this equation in the exponential series, which gives

$$N_0 e^S \left[\frac{1}{2} \sum_{ij} \left(Y^\nu_{ij} - \frac{3}{2} \sum_{kl} C_{ijkl} X^{\nu\,*}_{kl} \right) \beta^\dagger_i \beta^\dagger_j - \frac{1}{8} \sum_{ijklmn} \Xi^\nu_{ijklmn} \beta^\dagger_i \beta^\dagger_j \beta^\dagger_k \beta^\dagger_l \beta^\dagger_m \beta^\dagger_n \right] |\mathrm{HFB}\rangle = 0 \tag{7.16}$$

with the second term being

$$\Xi^\nu_{ijklmn} = \sum_{op} X^{\nu\,*}_{op} C_{oijk} C_{plmn} \tag{7.17}$$

and any other higher-order contributions vanishing. By restricting the summation to $k > l$ and considering that each term must vanish, one obtains

$$Y^\nu_{ij} - 3 \sum_{k>l} C_{ijkl} X^{\nu\,*}_{kl} = 0, \tag{7.18}$$

which allows a direct comparison to the QBA result

$$\mathbf{C}^{\mathrm{QBA}} = 3\mathbf{C}^{\mathrm{Exact}}_{\mathrm{QRPA}}. \tag{7.19}$$

Thus, the Pauli corrected correlation matrix is exactly the QBA result divided by 3.

7.2.2 Correction to the RPA ground state

The RPA case was studied in the case where single-particle orbitals have good angular momentum [73]. However, in the symmetry-less form, an equally simple correction can be found. The correlation operator now becomes

$$S = -\frac{1}{2} \sum_{php'h'} C_{php'h'} a^\dagger_p a_h a^\dagger_{p'} a_{h'} \tag{7.20}$$

with $C_{php'h'}$ antisymmetric under permutation of any of the indices, although we restrict the sum to the particle states for the p, p' indices and to the hole states for the h, h' indices. Following the same procedure, one gets

$$N_0 e^S \left[\sum_{ph} \left(Y^\nu_{ph} - 2 \sum_{p'h'} C_{php'h'} X^{\nu\,*}_{p'h'} \right) a^\dagger_p a_h + \frac{1}{2} \sum_{php'h'p''h''} \Xi_{php'h'p''h''} a^\dagger_p a_h a^\dagger_{p'} a_{h'} a^\dagger_{p''} a_{h''} \right] |\mathrm{HF}\rangle = 0 \tag{7.21}$$

which gives

$$\mathbf{C}^{\mathrm{QBA}} = 2\mathbf{C}^{\mathrm{Exact}}_{\mathrm{RPA}} \tag{7.22}$$

this time the correlation matrix is exactly twice the QBA result. If we substitute the RPA result in the self-consistent formula 7.14, then at first order in the inverse of the $2ph$ energies we obtain

$$\left(C^{\mathrm{Exact}}_{\mathrm{RPA}} \right)_{\alpha\beta} \approx -\frac{1}{2} \frac{B_{\alpha\beta}}{\varepsilon_\alpha + \varepsilon_\beta} \tag{7.23}$$

In reference [72], the proposed correction to the wave function is to remove the right-hand side term to the QBA results, which coincides with equation 7.22 at first order. In this reference, however, the QRPA phonons are coupled to good J. In appendix C we show that the one-half factor can also be derived for that case.

7.2.3 Agreement of both formulae at the zero-pairing limit

To check that both formulae are consistent with each other, one can start with the QRPA correlation operator (7.15). The zero pairing limit for the quasi-particle operators is

$$\beta_i^\dagger = \begin{cases} a_p^\dagger, & \text{for } i = p, \\ a_h, & \text{for } i = h. \end{cases} \tag{7.24}$$

By taking into consideration the fact that only $2p2h$ contributions are considered in the vacuum at the 0-pairing limit, we have 6 different combinations of the $ijkl$ indices that contribute to the sum in expression 7.15, namely $phph, phhp, hpph, hphp, pphh$ and $hhpp$. This results in

$$S = -\frac{3}{2^2} \sum_{php'h'} C_{php'h'} a_p^\dagger a_h a_{p'}^\dagger a_{h'} \tag{7.25}$$

Which gives us the relation

$$\mathbf{C}^{\text{Exact}}_{\text{QRPA 0-Pairng}} = \frac{2}{3} \mathbf{C}^{\text{Exact}}_{\text{RPA}} \tag{7.26}$$

which makes the expressions 7.22 and 7.19 consistent.

7.3 Correlation energies

The fact that the ground state is no longer an HFB state implies that additional contributions to the ground state energy may arise. However, as (Q)RPA is not a variational theory, the total energy associated to the QRPA state may be lower than the exact solution obtained by fully diagonalizing the Hamiltonian. The (Q)RPA correlation energy is defined as

$$E_{\text{cor}}^{\text{(Q)RPA}} = \langle \textbf{(Q)RPA} | \, H \, | \textbf{(Q)RPA} \rangle - E_{\text{HF(B)}}. \tag{7.27}$$

With the derived expressions for the correlation matrices, now the (Q)RPA correlation energy is evaluated.

7.3.1 Quasiboson (Q)RPA energy

Within the quasiboson approximation, the correlation energy is calculated by considering the approximate Hamiltonian that reproduces the (Q)RPA equations of motion [4]

$$H_{\text{QBA}} = E_{\text{HF(B)}} + \sum_{\alpha\beta} A_{\alpha\beta} A_\alpha^\dagger A_\beta + \frac{1}{2} \sum_{\alpha\beta} \left(B_{\alpha\beta} A_\alpha^\dagger A_\beta^\dagger + \text{h.c.} \right). \tag{7.28}$$

By expressing the Hamiltonian in the (Q)RPA phonon basis $Q_n^\dagger$, one obtains an expression for the correlation energies in terms of the $\mathbf{A}$ (Q)RPA matrix and the (Q)RPA eigensolutions

$$E_{\text{cor}}^{\text{(Q)RPA}-\text{QBA}} = \frac{1}{2} \operatorname{tr} (\mathbf{\Omega} - \mathbf{A}) = -\operatorname{tr} \mathbf{Y}^\dagger \mathbf{\Omega} \mathbf{Y} \tag{7.29}$$

with Ω the diagonal matrix with the (Q)RPA eigensolutions. By rewriting the (Q)RPA equation in a matrix form

$$\begin{pmatrix} \mathbf{A} & \mathbf{B} \\ -\mathbf{B}^* & -\mathbf{A}^* \end{pmatrix} \begin{pmatrix} \mathbf{X} \\ \mathbf{Y} \end{pmatrix} = \begin{pmatrix} \mathbf{X} \\ \mathbf{Y} \end{pmatrix} \mathbf{\Omega}, \tag{7.30}$$

multiplying on the right by $\mathbf{X}^{-1}$ and substituting equation 7.12, one obtains [137]

$$\begin{pmatrix} \mathbf{A} & \mathbf{B} \\ -\mathbf{B}^* & -\mathbf{A}^* \end{pmatrix} \begin{pmatrix} I \\ \mathbf{C}^* \end{pmatrix} = \begin{pmatrix} I \\ \mathbf{C}^* \end{pmatrix} \mathbf{X}\boldsymbol{\Omega}\mathbf{X}^{-1}. \tag{7.31}$$

By performing the matrix-vector product, the first line then reads

$$\mathbf{A} + \mathbf{B}\mathbf{C}^* = \mathbf{X}\boldsymbol{\Omega}\mathbf{X}^{-1} \tag{7.32}$$

Then one obtains the following value for the correlation energy

$$E_{\text{cor}}^{\text{(Q)RPA-QBA}} = \frac{1}{2} \operatorname{tr} \mathbf{B}\mathbf{C}^* \tag{7.33}$$

This expression has been used as a comparatively cheap alternative to the full diagonalization of H in shell model calculations [138]. However, as we mentioned before, taking into account Pauli correction, its value is significantly impacted [72, 131]. We discuss this in the following section.

7.3.2 Pauli corrected QRPA energy

To evaluate the QRPA correlation energy in taking into account Pauli effects, we need to evaluate the expectation value of the Hamiltonian. To do so, we use the quasiparticle basis expression for H that was derived in chapter 1

$$H = E_{\text{HFB}} + H^{11} + H^{22} + H^{40} + H^{04} + H^{31} + H^{13} \tag{7.34}$$

The H^{31} and H^{13} components do not contribute to the expectation value, as they break quasiparticle-number parity, which is a good quantum number in $|\mathbf{QRPA}\rangle$. To evaluate $\langle \mathbf{QRPA}| H |\mathbf{QRPA}\rangle$, one can use equation 7.9 and keep only linear terms of C, obtaining

$$\langle \mathbf{QRPA}| H |\mathbf{QRPA}\rangle = \langle \mathbf{QRPA}| e^S \left(H + [H, S]\right) |\mathbf{QRPA}\rangle + o(C^2) \tag{7.35}$$

where we neglect any higher orders, as $\mathbf{C}$ is supposed to be small. Using the definitions of the $\mathbf{A}, \mathbf{B}$ matrices in the q.p. basis [4]

$$\overline{A}_{ijkl} = H^{22}_{ijkl}, \quad B_{ijkl} = 4! H^{40}_{ijkl}, \quad \text{for } i > j, k > l, \tag{7.36}$$

then one evaluates term by term the expected value 7.35, obtaining

$$\left(H^{11} + \left[H^{11}, S\right]\right) |\text{HFB}\rangle = -\frac{1}{2} \sum_{ijkl} \varepsilon_i C_{ijkl} \beta_i^\dagger \beta_j^\dagger \beta_k^\dagger \beta_l^\dagger \tag{7.37a}$$

$$\left(H^{22} + \left[H^{22}, S\right]\right) |\text{HFB}\rangle = -\frac{3}{8} \sum_{ijklop} \overline{A}_{ijop} C_{opkl} \beta_i^\dagger \beta_j^\dagger \beta_k^\dagger \beta_l^\dagger \tag{7.37b}$$

$$\left(H^{40} + \left[H^{40}, S\right]\right) |\text{HFB}\rangle = +\frac{1}{4!} \sum_{ijkl} B_{ijkl} \beta_i^\dagger \beta_j^\dagger \beta_k^\dagger \beta_l^\dagger \tag{7.37c}$$

$$\left(H^{04} + \left[H^{04}, S\right]\right) |\text{HFB}\rangle = -\frac{1}{8} \sum_{ijkl} B^*_{ijkl} C_{ijkl} \tag{7.37d}$$

To be able to remove the single-particle energy term, one can use equation 7.14, which for the QRPA Pauli corrected case becomes

$$C^*_{\alpha\beta} = -\frac{1}{\varepsilon_\alpha + \varepsilon_\beta} \left(\frac{1}{3} \mathbf{B}^* + \overline{\mathbf{A}}\mathbf{C} + \mathbf{C}\overline{\mathbf{A}}^* + 3\mathbf{C}\mathbf{B}\mathbf{C} \right)_{\alpha\beta}. \tag{7.38}$$

By developing the subindices, this can be written as

$$(\varepsilon_i + \varepsilon_j + \varepsilon_k + \varepsilon_l)C^*_{ijkl} = -\frac{1}{3}B^*_{ijkl} - \sum_{op}\overline{A}^*_{ijop}C^*_{opkl} - \frac{3}{4}\sum_{opqr}C^*_{ikop}B_{opqr}C^*_{qrjk} \tag{7.39}$$

where $\overline{A}_{ijkl} = \overline{A}^*_{klij}$ was used. This expression can be compared with the commutator of H^{11} in 7.37 by using the identity

$$\sum_{ijkl}\varepsilon_i C_{ijkl}\beta^\dagger_i\beta^\dagger_j\beta^\dagger_k\beta^\dagger_l = \frac{1}{4}\sum_{ijkl}\left(\varepsilon_i + \varepsilon_j + \varepsilon_k + \varepsilon_l\right)C_{ijkl}\beta^\dagger_i\beta^\dagger_j\beta^\dagger_k\beta^\dagger_l \tag{7.40}$$

Summing all the components in 7.37 and taking into account that S commutes with all terms gives

$$\begin{aligned}\langle \mathrm{QRPA}|\, H\, |\mathrm{QRPA}\rangle =& E_{\mathrm{HFB}} - \frac{1}{8}\sum_{ijkl}B^*_{ijkl}C_{ijkl} \\ &+ \sum_{ijkl}\left[\frac{1}{12}B_{ijkl} - \frac{1}{4}\sum_{op}\overline{A}_{ijop}C_{opkl}\right]\langle \mathrm{QRPA}|\beta^\dagger_i\beta^\dagger_j\beta^\dagger_k\beta^\dagger_l\,|\mathrm{QRPA}\rangle + o(C^3)\end{aligned} \tag{7.41}$$

To evaluate the expectation value of the four-quasiparticle operators, we can use a complete set of QRPA states, which results in

$$\sum_n \langle \mathrm{QRPA}|\beta^\dagger_i\beta^\dagger_j|n\rangle\langle n|\beta^\dagger_k\beta^\dagger_l\,|\mathrm{QRPA}\rangle \approx \sum_n Y^n_{ij}X^{n\,*}_{kl}. \tag{7.42}$$

Using 7.18, then

$$\frac{1}{8}\sum_{ijkl}B_{ijkl}\langle \mathrm{QRPA}|\beta^\dagger_i\beta^\dagger_j\beta^\dagger_k\beta^\dagger_l\,|\mathrm{QRPA}\rangle = \frac{1}{8}\sum_n\sum_{ijklop}C^*_{ijop}X^n_{op}B_{ijkl}X^{n\,*}_{kl} + o(C^2) \tag{7.43a}$$

$$-\frac{1}{4}\sum_{ijkl}\sum_{op}\overline{A}_{ijop}C_{opkl}\langle \mathrm{QRPA}|\beta^\dagger_i\beta^\dagger_j\beta^\dagger_k\beta^\dagger_l\,|\mathrm{QRPA}\rangle = -\frac{1}{2}\sum_n\sum_{ijkl}Y^n_{ij}\overline{A}_{ijkl}Y^{n\,*}_{kl} + o(C^2) \tag{7.43b}$$

We can now sum both equations in 7.43, and use the closure relation of QRPA eigenstates, which gives

$$\frac{1}{4}\sum_{ijkl}C^*_{ijkl}B_{ijkl} + \frac{1}{2}\sum_{ijklop}C^*_{ijop}Y^n_{op}B_{ijkl}Y^{n\,*}_{kl} - \sum_n\sum_{ijkl}Y^n_{ij}\overline{A}_{ijkl}Y^n_{kl} \tag{7.44}$$

The last two terms come multiplying with the Y amplitudes to the right and left, which is of the order of $o(C^2)$ (see appendix C), so they can be neglected. Thus, summing all terms in 7.37 amounts to

$$\boxed{E^{\mathrm{QRPA-Exact}}_{\mathrm{cor}} \approx \frac{1}{2}\,\mathrm{Tr}\,\mathbf{B}\left(\mathbf{C}^{\mathrm{Exact}}_{\mathrm{QRPA}}\right)^* = \frac{1}{3}E^{\mathrm{QRPA-QBA}}_{\mathrm{cor}}.} \tag{7.45}$$

This means that correlation energies get divided by three with respect to the QRPA case with our Pauli correction. If now use equation 7.38 to substitute the correlation matrix up to first order, this gives

$$E^{\mathrm{QRPA-Exact}^{(1)}}_{\mathrm{cor}} = -\frac{1}{6}\sum_{\alpha\beta}\frac{\left|B_{\alpha\beta}\right|^2}{\varepsilon_\alpha + \varepsilon_\beta}. \tag{7.46}$$

which is exactly the first-order term of the Bogolyubov many-body perturbation theory expansion [105].

7.3.3 Correlation energy at the RPA limit

To now go to the RPA case, we just need to apply the zero-pairing limit formula for the correlation matrix (equation 7.26). Substituting it in equation 7.45, one obtains

$$E_{\text{cor}}^{\text{RPA-exact}} = \frac{1}{2} E_{\text{QBA}}^{\text{cor}} \tag{7.47}$$

which is the usual one-half correction formula [131, 137].

7.4 Convergence of the RPA correlation energies

To test the behavior of the formulae here derived, matrix-RPA (no pairing) calculations were performed using the Gogny D1M pseudopotential [12]. This effective interaction was derived with the intended purpose of fitting nuclear masses at a beyond-static-mean-field level using a five-dimensional collective Hamiltonian(5DCH). However, for closed-shell nuclei, the correlation energy obtained with the 5DCH made them less bound, so this contribution was not considered. In any case, HFB with D1M already predicts the binding energy of magic nuclei up to 1 MeV [92]. As we will see, the RPA correction energies are rather big, so the results here shown are to be interpreted in terms of their global tendency and not their exact numerical value. The calculations were done without calculating the two-body center of mass correction nor the exchange coulomb contribution for practical reasons.

In order to be able to study the contribution of each of the RPA phonons to the correlation energy, the correlation energy with the QBA formula with a cutoff in the phonon-energy Λ as

$$E_{\text{Cor}}^{\text{QBA}}(\Lambda) = -\sum_{ph} \sum_{\substack{n \\ \omega_n < \Lambda}} \omega_n \left| Y_{ph}^n \right|^2 \tag{7.48}$$

The results of the ratio between the RPA correlation energy and the HF energy are shown in figure

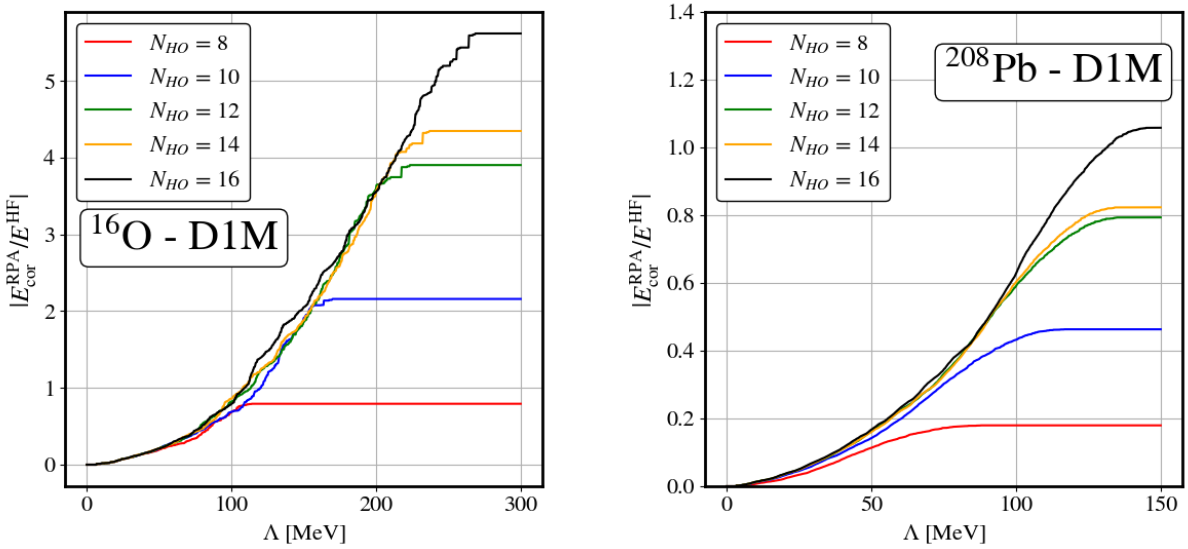

Figure 7.1: Ration between the absolute value of the RPA correlation energy and the HF energy as a function of the cutoff on phonon energies using the D1M interaction. Results using a different number of Harmonic oscillator shells are shown

7.1 for ^{16}O and ^{208}Pb for different values of the number of harmonic oscillator shells used. Right from the start, a pretty surprising result is found: RPA correlation energies are very big, in the case of oxygen up to more than five times the HF energy. On top of that, the result does not seem to converge with an increasing number of harmonic oscillator shells. However, these two facts are consistent with other results from the literature. In [63], a momentum transfer was set on the matrix elements of the Skyrme interaction used to obtain a converged result. On the other hand, in reference [138], the RPA calculations were performed in a small valence space; here we see that increasing the model space greatly increases the energy. Thus, for any application using EDF, a cutoff in phonon energy will need to be set. It has often been argued that only the lower energy phonons should be considered in the correlation energy [131]. The correlation energies obtained up to $\Lambda = 50$ MeV are converged up to a 1% ratio $E_{\text{cor}}^{\text{QBA}}/E_{\text{HF}}$, which further justifies the use of cutoffs when considering the correlation energy. Furthermore, as shown in the previous chapter, obtaining a reduced subset of the QRPA spectrum can be done cheaply via, for example, the JD-QRPA method developed in this thesis, which opens the way for the systematic evaluation of QRPA correlation energies.

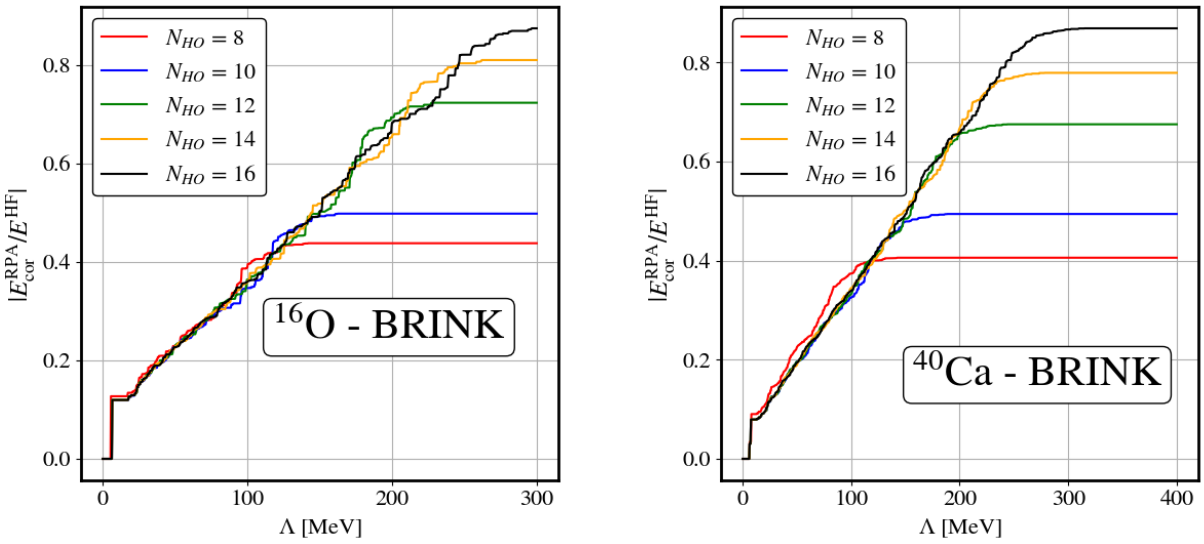

Figure 7.2: Ration between the absolute value of the RPA correlation energy and the HF energy as a function of the cutoff on phonon energies using the Brink and Boeker interaction. Results using a different number of Harmonic oscillator shells are shown

The D1M interaction includes two contact terms: the spin-orbit and the density term. Contact terms are known to induce ultraviolet divergencies when going beyond static-mean-field. To see if the divergence at high energy is an example of this, we repeat the calculations using the Brink and Boeker interaction [139]. This interaction has the functional form of a D1-type Gogny interaction in the direct term, while not having neither spin-orbit nor density terms. This makes it a fully finite range interaction, so it would not be expected to show ultraviolet divergencies. We show the results with this interaction in figure 7.2 for ^{16}O and ^{40}Ca. Convergence for the high energy part is not achieved at 16 harmonic oscillator shells, which points to this phenomenon being intrinsically linked to RPA. On top of that, the fact that even with cutoffs the correlation energies obtained through this method are larger than the ones considered in the D1M mass formula five-dimensional collective Hamiltonian (5DCH) [76] can be surprising but can be explained. The 5DCH takes into account only quadrupole degrees of freedom, while RPA takes all multipolarities into account.

Figure 7.3 shows the contribution to the correlation energy of each J^π block. As it can be seen the quadrupole (2^+) is just a fraction of the total correlation energy.

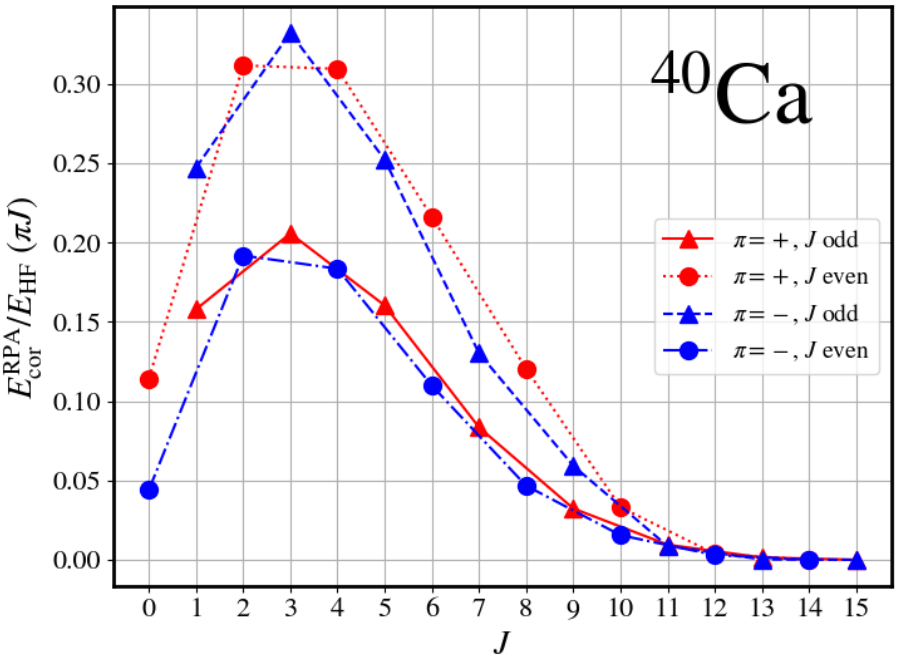

Figure 7.3: Contributions to the RPA correlation energy of each J^π block in ^{40}Ca using the D1M interactions with $N_{HO} = 12$ as a fraction with respect to the HF energy. No phonon cutoff was imposed.

7.5 Effect of the RPA and QRPA corrections

Having established that one should not take the full QRPA spectrum into account to obtain realistic RPA correlation energies, we now check the results using the correction formulae. Starting with the pairing-less case, RPA calculations were performed for doubly-closed nuclei. The result for the correlation energies obtained is plotted in figure 7.4 with and without the one-half Pauli correction. It can be observed that there is no immediate way to establish a natural cutoff for the correlation energies, as they grow indefinitely for all cases. One can see that for all nuclei considered the correlation energy grows similarly with the cutoff. For the interval between 25 and 40 MeV, the corrected correlation energy stays between at a fraction of $2-8\%$, which is more in line with what is expected for a correlation energy on top of a regular EDF.

As a way to test the behavior of the simple correction for the QPRA correlation energy derived here, the QRPA and RPA correlation energies for ^{16}O with 8 harmonic oscillator shells. Figure 7.5 shows the values obtained including or not the QRPA solution. One can see how the corrected QPRA and RPA energy between 25 and 40 MeV differ in less than 5%. It could be interesting to check whether this energy regime is the one where both corrections coincide for other nuclei. If that is the case, this could be a lead to a possible cutoff in the correlation energies. In anyways, when taking the full spectrum, the total correlation energy stays at E_{cor}(QRPA) = 169.0 and 56.6 MeV with and without correction respectively for QPRA and E_{cor}(RPA) = 148.0 and 74.0 MeV for RPA, so corrections do not necessarily coincide at all energy regimes. It has to be taken into

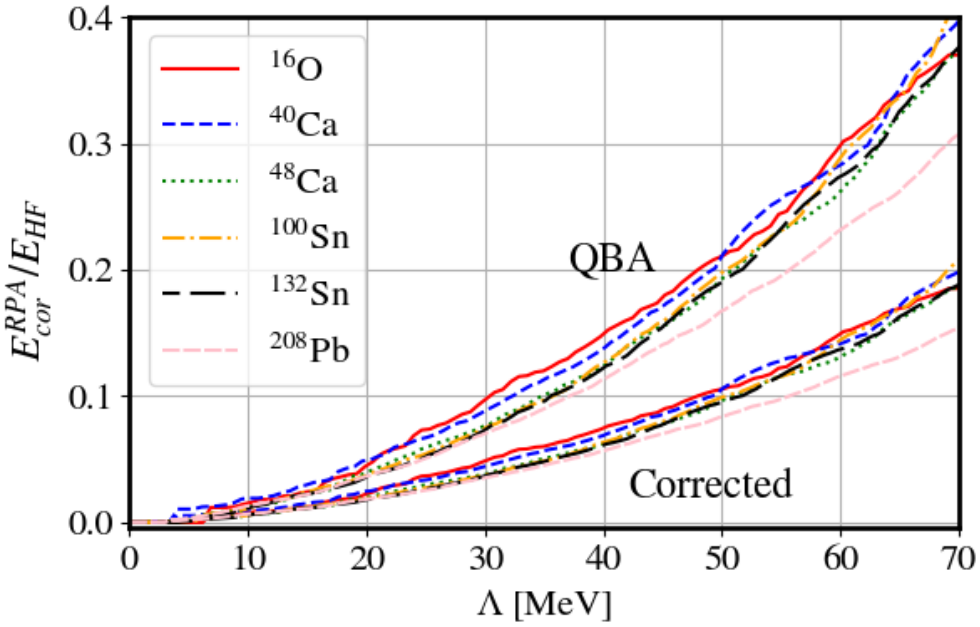

Figure 7.4: RPA correlation energy as a fraction of the HF energy as a function of the energy cutoff for the RPA phonons. The QBA and corrected (divided by one-half) results are shown. The RPA calculations were done with 16 main harmonic oscillator shells.

account that in the derivation of these formulae we have neglected many terms on the grounds that they scale as $o(C^2)$. It remains to be seen whether their contribution is significant.

7.6 Conclusions

In this chapter, a simple Pauli correction for the QRPA correlation matrix and correlation energy has been derived, which in both cases consists of dividing the QBA results by three. It has been shown that correlation energies in general diverge for increasing value of the energy cutoff considered for the contributing QRPA bosons using the D1M Gogny interaction. When comparing the results between RPA and QRPA corrected correlation energies, it is observed that a cutoff between 20 and 40 MeV gives correlation energies of the order of 3-8 % for the considered nuclei and makes the QRPA and RPA corrected energy coincide in ^{16}O.

It should be taken into consideration that no treatment of the spurious states has been performed other than removing them from the sum of equation 7.48. One could envision a more detailed treatment, as the one done in reference [138]. Once a correct cutoff procedure has been established, it could be possible to try to fit an interaction that reproduces binding energies at the QRPA level. The 5DCH used in the fitting of D1M only includes contributions coming from quadrupole degrees of freedom [76], whereas quadrupole excitations only contribute to a fraction of the RPA energy. The fact that all contributions are considered can constitute a significant improvement. In the future, only the lowest-lying eigenvalues will be considered for a systematic evaluation of the correlation energies. A fast evaluation of the correlation energy coming from these eigenstates could be evaluated using, for example, the JD-QRPA method developed during this thesis. Finally, it would be interesting to test the results obtained with chiral QRPA. As was discussed in chapter 4, chiral interactions produce a much smaller HFB binding energy than EDFs, so the big ratios that were observed for the correlation energy could be better justified in that context.

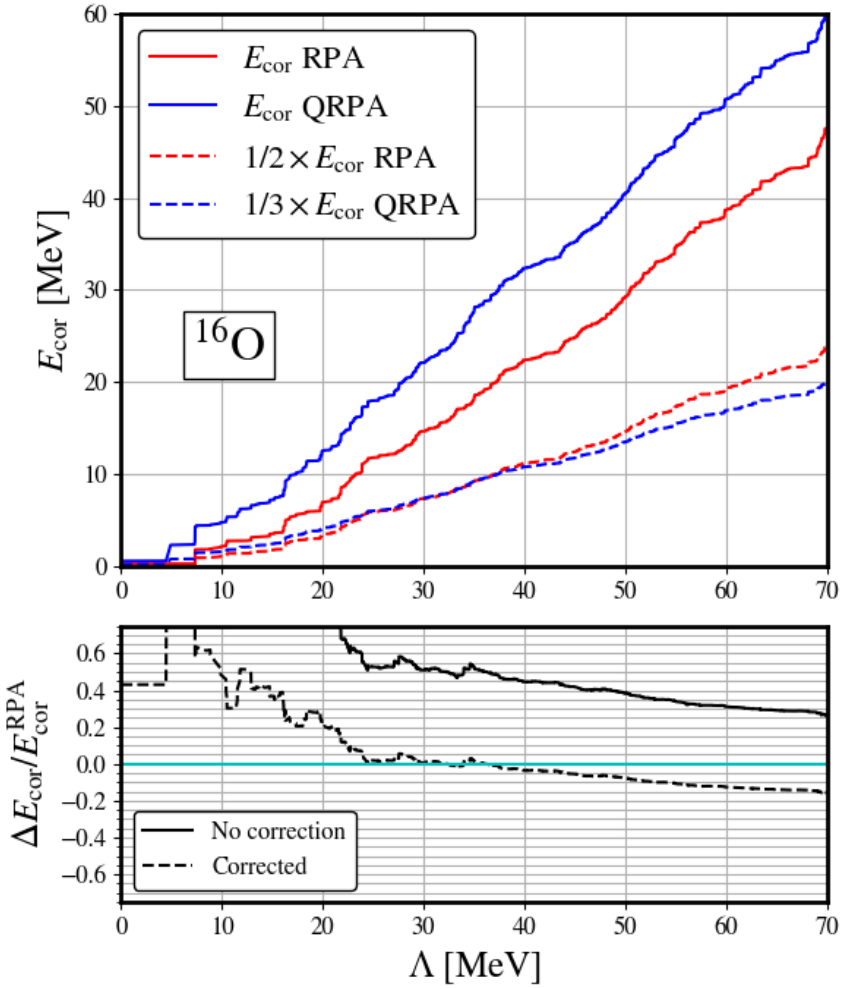

Figure 7.5: Top: QRPA and RPA correlation energies calculated with and without the respective correction. Bottom: Value of the relative difference between QRPA and RPA correlation energies $(E_{cor}(\text{QRPA}) - E_{cor}(\text{RPA}))\,/E_{cor}(\text{RPA})$ for the corrected and uncorrected cases.

Conclusion(s)

> Arrakis teaches the attitude of the knife - chopping off what's incomplete and saying: 'Now, it's complete because it's ended here.'
>
> Frank Herbert, *Dune*

The development of the FAM algorithm in the last decade has led to a "democratization" of QRPA: With calculation times significantly reduced, teams with less computational resources can afford now the evaluation of γ-strength functions; those lucky to enjoy access to state of the art computing facilities, as the CEA-DAM team where this thesis took place, can benefit of a multiplicative factor in terms of performance: Studies that used to take up to a year in human time now can be done in weeks. The contributions of this thesis go both in the *production* of QRPA results and in the *development* of new techniques that aim at a more efficient evaluation of the QRPA problem, as well as accessing new kinds of information about the theory.

On the one hand, this thesis includes the second-ever global QRPA study using an explicitly deformed mean field, and the first-ever using a deformed relativistic QRPA, in this case with the DD-PC1 Lagrangian. Some global behaviors of QRPA-E1 strengths have been observed that had not been described before. This includes the push to higher energies and the narrowing of the strength functions with shell closures. Also, some of the previously used empirical rules to obtain artificially deformed strengths have been tested, with some of the rules not being completely followed for higher deformations. A more detailed analysis comparing the obtained strengths with previous QRPA studies is currently being performed. Additionally, the results here presented will be used on the the ongoing PANDORA project [100] for the evaluation of strength functions up to $Z = 60$. As a clear perspective, the nuclear chart-wide study could be extended to other transitions, with $E2$ and $M1$ being the most likely candidates, as they usually constitute the second most important contribution to the photoabsorption strength. Lastly, one of the goals of this work would be to incorporate the obtained strength into the widely used TALYS code [83].

Alongside the nuclear-chart-wide study with covariant EDF, the first chiral QRPA systematic study covering nuclei with GDR data up to iron has been performed. It is shown that chiral interactions can provide results comparable to those of EDF in terms of agreement with experimental data. The convergence of QRPA with the chiral expansion of the Hamiltonian from reference [29] is observed for this mass region. Around iron, a growing contribution at high energy gradually appears with increasing mass that is not observed in experimental data. It remains to be seen whether this is a limitation of the chiral interactions (not high enough expansion in the chiral expansion) of QRPA, but in this study, we show that it is a shared characteristic between EM1.8/2.0 and the interaction from reference [29]. Another analysis that could be done with the two sets of strengths obtained is to study the effect of neutron skins in the dipole polarizability [110, 111], which can be calculated via the m^{-1} moment of the strength.

In this work, we have also performed the first-ever study of chiral QRPA strengths with a triaxially deformed mean field. Both ^{24}Mg and ^{32}S are shown to display a clearly triaxial minimum when using the interaction from reference [29]. On top of that, the HFB minimum in ^{24}Mg displays 6-α structure. While the triaxial minimum in ^{32}S does not show clustering, a secondary minimum is observed in the PES that corresponds to a $2\times^{16}$O cluster configuration. The strength function for both nuclei is better reproduced with the triaxial shape, with the QRPA strength being three-peaked in the region of experimental data. This evaluation of the triaxial QRPA strength at reasonable computational times is made possible thanks to the increased computational efficiency of the FAM approach. This opens the way to the improvement of the description of the QRPA strengths alongside the nuclear chart.

On top of the systematic calculations performed, part of the achievements of the thesis is the development of the Jacobi-Davidson method for the fast evaluation of several QRPA eigenvectors. In our implementation, we show that QRPA eigenvectors are reproduced up to numerical precision with this method. JD has the advantage that one does not need to know the position of the eigenvalue from before to extract it. The method is especially performing at small energies, where only 2 to 5 calls to FAM are needed to find an eigenvalue. Some numerical issues still to be solved are the augmented number of FAM iterations needed in each global JD iteration for bigger model spaces and higher sampled energies. Several possible remedies are now being implemented. In any way, the feasibility and performance of the method have been tested, which opens the way to cheap calculation of nuclear spectra for both EDF and chiral interactions. This will allow us to gain fast access to low-lying collective states and their contribution to the correlation energy.

Finally, a new simple prescription has been derived for a correction for the QRPA ground-state wave function. The protocol from reference [73] for RPA has been extended to the QRPA case. Correlation QRPA energies have been calculated with the D1M Gogny interaction. It has been observed that, unless a phonon-energy cutoff is used, correlation energies diverge, accounting for several times the HFB energy. When setting a cutoff between 25 and 40 MeV, correlation energies stay at around 2 to 8 % of the HFB energy, which is more in line with what is expected from an EDF. This energy range coincides with that for which the corrected RPA and QRPA energies coincide, which may point to at possible value for a phonon-energy cutoff. Once a sensitive cutoff is set, this could open the way for fitting an interaction to be able to reproduce masses at the QRPA level. This would allow us to describe ground state and spectroscopic properties on the same footing.

Appendices

Appendix A

Proofs regarding QRPA-FAM

Given an operator F, its associated transition rate can be defined as

$$B(E_i \to \mathrm{GS}) = |\langle i| F |\mathrm{GS}\rangle|^2 \tag{A.1}$$

The transition strength then can be defined as the derivative with respect the energy of the excited state of this quantity

$$S(E;F) \equiv \frac{dB}{dE}(E;F) = \sum_i |\langle i| F |\mathrm{GS}\rangle|^2 \delta(E_i - E) \tag{A.2}$$

With $|i\rangle$ all the excited estates. Then it is trivial to see that

$$\int_{E_0}^{E_0+\Delta E} S(E;F) = \sum_{E_i \in (E_0, E_0+\Delta E)} |\langle i| F |\mathrm{GS}\rangle|^2 \tag{A.3}$$

A.1 (Q)RPA strength functions

The solution to the (Q)RPA equations give a set of excited states $\{|n\rangle\}$ which can be separated into positive-energy physical and negative-energy unphysical solutions. As such, the strength function is defined as

$$S(E;F) \equiv \sum_{n>0} |\langle n| F |(\mathrm{Q})\mathrm{RPA}\rangle|^2 \delta(E_n - E) \tag{A.4}$$

where $n > 0$ stands for positive energy states. Let's now take the quantity

$$I(\omega, \gamma; F) = \sum_n \frac{|\langle n| F |(\mathrm{Q})\mathrm{RPA}\rangle|^2}{\omega - E_n + i\gamma} - \frac{\left|\langle n| F^\dagger |(\mathrm{Q})\mathrm{RPA}\rangle\right|^2}{\omega + E_n - i\gamma} \tag{A.5}$$

Assuming F is Hermitian, then we can write

$$I(\omega, \gamma; F) = \sum_n f(E_n; F) \left(\frac{1}{\omega - E_n + i\gamma} - \frac{1}{\omega + E_n - i\gamma} \right) \tag{A.6}$$

We can then substitute there a Lorentzian by doing

$$\frac{1}{\omega + E_n - i\gamma} = \frac{\omega + E_n + i\gamma}{(\omega + E_n)^2 - \gamma^2} \tag{A.7a}$$

$$\frac{1}{\omega - E_n + i\gamma} = \frac{\omega + E_n - i\gamma}{(\omega - E_n)^2 - \gamma^2} \tag{A.7b}$$

Taking into account the expression for a Lorentzian with center x_0 and width at half maximum Γ

$$L(x; x_0, \Gamma) = \frac{\Gamma}{2\pi} \frac{1}{(x - x_0)^2 + \frac{\Gamma^2}{4}}, \tag{A.8}$$

we can then write

$$-\frac{1}{\pi} \operatorname{Im} I(\omega, \gamma; F) = \sum_{n>0} f(E_n; F) \left[L(\omega, E_n, 2\gamma) + L(\omega, -E_n, 2\gamma) \right] \tag{A.9}$$

If we assume that there are no physical eigenvalues close to 0[1] and that γ is small enough, we can then take only the positive-energy centered Lorentzian. By using $\lim_{\Gamma \to 0} L(x; x_0, \Gamma) = \delta(x - x_0)$, then we can take

$$S(\omega; F) = -\frac{1}{\pi} \lim_{\gamma \to 0} \operatorname{Im} I(\omega, \gamma; F) \tag{A.10}$$

A.2 One-body operators in matrix form

Let F be a one-body operator written in the second quantization formalism

$$F = \sum_{ij} f_{ij} c_i^\dagger c_j. \tag{A.11}$$

As F is Hermitian, $f_{ij} = f_{ji}^*$. Using the fermion anticomutation relations then one can write

$$F = \underbrace{\sum_{ij} f_{ii}}_{\equiv f_0} + \frac{1}{2} \sum_{ij} \left(f_{ij} c_i^\dagger c_j - f_{ji}^* c_j^\dagger c_i \right) = f_0 + \frac{1}{2} \begin{pmatrix} c^\dagger & c \end{pmatrix} \begin{pmatrix} f & \\ & -f^\intercal \end{pmatrix} \begin{pmatrix} c \\ c^\dagger \end{pmatrix} \tag{A.12}$$

Now, let's take a particle number non-conserving Hermitean one body operator of the form

$$g = \frac{1}{2} \sum_{ij} g_{ij}^{20} c_i^\dagger c_j^\dagger + \frac{1}{2} \sum_{ij} g_{ij}^{02} c_j c_i \tag{A.13}$$

with $g_{ij}^{20^*} = g_{ij}^{02}$ and $g_{ij}^{20} = -g_{ji}^{20}$, $g_{ij}^{02} = -g_{ji}^{02}$. Here it is straightforward to see that

$$g = \frac{1}{2} \begin{pmatrix} c^\dagger & c \end{pmatrix} \begin{pmatrix} & g^{20} \\ -g^{02} & \end{pmatrix} \begin{pmatrix} c \\ c^\dagger \end{pmatrix} \tag{A.14}$$

[1] Spurious 0-energy modes are in general not accounted for the calculation of the strength function

Appendix B

Detailed derivations for JD

B.1 Stability of RQI

Let $M \in \mathbb{C}^{n\times n}$, $\nu \in \mathbb{R}^{n\times n}$. Let u be a Ritz vector of non-vanishing norm. We want to prove that $\rho(u)$ is stationary when $u = x_n$ an ν-eigenvalue of M. To do so, we take the derivative of $\rho(u)$ with respect to a component of u. Without loss of generality, let's assume $u^\dagger \nu u = \pm 1$. This gives

$$\frac{\partial \rho}{\partial u_i}(u) = \left(u^\dagger M\right)_i (u^\dagger \nu u) - \left(u^\dagger M u\right)\left(u^\dagger \nu\right)_i \tag{B.1}$$

For $u = x_n$, $\left(u^\dagger M\right)_i = \lambda_n \left(x_n^\dagger \nu\right)_i$ and $\left(u^\dagger M u\right) = \lambda_n \left(x_n^\dagger \nu x_n\right)$, obtaining

$$\frac{\partial \rho}{\partial x_n^i}(x_n) = 0 \; \forall i. \tag{B.2}$$

Which is what we wanted to prove.

B.2 Local onvergence of RQI

Let the Ritz vector u of non-zero ν-norm η_ν be expressed as a sum of an eigenvalue and a vector d ν-orthogonal to it

$$u = \alpha x_n + \delta d, \tag{B.3}$$

with $\alpha, \beta \in \mathbb{C}$ and x_n, d having ν-norm η either 1 or -1. The ν-norm of the vector u can be written as

$$\eta_u = u^\dagger \nu u = |\alpha|^2 \eta_x + |\delta|^2 \eta_d. \tag{B.4}$$

Where we used $x^\dagger \nu = 0$. By multiplying the expression by η_u and η_x and rearranging the terms, one obtains

$$\eta_x - |\alpha|^2 \eta_u = |\delta|^2 \eta_u \eta_{x_n} \eta_d \tag{B.5}$$

Let's now compare the difference between the target eigenvalue and the Ritz vector

$$\lambda_n - \rho(u) = \eta_{x_n} x_n^\dagger M x_n - \eta_u u^\dagger M u = |\delta|^2 d^\dagger \left(\lambda_n \eta_u \eta_{x_n} \eta_d \nu - M\right) d. \tag{B.6}$$

Which means that

$$|\lambda_n - \rho(u)| = O\left(|\delta|^2\right) \tag{B.7}$$

Now, let's see what happens with an RQI iteration. Save normalization, the RQI iteration is obtained as

$$u_{n+1} = \left(M - \rho_k \nu\right)^{-1} \nu u_k \tag{B.8}$$

with $\rho_k \equiv \rho(u_k)$. By taking into consideration that

$$(M - \rho_k \nu)x_n = (\lambda_n - \rho_k)\nu x_n \rightarrow \frac{1}{\lambda_n - \rho_k} x_n = (M - \rho_k \nu)^{-1} \nu x_n. \tag{B.9}$$

Then by considering $u_k = \alpha_k x_n + \delta_k d_k$, then

$$u_{n+1} = \frac{\alpha_k}{\lambda_n - \rho_k} x_n + \delta_k (M - \rho_k \nu)^{-1} \nu d \tag{B.10}$$

There, as we need to write the new vector as $u_{k+1} = \alpha_k x_n + \delta_k d_k$, then we can rewrite

$$u_{n+1} = \alpha_{k+1} \left(x_n + \frac{\lambda_n - \rho_k}{\alpha_k} \delta_k (M - \rho_k \nu)^{-1} \nu d \right). \tag{B.11}$$

From equation B.7, we see that $\lambda_n - \rho_k$ scales as $|\delta_k|^2$. By checking the part not included in x_n, as there is a δ_k term in it, then

$$\delta_{k+1} = O\left(|\delta_k|^3\right). \tag{B.12}$$

Which proves that RQI converges cubically. This same proof can be invoked to asses that in equation 6.14.

B.3 Solving exactly the correction equation

Having access to FAM, we can exactly solve the correction equation. This can be done by only calling once the FAM algorithm. To do so, we start from the multiple eigenvalue version of equation 6.15, which reads

$$(I - \nu Q \Xi Q^\dagger)(M - \rho\nu)t = -r \tag{B.13}$$

This can be rewriten as

$$t = (M - \rho\nu)^{-1}\nu\tilde{Q}\alpha - \underbrace{(M - \rho\nu)^{-1} r}_{u} = (M - \rho\nu)^{-1}\nu\tilde{Q}\alpha - u \tag{B.14}$$

with

$$\alpha \equiv \Xi \tilde{Q}^\dagger (M - \rho\nu)^{-1} t \tag{B.15}$$

Exploiting the fact that $\tilde{Q}^\dagger \nu t = 0$, applying $\tilde{Q}^\dagger \nu$ on the left one obtains

$$W\alpha = Z \tag{B.16}$$

with

$$W = \tilde{Q}^\dagger \nu (M - \rho\nu)^{-1} \nu \tilde{Q}, \quad Z = \tilde{Q}^\dagger \nu u. \tag{B.17}$$

Then solving the correction equation can be achieved following the steps:

1. Calculate W and Z via equation B.17.
2. Calculate $\alpha = W^{-1}Z$.
3. Obtain t from equation B.14.

The number of FAM calls can be reduced to one by using the same trick as in B.9. Then, one can write

$$(M - \rho\nu)^{-1}\nu\tilde{Q}^\dagger = \left((M - \rho\nu)^{-1}\nu u \quad \tfrac{1}{\omega_1 - \rho} x_1 \quad \tfrac{1}{\omega_2 - \rho} x_2 \quad \ldots \right) \equiv \Gamma \tag{B.18}$$

Which implies that FAM only has to be used once with $-f = \nu u$. Doing this, solving the correction equation becomes:

1. Calculate Γ with equation B.18 with one FAM call to calculate the first component.
2. Calculate $W = \tilde{Q}^{\dagger} v \Gamma$, $Z = \tilde{Q}^{\dagger} v u$
3. Calculate $\alpha = W^{-1} Z$
4. Obtain t as $t = \Gamma \alpha - u$.

Appendix C

Proofs involving the QRPA vacuum

C.1 Expression of $\mathbf{X}^{-1}$

ç If the **B** matrix is positive definite, then $\mathbf{X}^{-1}$ exists [137]. One can find an explicit expression for it by starting from the closure relation

$$\mathbf{X}\mathbf{X}^{\dagger} - \mathbf{Y}^{*}\mathbf{Y}^{\intercal} = I \tag{C.1}$$

Multiplying on the left by $\mathbf{X}^{-1}$ one obtains

$$\mathbf{X}^{-1} = \mathbf{X}^{\dagger} - \mathbf{X}^{-1}\mathbf{Y}^{*}\mathbf{Y}^{\intercal} \tag{C.2}$$

Which is a recurrence relation for $\mathbf{X}^{-1}$, thus it can be written as an infinte series

$$\mathbf{X}^{-1} = \sum_{n=0}^{\infty}(-1)^{n}\mathbf{X}^{\dagger}\left(\mathbf{Y}^{*}\mathbf{Y}^{\intercal}\right)^{n} \tag{C.3}$$

C.2 Symmetry of the correlation matrix

Even if the correlation matrix **C** is symmetric by definition, one can also check that the resulting expression is indeed symmetric. To do so, we write

$$\mathbf{C}^{*} = \mathbf{Y}\mathbf{X}^{-1} \tag{C.4}$$

By substituting C.3 and taking the transpose one obtains

$$\mathbf{C}^{*\intercal} = \sum_{n=0}^{\infty}(-1)^{n}\left(\mathbf{Y}\mathbf{Y}^{\dagger}\right)^{n}\mathbf{X}^{*}\mathbf{Y}^{\intercal} \tag{C.5}$$

By repeatedly applying $\mathbf{Y}^{\dagger}\mathbf{X}^{*} = \mathbf{X}^{\dagger}\mathbf{Y}^{*}$, one gets

$$\mathbf{C}^{\intercal} = \mathbf{C} \tag{C.6}$$

C.3 Order in C of products of Y

We can write the product of two **Y** matrices as an infinite series

$$\mathbf{Y}\mathbf{Y}^{\dagger} = \mathbf{C}^{*}\mathbf{X}\mathbf{X}^{\dagger}\mathbf{C} = \mathbf{C}^{*}\mathbf{C} + \mathbf{C}^{*}\mathbf{Y}^{*}\mathbf{Y}^{\intercal}\mathbf{C} \tag{C.7}$$

Applying recursively the closure formula,

$$\mathbf{Y}\mathbf{Y}^{\dagger} = \sum_{n=1}^{\infty} (\mathbf{C}^{*}\mathbf{C})^{n}, \tag{C.8}$$

from which we can infer that the square of the Y coefficients is of the order of the square of C.

C.4 Pauli corrected C matrix in spherical RPA

In reference [73], the single-particle occupancies are calculated of the RPA ground state are calculated using a spherical RPA. The one-half Pauli-correction factor is calculated at the levels of the densities, not the correlation matrix. However, one can make arise the one-half factor at the correlation matrix. For that we need to study the symmetry properties of the correlation matrix at spherical symmetry. The spherical correlation operator reads [130]

$$S = -\frac{1}{2} \sum_{ph\, p'h'\pi JM} C^{\pi J}_{ph\, p'h'} (-1)^{J-M} A^{\dagger}_{ph}(\pi, J, M) A^{\dagger}_{p'h'}(\pi, J, -M) \tag{C.9}$$

with the coupled ph operator being

$$A^{\dagger}_{ph}(\pi JM) = \sum_{m_p m_h} (-1)^{j_h - m_h} \left\langle j_p\, m_p\, j_h\, -m_h \middle| J\, M \right\rangle a^{\dagger}_{p\, m_p} a_{h\, m_h} \tag{C.10}$$

The Wigner 6-j symbol are defined as [140]

$$\begin{Bmatrix} j_1 & j_2 & j_3 \\ j_4 & j_5 & j_6 \end{Bmatrix} = \sum_{\text{all } m} (-1)^{\sum_k (j_k + m_k)} \begin{pmatrix} j_1 & j_2 & j_3 \\ m_1 & m_2 & m_3 \end{pmatrix} \begin{pmatrix} j_1 & j_5 & j_6 \\ -m_1 & m_5 & -m_6 \end{pmatrix} \begin{pmatrix} j_4 & j_2 & j_6 \\ -m_4 & -m_2 & m_6 \end{pmatrix} \begin{pmatrix} j_4 & j_5 & j_3 \\ m_4 & -m_5 & -m_3 \end{pmatrix} \tag{C.11}$$

The following formula can be derived

$$\begin{pmatrix} j_1 & j_2 & j_3 \\ m_1 & m_2 & m_3 \end{pmatrix} \begin{Bmatrix} j_1 & j_2 & j_3 \\ j_4 & j_5 & j_6 \end{Bmatrix} = \sum_{m_4 m_5 m_6} (-1)^{j_4 + j_5 + j_6 + m_4 + m_5 + m_6} \begin{pmatrix} j_1 & j_5 & j_6 \\ m_1 & m_5 & -m_6 \end{pmatrix} \begin{pmatrix} j_4 & j_2 & j_6 \\ -m_4 & m_2 & m_6 \end{pmatrix} \begin{pmatrix} j_4 & j_5 & j_3 \\ m_4 & -m_5 & m_3 \end{pmatrix} \tag{C.12}$$

Which using the orthogonality condition of the 3-j symbols, can be turned into

$$\begin{aligned} \sum_{j_3 m_3} (-1)^{j_3} (2j_3 + 1) \begin{pmatrix} j_1 & j_2 & j_3 \\ m_1 & m_2 & -m_3 \end{pmatrix} \begin{pmatrix} j_4 & j_5 & j_3 \\ m_4 & m_5 & m_3 \end{pmatrix} \begin{Bmatrix} j_1 & j_2 & j_3 \\ j_4 & j_5 & j_6 \end{Bmatrix} = \\ = \sum_{m_6} (-1)^{j_6 - m_4 + m_5 + m_6} \begin{pmatrix} j_1 & j_5 & j_6 \\ m_1 & m_5 & -m_6 \end{pmatrix} \begin{pmatrix} j_4 & j_2 & j_6 \\ m_4 & m_2 & m_6 \end{pmatrix} \end{aligned} \tag{C.13}$$

In the case of symmetry-less RPA, we could check very easily that $C_{php'h'} = -C_{p'hp'h}$. However, in spherical RPA, the presence of the Clebsch-Gordan coefficients makes this relation a bit more

obscure. However, we can get by a similar result. To do so, let's express the correlation operator in terms of 3-j symbols and reorder the creation and annihilation operators

$$C = -\frac{1}{2}\sum_{ph\,p'h'\pi JM} C^{\pi J}_{ph\,p'h'}(-1)^{J-M+1}(2J+1) \\ (-1)^{-j_p-m_h}\begin{pmatrix} j_p & j_h & J \\ m_p & -m_h & -M\end{pmatrix}(-1)^{-j_{p'}-m_{h'}}\begin{pmatrix} j_{p'} & j_{h'} & J \\ m_{p'} & -m_{h'} & M\end{pmatrix} a^\dagger_p a_{h'} a^\dagger_{p'} a_h \tag{C.14}$$

where we used $(-1)^{2k} = -1$ for k half-integer. We can now apply (C.13) to obtain

$$C = -\frac{1}{2}\sum_{ph\,p'h'\pi JIM} C^{\pi J}_{ph\,p'h'}(-1)^{I+m_{p'}+m_h+1}(2J+1)(2I+1)\begin{Bmatrix} j_p & j_h & I \\ j_{p'} & j_{h'} & J\end{Bmatrix} \\ (-1)^{-j_p-m_{h'}}\begin{pmatrix} j_p & j_{h'} & I \\ m_p & -m_{h'} & -M\end{pmatrix}(-1)^{-j_{p'}-m_h}\begin{pmatrix} j_{p'} & j_h & I \\ m_{p'} & -m_h & M\end{pmatrix} a^\dagger_p a_{h'} a^\dagger_{p'} a_h. \tag{C.15}$$

where we used $(-1)^K = (-1)^{-K}$ for K integer. By using $m_{p'} - m_h = -M$ and $(-1)^{2m_h} = -1$

$$C = -\frac{1}{2}\sum_{ph\,p'h'\pi JIM} C^{\pi I}_{ph\,p'h'}(2I+1)\begin{Bmatrix} j_p & j_h & J \\ j_{p'} & j_{h'} & I\end{Bmatrix}(-1)^{J-M}A^\dagger_{ph'}(\pi,J,M)A^\dagger_{p'h}(\pi,J,-M). \tag{C.16}$$

which gives us the identity

$$C^{\pi J}_{ph'\,ph'} = \sum_I C^{\pi I}_{ph\,p'h'}(2I+1)\begin{Bmatrix} j_p & j_h & J \\ j_{p'} & j_{h'} & I\end{Bmatrix} \tag{C.17}$$

In reference [73], the following identity is obtained when deriving the spherical equivalent of equation 7.21

$$Y^{npiJ^*}_{ph} = \sum_{p'h'}\left(C^{\pi J}_{ph'\,ph'} + \sum_I C^{\pi I}_{ph\,p'h'}(2I+1)\begin{Bmatrix} j_p & j_h & J \\ j_{p'} & j_{h'} & I\end{Bmatrix}\right)X^{npiJ^*}_{ph}. \tag{C.18}$$

Recognizing C.17 in this equation, then we can write

$$Y^{npiJ^*}_{ph} = \sum_{p'h'} 2C^{\pi J}_{ph'\,ph'}X^{npiJ^*}_{ph}. \tag{C.19}$$

Which is exactly the one-half correction for the quasiboson correlation matrix.

Résumé en français

Motivation physique

Les fonctions de force des rayonnements gamma sont l'un des éléments les plus importants dans les modèles de réactions nucléaires. Elles permettent de mesurer la probabilité qu'un noyau capture un photon d'énergie et de multipolarité données. Actuellement, les données expérimentales concernant ces fonctions de force ne sont disponibles que pour environ 200 noyaux, tous situés dans la vallée de stabilité. Cependant, il existe un intérêt croissant pour modéliser les réactions dans les noyaux exotiques, en particulier dans le cadre des processus astrophysiques, tels que la nucléosynthèse. C'est pourquoi les prédictions théoriques deviennent essentielles.

Dans cette thèse, nous utilisons la méthode QRPA (quasi-particle random phase approximation) pour effectuer des prédictions concernant les fonctions de force dipolaires pour l'ensemble des noyaux de la charte nucléaire. L'objectif est de fournir des estimations plus précises des propriétés nucléaires dans des régions encore peu explorées expérimentalement, en particulier celles liées à la physique des noyaux exotiques et aux processus astrophysiques.

Approximation de phase aléatoire de quasi-particules (QRPA)

L'approximation de phase aléatoire de quasi-particules, ou QRPA (pour "Quasi-Particle Random Phase Approximation" en anglais), est la seule méthode microscopique ayant permis de produire des fonctions de force à partir d'études systématiques. Elle repose sur la méthode Hartree-Fock-Bogolioubov (HFB), qui fournit une description au premier ordre de l'état fondamental nucléaire. Dans le cadre de la HFB, l'état fondamental est exprimé comme un produit d'opérateurs de quasi-particules. En revanche, la QRPA modélise les états excités nucléaires, qui sont représentés comme une combinaison linéaire d'excitations et de dés-excitations à deux quasi-particules.

L'un des avantages majeurs de la QRPA est que dès qu'un minimum est trouvé sur la surface d'énergie potentielle HFB, la QRPA est bien définie et stable. Cela la distingue d'autres méthodes, comme la PGCM (Projective Generator Coordinate Method), où les degrés de liberté collectifs doivent être identifiés au cas par cas. D'autre part, bien que le coût computationnel soit très élevé, la QRPA reste praticable même pour les noyaux les plus lourds. Toutefois, en raison de ce coût computationnel élevé, il n'existe qu'une seule étude QRPA déformée couvrant l'intégralité de la charte nucléaire.

Dans cette thèse, deux dérivations de la QRPA sont présentées : celle basée sur les équations du mouvement, et celle fondée sur la théorie de la réponse linéaire. Cette dernière constitue la base de la méthode d'Amplitude Finie (FAM).

La FAM est l'une des méthodes itératives de la QRPA, qui permet de calculer une partie de la solution de la QRPA avec un coût computationnel significativement réduit. Dans le cas de la FAM, on obtient directement la fonction de force pour une multipolarité donnée. Cette méthode est utilisée dans deux nouvelles études systématiques QRPA déformées : la première couvrant

l'ensemble de la charte nucléaire avec une interaction effective covariante, et la deuxième utilisant une interaction chirale qui inclut des noyaux jusqu'au fer en numéro atomique. Pour la première étude, nous utilisons le code DIRQFAM, et pour la deuxième, nous faisons appel au solveur QRPA PANACEA.

Dans le cadre de cette thèse, le code PANACEA a été amélioré par l'ajout de la méthode GMRES (Generalized Minimum Residual Method) pour résoudre la FAM. Cette amélioration permet au code de converger environ trois fois plus rapidement et d'être plus numériquement stable.

Première étude systématique : Interaction covariante DD-PC1

Dans cette partie de la thèse, nous calculons les fonctions de force E1 pour tous les noyaux jusqu'à Z = 110. Cette étude constitue la deuxième étude systématique QRPA déformée, et la première réalisée avec une interaction covariante. Pour atteindre cet objectif, nous avons utilisé le code DIRQFAM, qui implémente le formalisme FAM avec l'interaction DD-PC1, une interaction relativiste dépendant de la densité. La réponse QRPA est construite à partir d'un état RHB (Hartree-Bogolyubov Relativiste), qui offre une description équivalente à celle de la HFB pour l'état fondamental, sans tenir compte des termes d'échange.

L'étude commence par la résolution d'un problème de convergence rencontré par le code. Dans sa version de base, le code implémente une formule analytique qui fixe la valeur du paramètre de fréquence de l'oscillateur harmonique, cette valeur étant uniquement dépendante de la masse. Toutefois, cette valeur ne minimise pas l'énergie de liaison RHB. En la minimisant pour chaque noyau, nous obtenons une réponse QRPA convergée. Grâce à cette méthode, nous avons calculé environ 1600 fonctions de force E1 pour les noyaux pairs-pairs. Pour les noyaux impairs, nous avons calculé leur fonction de force comme étant la moyenne géométrique des noyaux pairs voisins.

Les résultats obtenus sont comparés aux données expérimentales. Les centroids et largeurs des fonctions de force expérimentales sont reproduits avec une déviation de la racine carrée de la moyenne des carrés (RMS) inférieure à 0,65 MeV pour les centroids et 0,45 MeV pour les largeurs. Ces déviations ont été obtenues sans aucune correction empirique. Les études QRPA précédentes ont nécessité ce type de correction pour obtenir des déviations similaires. De plus, le comportement des fonctions de force a été étudié en fonction du nombre de particules et de la déformation. Nous avons observé que les fermetures de couches entraînent un rétrécissement des fonctions de force et un déplacement vers des énergies plus élevées. Nous avons également vérifié la validité des règles empiriques utilisées pour caractériser les fonctions de force des noyaux déformés dans les études précédentes avec la QRPA sphérique. Bien qu'une des règles soit suivie assez fidèlement, l'autre ne s'avère valide que pour de petites valeurs de déformation quadripolaire.

Ayant calculé les fonctions de force E1 pour tous les noyaux, nous laissons comme perspective de cette étude l'implémentation de ces résultats dans le célèbre code de réactions nucléaires TALYS. À ce jour, seules les fonctions de force E1 ont été calculées ; le calcul des transitions M1 et E2 reste une extension naturelle de cette étude.

Seconde étude systématique : Interaction chirale

Au cours des dernières décennies, un fort développement des interactions internucléoniques basées sur la chromodynamique quantique a eu lieu, grâce à la théorie effective des champs chiraux (χEFT). Grâce au concept de comptage de puissance ("Power Counting" en anglais), les termes d'interaction dérivés de cette théorie peuvent être ordonnés selon une hiérarchie d'importance : LO (leading order, ordre principal en anglais), NLO (next-to-leading order, ordre suivant à l'ordre

principal), N2LO (next-to-next-to-leading order, ordre suivant à l'ordre suivant à l'ordre principal), et ainsi de suite. Il existe peu de travaux portant sur les études QRPA avec des interactions dérivées de la χEFT. Toutefois, ces études se concentrent sur un nombre limité de noyaux. Dans cette thèse, nous poursuivons la première étude systématique des transitions E1 avec des interactions relativistes jusqu'au fer. Nous nous focalisons sur les noyaux pour lesquels nous disposons de données expérimentales photonucléaires. Nous utilisons une famille d'interactions chirales jusqu'au troisième ordre d'expansion chirale (N3LO).

Dans un premier temps, nous constatons que les fonctions de force montrent une convergence avec l'expansion chirale, et que cette expansion converge vers les données expérimentales. Pour les noyaux de plus grande masse, la fonction de force s'étend vers des énergies plus élevées, s'éloignant des données expérimentales. Nous observons également que les erreurs liées à la troncation du nombre de couches de l'oscillateur harmonique et à la fréquence de l'oscillateur sont sous contrôle. Les résultats obtenus avec cette interaction décrivent les données expérimentales avec une précision similaire à celle des résultats obtenus avec des interactions effectives.

Enfin, nous comparons ces résultats avec ceux obtenus avec une autre interaction chirale, l'EM1.8/2.0, parfois appelée "magic interaction" dans le langage courant. Bien que les résultats reproduisent de manière similaire l'expérience, l'EM1.8/2.0 décale la fonction de force vers des énergies plus élevées par rapport à l'interaction N3LO utilisée précédemment.

Ces résultats marquent la première fois que la QRPA chirale est utilisée de manière systématique jusqu'au fer. Cela nous permet de mieux comprendre le comportement de la théorie avec ce type d'interactions. Dans le futur, comme dans le cas précédent, une extension aux transitions M1 et E2 pourrait être envisagée.

Étude du rôle de la triaxialité dans la réponse E1

Les études QRPA déformées de façon axiale, telles que celles présentées précédemment dans cette thèse, nécessitent de grandes ressources computationnelles. Cependant, plusieurs noyaux de la charte nucléaire présentent une symétrie triaxiale dans leur état fondamental HFB. La QRPA triaxiale est bien plus exigeante sur le plan computationnel que sa contrepartie axiale. C'est pourquoi, jusqu'à récemment, il n'existait pas d'études QRPA triaxiales. Cela a changé avec le développement de la méthode FAM, qui a ouvert la voie à une évaluation des fonctions de force QRPA avec un coût computationnel réduit. Des études avec des interactions de type Skyrme et des espaces de valence ont été réalisées. Dans cette étude, nous utilisons pour la première fois la QRPA triaxiale avec une interaction chirale.

Dans le régime de masse étudié précédemment, les noyaux Mg24 et S32 présentent un minimum triaxial en état fondamental HFB et ont des données expérimentales dans la région de la résonance géante. Nous avons étudié leur état fondamental HFB ainsi que leur réponse QRPA E1. Dans le cas de Mg24, la densité à un corps HFB montre six substructures. En intégrant la densité dans chaque sous-structure, nous retrouvons quatre particules, ce qui nous fait penser à un phénomène de clustering alpha. Dans le cas de S32, la surface de l'énergie potentielle HFB présente deux minimums : dans le minimum principal, la densité à un corps montre une structure clairement triaxiale, mais sans aucune trace de clustering. Dans le second minimum, la densité à deux corps montre deux sous-structures de 16 particules, ce qui rappelle un clustering 2 x O16.

Nous avons calculé les fonctions de force E1 triaxiales et axiales avec l'interaction N3LO de l'étude précédente. Ensuite, nous avons comparé les fonctions de force E1 calculées dans les minima axial et triaxial. D'un côté, la fonction de force triaxiale de Mg24 présente un troisième maximum entre les deux principaux maxima, ce qui est observé dans les données expérimentales mais pas dans la réponse axiale. Ce troisième maximum est une manifestation typique de ce type de

déformation. La fonction de force a été calculée pour plusieurs paramètres de déformation triaxiale γ, et nous avons observé que l'apparition du troisième maximum se fait de manière assez soudaine à mesure que l'on approche du minimum.

Dans le cas de S32, la fonction de force est bien plus fragmentée dans le cas triaxial que dans le cas axial, ce qui est en accord avec les données expérimentales. En revanche, la hiérarchie entre les différents maxima n'est pas parfaitement reproduite en comparaison avec les données expérimentales.

Une nouvelle méthode pour résoudre la QRPA : la méthode Jacobi-Davidson exacte

Dans le cadre de cette thèse, nous avons utilisé la méthode FAM pour obtenir de manière rapide les fonctions de force QRPA. La QRPA est l'une des méthodes itératives permettant de récupérer une partie de la solution QRPA sans avoir à supporter le coût computationnel élevé associé à la formulation traditionnelle de cette théorie. Cependant, dans certains cas, il peut être nécessaire de se concentrer sur l'obtention de certaines valeurs propres de la QRPA, plutôt que sur la fonction de force elle-même. Par exemple, cela peut inclure le calcul des énergies d'excitation à basse énergie ou des contributions individuelles à l'énergie de corrélation, parmi d'autres applications possibles. Il existe plusieurs méthodes dans la littérature pour atteindre cet objectif, telles que la méthode d'intégration complexe FAM ou la méthode Arnoldi. Toutefois, ces méthodes présentent certaines limites. Par exemple, la première nécessite une estimation approximative de la position des états propres.

Dans cette étude, nous proposons une nouvelle méthode, conceptuellement similaire à la méthode d'Arnoldi, mais qui utilise FAM pour évaluer le produit entre l'inverse de la matrice QRPA et un vecteur arbitraire. La méthode repose sur l'algorithme itératif de Jacobi-Davidson, et l'utilisation de FAM permet de tirer parti de sa version exacte, garantissant ainsi une convergence cubique. Cette approche est implémentée dans le code PANACEA, que nous avons utilisé dans d'autres parties de cette thèse. Nous avons testé la performance de l'algorithme, et les résultats obtenus sont identiques à ceux obtenus en résolvant la matrice QRPA avec des interactions modèles en couches. Nous avons également obtenu des résultats similaires à ceux obtenus avec la méthode FAM, en utilisant des interactions chirales et Gogny.

L'algorithme s'est montré capable de trouver des valeurs propres de manière très efficace, en nécessitant seulement une ou deux itérations par valeur propre. La partie la plus coûteuse de l'algorithme réside dans l'appel à FAM à chaque itération. Nous avons observé que, pour les parties basses du spectre énergétique, le nombre d'itérations FAM reste raisonnable. En revanche, pour des énergies plus élevées, ce nombre peut augmenter de manière exponentielle. Toutefois, ce comportement peut être contrôlé en ajoutant une petite partie complexe à l'énergie d'échantillonnage. Nous avons démontré la capacité de notre méthode en calculant les dix premières valeurs propres pour le noyau U238 avec l'interaction Gogny. Nous avons ainsi pu obtenir l'ensemble du spectre avec seulement 10 itérations JD et 6 heures de temps de calcul. À titre de comparaison, pour effectuer une diagonalisation complète, il serait nécessaire de disposer d'un temps de calcul compris entre 1000 et 10000 fois supérieur, ce qui démontre l'accélération considérable que permet notre approche, en particulier lorsque l'on s'intéresse uniquement à une partie du spectre.

Une correction de Pauli pour l'état fondamental QRPA

Afin de dériver la QRPA, l'approximation de quasibosons est utilisée, dans laquelle on suppose que les opérateurs de création-destruction à deux quasiparticules obéissent aux règles de commutation bosoniques. Cette approximation entraîne une brisure partielle du principe de Pauli. Bien que la QRPA soit principalement utilisée pour caractériser les états excités, elle fournit également une forme analytique pour l'état fondamental, qui intègre des corrélations manquantes dans l'état HFB. Cependant, la brisure du principe de Pauli dans la QRPA conduit à une surestimation des corrélations. Afin de corriger cette brisure, plusieurs prescriptions ont été proposées dans la littérature pour ajuster certains observables, tels que les occupations monoparticulaires et les énergies de liaison. Toutefois, ces corrections ont principalement été appliquées aux noyaux à couche fermée (dans le cas de la RPA, sans la composante Q).

Dans ce chapitre, nous généralisons ces prescriptions pour le cas des noyaux à couche ouverte et les appliquons spécifiquement aux énergies de corrélation QRPA. La correction obtenue consiste à diviser l'énergie de corrélation par un facteur d'un tiers. On retrouve ainsi la correction habituelle de un demi dans le cas où l'appariement est nul. Après avoir effectué les dérivations numériques, plusieurs tests ont été réalisés. D'une part, les énergies de corrélation RPA ont été calculées en imposant un seuil (cutoff) sur l'énergie des phonons. Nous avons utilisé l'interaction effective Gogny D1M pour ces calculs. Il a été observé que les énergies de corrélation divergent avec la taille de la base d'oscillateur harmonique utilisée, et ce, pour tous les noyaux calculés.

Afin de vérifier que cette divergence n'était pas simplement due à l'absence des termes spin-orbit et densité dans l'interaction Gogny (qui ont une portée nulle), nous avons répété les calculs avec l'interaction de Brink et Boeker, ce qui a confirmé la tendance divergente des énergies de corrélation. Cela implique que, pour utiliser les énergies de corrélation QRPA dans des applications pratiques, il est nécessaire de définir un critère de coupure pour les phonons inclus dans les calculs.

D'autre part, les résultats des énergies de corrélation QRPA et RPA corrigées ont été comparés pour le noyau O16. Il a été trouvé que, pour un critère de coupure des phonons compris entre 25 et 40 MeV, les corrections obtenues sont pratiquement identiques, ce qui confirme la validité de notre approche.

Bibliography

[1] Y. T. Oganessian, V. Utyonkov, Y. V. Lobanov, F. S. Abdullin, A. Polyakov, R. Sagaidak, I. Shirokovsky, Y. S. Tsyganov, A. Voinov, G. Gulbekian, *et al.*, "Synthesis of the isotopes of elements 118 and 116 in the ^{249}Cf and ^{245}Cm + ^{48}Ca fusion reactions," *Physical Review C–Nuclear Physics*, vol. 74, no. 4, p. 044602, 2006.

[2] R. Machleidt, "What is ab initio?," *Few-Body Systems*, vol. 64, no. 4, p. 77, 2023.

[3] A. Ekström, C. Forssén, G. Hagen, G. Jansen, W. Jiang, and T. Papenbrock, "What is ab initio in nuclear theory?," *Frontiers in Physics*, vol. 11, p. 1129094, 2023.

[4] P. Ring and P. Schuck, *The nuclear many-body problem*. Springer Science & Business Media, 2004.

[5] N. Schunck, *Energy density functional methods for atomic nuclei*. IoP Publishing, 2019.

[6] J. R. Stone and P.-G. Reinhard, "The Skyrme interaction in finite nuclei and nuclear matter," *Progress in Particle and Nuclear Physics*, vol. 58, no. 2, pp. 587–657, 2007.

[7] L. Robledo, T. Rodríguez, and R. Rodríguez-Guzmán, "Mean field and beyond description of nuclear structure with the Gogny force: a review," *Journal of Physics G: Nuclear and Particle Physics*, vol. 46, no. 1, p. 013001, 2018.

[8] E. Chabanat, P. Bonche, P. Haensel, J. Meyer, and R. Schaeffer, "A Skyrme parametrization from subnuclear to neutron star densities. Part II. nuclei far from stabilities," *Nuclear Physics A*, vol. 635, no. 1-2, pp. 231–256, 1998.

[9] M. Kortelainen, J. McDonnell, W. Nazarewicz, P.-G. Reinhard, J. Sarich, N. Schunck, M. Stoitsov, and S. Wild, "Nuclear energy density optimization: Large deformations," *Physical Review C–Nuclear Physics*, vol. 85, no. 2, p. 024304, 2012.

[10] S. Goriely, N. Chamel, and J. Pearson, "Further explorations of Skyrme-Hartree-Fock-Bogoliubov mass formulas. XVI. inclusion of self-energy effects in pairing," *Physical Review C*, vol. 93, no. 3, p. 034337, 2016.

[11] J. Dechargé and D. Gogny, "Hartree-Fock-Bogolyubov calculations with the D1 effective interaction on spherical nuclei," *Physical Review C*, vol. 21, no. 4, p. 1568, 1980.

[12] S. Goriely, S. Hilaire, M. Girod, and S. Péru, "First Gogny-Hartree-Fock-Bogoliubov nuclear mass model," *Physical review letters*, vol. 102, no. 24, p. 242501, 2009.

[13] F. Chappert, N. Pillet, M. Girod, and J.-F. Berger, "Gogny force with a finite-range density dependence," *Physical Review C*, vol. 91, no. 3, p. 034312, 2015.

[14] L. Batail, D. Davesne, S. Péru, P. Becker, A. Pastore, and J. Navarro, "A three-ranged Gogny interaction in touch with pion exchange: promising results to improve infinite matter properties," *The European Physical Journal A*, vol. 59, no. 7, p. 173, 2023.

[15] G. Zietek, *Towards a generalized effective nuclear Gogny interaction extended to finite-range spin-orbit and tensor forces*. PhD thesis, Université Paris-Saclay, 2023.

[16] Y. Gambhir, P. Ring, and A. Thimet, "Relativistic mean field theory for finite nuclei," *Annals of Physics*, vol. 198, no. 1, pp. 132–179, 1990.

[17] P. Ring, "Relativistic mean field theory in finite nuclei," *Progress in Particle and Nuclear Physics*, vol. 37, pp. 193–263, 1996.

[18] H. Yukawa, "On the interaction of elementary particles. Is," *Proceedings of the Physico-Mathematical Society of Japan. 3rd Series*, vol. 17, pp. 48–57, 1935.

[19] H. Kucharek and P. Ring, "Relativistic field theory of superfluidity in nuclei," *Zeitschrift für Physik A Hadrons and Nuclei*, vol. 339, no. 1, pp. 23–35, 1991.

[20] W. H. Long, P. Ring, N. V. Giai, and J. Meng, "Relativistic Hartree-Fock-Bogoliubov theory with density dependent meson-nucleon couplings," *Physical Review C–Nuclear Physics*, vol. 81, no. 2, p. 024308, 2010.

[21] J.-P. Ebran, E. Khan, D. Pena Arteaga, and D. Vretenar, "Relativistic Hartree-Fock-Bogoliubov model for deformed nuclei," *Physical Review C–Nuclear Physics*, vol. 83, no. 6, p. 064323, 2011.

[22] J. Geng and W. H. Long, "Relativistic Hartree-Fock-Bogoliubov model for axially deformed nuclei," *Physical Review C*, vol. 105, no. 3, p. 034329, 2022.

[23] G. Lalazissis, T. Nikšić, D. Vretenar, and P. Ring, "New relativistic mean-field interaction with density-dependent meson-nucleon couplings," *Physical Review C–Nuclear Physics*, vol. 71, no. 2, p. 024312, 2005.

[24] T. Nikšić, D. Vretenar, and P. Ring, "Relativistic nuclear energy density functionals: Adjusting parameters to binding energies," *Physical Review C–Nuclear Physics*, vol. 78, no. 3, p. 034318, 2008.

[25] E. Yüksel, T. Marketin, and N. Paar, "Optimizing the relativistic energy density functional with nuclear ground state and collective excitation properties," *Physical Review C*, vol. 99, no. 3, p. 034318, 2019.

[26] H. Hergert, "A guided tour of ab initio nuclear many-body theory," *Frontiers in Physics*, vol. 8, p. 379, 2020.

[27] R. Machleidt and D. R. Entem, "Chiral effective field theory and nuclear forces," *Physics Reports*, vol. 503, no. 1, pp. 1–75, 2011.

[28] S. Weinberg, "Phenomenological Lagrangians," *Physica, A;(Netherlands)*, vol. 96, 1979.

[29] T. Hüther, K. Vobig, K. Hebeler, R. Machleidt, and R. Roth, "Family of chiral two-plus three-nucleon interactions for accurate nuclear structure studies," *Physics Letters B*, vol. 808, p. 135651, 2020.

[30] K. Hebeler, S. Bogner, R. Furnstahl, A. Nogga, and A. Schwenk, "Improved nuclear matter calculations from chiral low-momentum interactions," *Physical Review C–Nuclear Physics*, vol. 83, no. 3, p. 031301, 2011.

[31] J. Hoppe, C. Drischler, K. Hebeler, A. Schwenk, and J. Simonis, "Probing chiral interactions up to next-to-next-to-next-to-leading order in medium-mass nuclei," *Physical Review C*, vol. 100, no. 2, p. 024318, 2019.

[32] B. R. Barrett, P. Navrátil, and J. P. Vary, "Ab initio no core shell model," *Progress in Particle and Nuclear Physics*, vol. 69, pp. 131–181, 2013.

[33] R. Roth, J. Langhammer, A. Calci, S. Binder, and P. Navrátil, "Similarity-Transformed Chiral NN+3N Interactions for the Ab Initio Description of ^{12}C and ^{16}O," *Physical Review Letters*, vol. 107, no. 7, p. 072501, 2011.

[34] A. Tichai, P. Arthuis, T. Duguet, H. Hergert, V. Somá, and R. Roth, "Bogoliubov many-body perturbation theory for open-shell nuclei," *Physics Letters B*, vol. 786, pp. 195–200, 2018.

[35] P. Demol, T. Duguet, and A. Tichai, "Ab initio Bogoliubov many-body perturbation theory: Closed-form constraint on the average particle number," *arXiv preprint arXiv:2407.16841*, 2024.

[36] G. Hagen, T. Papenbrock, D. J. Dean, and M. Hjorth-Jensen, "Ab initio coupled-cluster approach to nuclear structure with modern nucleon-nucleon interactions," *Physical Review C–Nuclear Physics*, vol. 82, no. 3, p. 034330, 2010.

[37] A. Tichai, P. Demol, and T. Duguet, "Towards heavy-mass ab initio nuclear structure:Open-shell Ca, Ni and Sn isotopes from Bogoliubov coupled-cluster theory," *Physics Letters B*, vol. 851, p. 138571, 2024.

[38] H. Hergert, S. K. Bogner, T. D. Morris, A. Schwenk, and K. Tsukiyama, "The in-medium similarity renormalization group: A novel ab initio method for nuclei," *Physics reports*, vol. 621, pp. 165–222, 2016.

[39] H. Hergert, S. Binder, A. Calci, J. Langhammer, and R. Roth, "Ab initio calculations of even oxygen isotopes with chiral two-plus-three-nucleon interactions," *Physical Review Letters*, vol. 110, no. 24, p. 242501, 2013.

[40] M. Arnould, S. Goriely, and K. Takahashi, "The r-process of stellar nucleosynthesis: Astrophysics and nuclear physics achievements and mysteries," *Physics Reports*, vol. 450, no. 4-6, pp. 97–213, 2007.

[41] B. D. Metzger, G. Martínez-Pinedo, S. Darbha, E. Quataert, A. Arcones, D. Kasen, R. Thomas, P. Nugent, I. Panov, and N. T. Zinner, "Electromagnetic counterparts of compact object mergers powered by the radioactive decay of r-process nuclei," *Monthly Notices of the Royal Astronomical Society*, vol. 406, no. 4, pp. 2650–2662, 2010.

[42] M. N. Harakeh and A. Woude, *Giant Resonances: fundamental high-frequency modes of nuclear excitation*, vol. 24. Oxford Studies in Nuclear Phys, 2001.

[43] S. Goriely, P. Dimitriou, M. Wiedeking, T. Belgya, R. Firestone, J. Kopecky, M. Krtička, V. Plujko, R. Schwengner, S. Siem, *et al.*, "Reference database for photon strength functions," *The European Physical Journal A*, vol. 55, pp. 1–52, 2019.

[44] R. Capote, M. Herman, P. Obložinskỳ, P. Young, S. Goriely, T. Belgya, A. Ignatyuk, A. J. Koning, S. Hilaire, V. A. Plujko, *et al.*, "RIPL–reference input parameter library for calculation of nuclear reactions and nuclear data evaluations," *Nuclear Data Sheets*, vol. 110, no. 12, pp. 3107–3214, 2009.

[45] S. Goriely and V. Plujko, "Simple empirical E1 and M1 strength functions for practical applications," *Physical Review C*, vol. 99, no. 1, p. 014303, 2019.

[46] D. Savran, T. Aumann, and A. Zilges, "Experimental studies of the pygmy dipole resonance," *Progress in Particle and Nuclear Physics*, vol. 70, pp. 210–245, 2013.

[47] J. Piekarewicz, "Pygmy resonances and neutron skins," *Physical Review C–Nuclear Physics*, vol. 83, no. 3, p. 034319, 2011.

[48] S. Krewald, V. Klemt, J. Speth, and A. Faessler, "On the use of skyrme forces in self-consistent rpa calculations," *Nuclear Physics A*, vol. 281, no. 2, pp. 166–206, 1977.

[49] S. Péru and H. Goutte, "Role of deformation on giant resonances within the quasiparticle random-phase approximation and the Gogny force," *Physical Review C–Nuclear Physics*, vol. 77, no. 4, p. 044313, 2008.

[50] K. Yoshida and N. V. Giai, "Deformed quasiparticle-random-phase approximation for neutron-rich nuclei using the skyrme energy density functional," *Physical Review C–Nuclear Physics*, vol. 78, no. 6, p. 064316, 2008.

[51] N. Paar, D. Vretenar, E. Khan, and G. Colo, "Exotic modes of excitation in atomic nuclei far from stability," *Reports on Progress in Physics*, vol. 70, no. 5, p. R02, 2007.

[52] A. Ravlić, E. Yüksel, Y. Niu, G. Colò, E. Khan, and N. Paar, "Stellar electron-capture rates based on finite-temperature relativistic quasiparticle random-phase approximation," *Physical Review C*, vol. 102, no. 6, p. 065804, 2020.

[53] R. Trippel, "Collective excitations with chiral NN+3N interactions from coupled-cluster and in-medium SRG," 2016.

[54] Y. Beaujeault-Taudière, M. Frosini, J.-P. Ebran, T. Duguet, R. Roth, and V. Somà, "Zero- and finite-temperature electromagnetic strength distributions in closed-and open-shell nuclei from first principles," *Physical Review C*, vol. 107, no. 2, p. L021302, 2023.

[55] A. Porro, T. Duguet, J.-P. Ebran, M. Frosini, R. Roth, and V. Somá, "Ab initio description of monopole resonances in light-and medium-mass nuclei: I. Technical aspects and uncertainties of ab initio PGCM calculations," *The European Physical Journal A*, vol. 60, no. 6, p. 133, 2024.

[56] A. Porro, T. Duguet, J.-P. Ebran, M. Frosini, R. Roth, and V. Somà, "Ab initio description of monopole resonances in light-and medium-mass nuclei: Ii. ab initio PGCM calculations in ^{46}Ti, ^{28}Si and ^{24}Mg," *The European Physical Journal A*, vol. 60, no. 6, p. 134, 2024.

[57] E. Marshalek and J. Rasmussen, "Collective vibrations of spheroidal even nuclei," *Nuclear Physics*, vol. 43, pp. 438–471, 1963.

[58] S. Goriely and E. Khan, "Large-scale QRPA calculation of E1-strength and its impact on the neutron capture cross section," *Nuclear Physics A*, vol. 706, no. 1-2, pp. 217–232, 2002.

[59] S. Goriely, E. Khan, and M. Samyn, "Microscopic HFB+QRPA predictions of dipole strength for astrophysics applications," *Nuclear Physics A*, vol. 739, no. 3-4, pp. 331–352, 2004.

[60] M. Martini, S. Péru, S. Hilaire, S. Goriely, and F. Lechaftois, "Large-scale deformed quasiparticle random-phase approximation calculations of the γ-ray strength function using the Gogny force," *Physical Review C*, vol. 94, no. 1, p. 014304, 2016.

[61] S. Goriely, S. Hilaire, S. Péru, M. Martini, I. Deloncle, and F. Lechaftois, "Gogny-Hartree-Fock-Bogolyubov plus quasiparticle random-phase approximation predictions of the M1 strength function and its impact on radiative neutron capture cross section," *Physical Review C*, vol. 94, no. 4, p. 044306, 2016.

[62] J. Toivanen, B. Carlsson, J. Dobaczewski, K. Mizuyama, R. Rodríguez-Guzmán, P. Toivanen, and P. Veselỳ, "Linear response strength functions with iterative Arnoldi diagonalization," *Physical Review C–Nuclear Physics*, vol. 81, no. 3, p. 034312, 2010.

[63] B. Carlsson, J. Toivanen, and A. Pastore, "Collective vibrational states within the fast iterative quasiparticle random-phase approximation method," *Physical Review C–Nuclear Physics*, vol. 86, no. 1, p. 014307, 2012.

[64] A. Bjelčić, T. Nikšić, and Z. Drmač, "Chebyshev kernel polynomial method for efficient calculation of the quasiparticle random phase approximation response function," *Computer physics communications*, vol. 280, p. 108477, 2022.

[65] T. Nakatsukasa, T. Inakura, and K. Yabana, "Finite amplitude method for the solution of the random-phase approximation," *Physical Review C–Nuclear Physics*, vol. 76, no. 2, p. 024318, 2007.

[66] P. Avogadro and T. Nakatsukasa, "Finite amplitude method for the quasiparticle random-phase approximation," *Physical Review C–Nuclear Physics*, vol. 84, no. 1, p. 014314, 2011.

[67] N. Hinohara, M. Kortelainen, and W. Nazarewicz, "Low-energy collective modes of deformed superfluid nuclei within the finite-amplitude method," *Physical Review C–Nuclear Physics*, vol. 87, no. 6, p. 064309, 2013.

[68] N. Hinohara, M. Kortelainen, W. Nazarewicz, and E. Olsen, "Complex-energy approach to sum rules within nuclear density functional theory," *Physical review C*, vol. 91, no. 4, p. 044323, 2015.

[69] A. Bjelčić and N. Schunck, "Computing the QRPA level density with the Finite Amplitude Method," *arXiv preprint arXiv:2409.07644*, 2024.

[70] K. Washiyama and T. Nakatsukasa, "Multipole modes of excitation in triaxially deformed superfluid nuclei," *Physical review C*, vol. 96, no. 4, p. 041304, 2017.

[71] K. Washiyama, S. Ebata, and K. Yoshida, "Evolution of the giant monopole resonance with triaxial deformation," *Physical Review C*, vol. 109, no. 2, p. 024317, 2024.

[72] P. Ellis, "RPA ground state correlations from perturbation theory," *Nuclear Physics A*, vol. 155, no. 2, pp. 625–643, 1970.

[73] H. Lenske and J. Wambach, "RPA ground state correlations in nuclei," *Physics Letters B*, vol. 249, no. 3-4, pp. 377–380, 1990.

[74] N. Paar, P. Ring, T. Nikšić, and D. Vretenar, "Quasiparticle random phase approximation based on the relativistic Hartree-Bogoliubov model," *Physical Review C*, vol. 67, no. 3, p. 034312, 2003.

[75] A. Ravlić, *Stellar weak interaction processes at finite temperature based on the relativistic energy density functional theory*. PhD thesis, University of Zagreb. Faculty of Science. Department of Physics, 2023.

[76] S. Peru and M. Martini, "Mean field based calculations with the Gogny force: Some theoretical tools to explore the nuclear structure," *The European Physical Journal A*, vol. 50, pp. 1–35, 2014.

[77] A. Baran, A. Bulgac, M. M. Forbes, G. Hagen, W. Nazarewicz, N. Schunck, and M. V. Stoitsov, "Broyden's method in nuclear structure calculations," *Physical Review C–Nuclear Physics*, vol. 78, no. 1, p. 014318, 2008.

[78] A. Bjelčić and T. Nikšić, "Implementation of the quasiparticle finite amplitude method within the relativistic self-consistent mean-field framework (II): The program DIRQFAM v2. 0.0," *Computer Physics Communications*, vol. 287, p. 108689, 2023.

[79] M. Frosini and et al., "To be publsished,"

[80] V. Plujko, O. Gorbachenko, R. Capote, and P. Dimitriou, "Giant dipole resonance parameters of ground-state photoabsorption: Experimental values with uncertainties," *Atomic Data and Nuclear Data Tables*, vol. 123, pp. 1–85, 2018.

[81] H. Loens, K. Langanke, G. Martínez-Pinedo, and K. Sieja, "M1 strength functions from large-scale shell-model calculations and their effect on astrophysical neutron capture cross-sections," *The European Physical Journal A*, vol. 48, pp. 1–17, 2012.

[82] K. Sieja, "Electric and magnetic dipole strength at low energy," *Physical Review Letters*, vol. 119, no. 5, p. 052502, 2017.

[83] A. Koning, S. Hilaire, and S. Goriely, "TALYS: modeling of nuclear reactions," *The European Physical Journal A*, vol. 59, no. 6, p. 131, 2023.

[84] I. Daoutidis and S. Goriely, "Large-scale continuum random-phase approximation predictions of dipole strength for astrophysical applications," *Physical Review C–Nuclear Physics*, vol. 86, no. 3, p. 034328, 2012.

[85] S. Goriely, S. Hilaire, S. Péru, and K. Sieja, "Gogny-HFB+QRPA dipole strength function and its application to radiative nucleon capture cross section," *Physical Review C*, vol. 98, no. 1, p. 014327, 2018.

[86] A. Bjelčić and T. Nikšić, "Implementation of the quasiparticle finite amplitude method within the relativistic self-consistent mean-field framework: The program DIRQFAM," *Computer physics communications*, vol. 253, p. 107184, 2020.

[87] T. Nikšić, N. Paar, D. Vretenar, and P. Ring, "DIRHB—A relativistic self-consistent mean-field framework for atomic nuclei," *Computer physics communications*, vol. 185, no. 6, pp. 1808–1821, 2014.

[88] F. Mercier, A. Bjelčić, T. Nikšić, J.-P. Ebran, E. Khan, and D. Vretenar, "Low-energy cluster modes in N=Z nuclei," *Physical Review C*, vol. 103, no. 2, p. 024303, 2021.

[89] S. A. Moszkowski, "Models of nuclear structure," *Handbuch der Physik*, vol. 39, pp. 411–550, 1957.

[90] J. Blomqvist and A. Molinari, "Collective 0^- vibrations in even spherical nuclei with tensor forces," *Nuclear Physics A*, vol. 106, no. 3, pp. 545–569, 1968.

[91] L. G.-M. Zaragoza, J.-P. Ebran, S. Hilaire, S. Péru, M. Frosini, and T. Duguet, "Towards systematic large scale Quasiparticle Random-Phase Approximation calculations with covariant and chiral interactions," in *EPJ Web of Conferences*, vol. 294, p. 03003, EDP Sciences, 2024.

[92] S. Hilaire and M. Girod, "The AMEDEE nuclear structure database," in *International Conference on Nuclear Data for Science and Technology*, pp. 107–110, EDP Sciences, 2007.

[93] W. Huang, M. Wang, F. G. Kondev, G. Audi, and S. Naimi, "The AME2020 atomic mass evaluation (I). Evaluation of input data, and adjustment procedures," *Chinese Physics C*, vol. 45, no. 3, p. 030002, 2021.

[94] M. Wang, W. J. Huang, F. G. Kondev, G. Audi, and S. Naimi, "The AME2020 atomic mass evaluation (II). tables, graphs and references," *Chinese Physics C*, vol. 45, no. 3, p. 030003, 2021.

[95] S. Agbemava, A. Afanasjev, D. Ray, and P. Ring, "Global performance of covariant energy density functionals: Ground state observables of even-even nuclei and the estimate of theoretical uncertainties," *Physical Review C*, vol. 89, no. 5, p. 054320, 2014.

[96] I. Angeli and K. P. Marinova, "Table of experimental nuclear ground state charge radii: An update," *Atomic Data and Nuclear Data Tables*, vol. 99, no. 1, pp. 69–95, 2013.

[97] J. Terasaki, J. Engel, M. Bender, J. Dobaczewski, W. Nazarewicz, and M. Stoitsov, "Self-consistent description of multipole strength in exotic nuclei: Method," *Physical Review C–Nuclear Physics*, vol. 71, no. 3, p. 034310, 2005.

[98] J. Gaardhoje, "Nuclear structure at high excitation energy studied with giant resonances," *Annual review of nuclear and particle science. Volume 42*, 1992.

[99] F. Bečvář, "What do we really know about photon strength functions?," *Journal of Physics G: Nuclear and Particle Physics*, vol. 35, no. 1, p. 014025, 2007.

[100] A. Tamii, L. Pellegri, P.-A. Söderström, D. Allard, S. Goriely, T. Inakura, E. Khan, E. Kido, M. Kimura, E. Litvinova, *et al.*, "PANDORA project for the study of photonuclear reactions below A= 60," *The European Physical Journal A*, vol. 59, no. 9, p. 208, 2023.

[101] M. Miorelli, S. Bacca, N. Barnea, G. Hagen, G. Jansen, G. Orlandini, and T. Papenbrock, "Electric dipole polarizability from first principles calculations," *Physical Review C*, vol. 94, no. 3, p. 034317, 2016.

[102] J. Birkhan, M. Miorelli, S. Bacca, S. Bassauer, C. Bertulani, G. Hagen, H. Matsubara, P. von Neumann-Cosel, T. Papenbrock, N. Pietralla, *et al.*, "Electric dipole polarizability of ca 48 and implications for the neutron skin," *Physical review letters*, vol. 118, no. 25, p. 252501, 2017.

[103] M. Kruse, W. Ormand, and C. Johnson, "No-core shell model calculations of the photonuclear cross section of 10b," *The European Physical Journal A*, vol. 55, no. 12, p. 225, 2019.

[104] F. Bonaiti, S. Bacca, G. Hagen, and G. R. Jansen, "Electromagnetic observables of open-shell nuclei from coupled-cluster theory," *Physical Review C*, vol. 110, no. 4, p. 044306, 2024.

[105] B. Carlsson, J. Toivanen, and U. von Barth, "Fluctuating parts of nuclear ground-state correlation energies," *Physical Review C–Nuclear Physics*, vol. 87, no. 5, p. 054303, 2013.

[106] A. Nogga, S. K. Bogner, and A. Schwenk, "Low-momentum interaction in few-nucleon systems," *Physical Review C–Nuclear Physics*, vol. 70, no. 6, p. 061002, 2004.

[107] M. Frosini, T. Duguet, B. Bally, Y. Beaujeault-Taudière, J.-P. Ebran, and V. Somà, "In-medium k-body reduction of n-body operators: A flexible symmetry-conserving approach based on the sole one-body density matrix," *The European Physical Journal A*, vol. 57, no. 4, p. 151, 2021.

[108] B. B. et al., "Mean-field approximation on steroids: description of the deuteron," *arXiv preprint arXiv:2410.03356*, 2024.

[109] A. Scalesi, T. Duguet, M. Frosini, and V. Somà, "Deformed natural orbitals for ab initio calculations," *arXiv preprint arXiv:2407.18308*, 2024.

[110] J. Piekarewicz, B. Agrawal, G. Colo, W. Nazarewicz, N. Paar, P.-G. Reinhard, X. Roca-Maza, and D. Vretenar, "Electric dipole polarizability and the neutron skin," *Physical Review C–Nuclear Physics*, vol. 85, no. 4, p. 041302, 2012.

[111] Z. Li, Y. Niu, and W. Long, "Electric dipole polarizability in neutron-rich Sn isotopes as a probe of nuclear isovector properties," *Physical Review C*, vol. 103, no. 6, p. 064301, 2021.

[112] M. Frosini, W. Ryssens, and K. Sieja, "Quasiparticle random-phase approximation in valence spaces: The case of magnetic dipole transitions," *Physical Review C*, vol. 110, no. 1, p. 014307, 2024.

[113] G. Haouat, C. Lagrange, R. De Swiniarski, F. Dietrich, J. Delaroche, and Y. Patin, "Nuclear deformations of ^{24}Mg , ^{28}Si, and ^{32}S from fast neutron scattering," *Physical Review C*, vol. 30, no. 6, p. 1795, 1984.

[114] W. von Oertzen, M. Freer, and Y. Kanada-En'yo, "Nuclear clusters and nuclear molecules," *Physics Reports*, vol. 432, no. 2, pp. 43–113, 2006.

[115] J.-P. Ebran, E. Khan, T. Nikšić, and D. Vretenar, "How atomic nuclei cluster," *Nature*, vol. 487, no. 7407, pp. 341–344, 2012.

[116] M. Chernykh, H. Feldmeier, T. Neff, P. von Neumann-Cosel, and A. Richter, "Structure of the Hoyle state in ^{12}c," *Physical review letters*, vol. 98, no. 3, p. 032501, 2007.

[117] J.-P. Ebran, E. Khan, T. Nikšić, and D. Vretenar, "Density functional theory studies of cluster states in nuclei," *Physical Review C*, vol. 90, no. 5, p. 054329, 2014.

[118] M. Girod and P. Schuck, "α-particle clustering from expanding self-conjugate nuclei within the Hartree-Fock-Bogoliubov approach," *Physical review letters*, vol. 111, no. 13, p. 132503, 2013.

[119] Y. Alhassid, B. Bush, and S. Levit, "Thermal shape fluctuations, landau theory, and giant dipole resonances in hot rotating nuclei," *Physical review letters*, vol. 61, no. 17, p. 1926, 1988.

[120] E. Grosse, A. R. Junghans, and R. Massarczyk, "Breaking of axial symmetry in excited heavy nuclei as identified in giant dipole resonance data," *The European Physical Journal A*, vol. 53, pp. 1–21, 2017.

[121] V. Varlamov, M. Stepanov, and V. Chesnokov, "New data on photoabsorption reaction cross sections," *Izvestiya Akademii Nauk. Rossijskaya Akademiya Nauk. Seriya Fizicheskaya*, vol. 67, no. 5, pp. 656–663, 2003.

[122] B. Ishkhanov, I. Kapitonov, E. Lileeva, E. Shirokov, V. Erokhova, M. Elkin, and A. Izotova, "Cross sections of photon absorption by nuclei with nucleon numbers 12-65," in *, Moscow*, 2002.

[123] M. Frosini, T. Duguet, P. Tamagno, and L. Zurek, "Dimensionality reduction through tensor factorization: application to ab initio nuclear physics calculations," *arXiv preprint arXiv:2407.17971*, 2024.

[124] G. L. Sleijpen and H. A. Van der Vorst, "A Jacobi–Davidson iteration method for linear eigenvalue problems," *SIAM review*, vol. 42, no. 2, pp. 267–293, 2000.

[125] M. E. Hochstenbach and Y. Notay, "The Jacobi–Davidson method," *GAMM-Mitteilungen*, vol. 29, no. 2, pp. 368–382, 2006.

[126] P. Arbenz and M. E. Hochstenbach, "A Jacobi–Davidson method for solving complex symmetric eigenvalue problems," *SIAM Journal on Scientific Computing*, vol. 25, no. 5, pp. 1655–1673, 2004.

[127] W. Ryssens and Y. Alhassid, "Finite-temperature mean-field approximations for shell model Hamiltonians: the code HF-SHELL," *The European Physical Journal A*, vol. 57, pp. 1–18, 2021.

[128] B. A. Brown and W. Richter, "New "USD" Hamiltonians for the sd shell," *Physical Review C–Nuclear Physics*, vol. 74, no. 3, p. 034315, 2006.

[129] S. Péru, G. Gosselin, M. Martini, M. Dupuis, S. Hilaire, and J.-C. Devaux, "Giant resonances in ^{238}U within the quasiparticle random-phase approximation with the Gogny force," *Physical Review C–Nuclear Physics*, vol. 83, no. 1, p. 014314, 2011.

[130] E. Sanderson, "Nuclear ground states in the random phase approximation," *Physics Letters*, vol. 19, no. 2, pp. 141–143, 1965.

[131] D. Rowe, "Methods for calculating ground-state correlations of vibrational nuclei," *Physical Review*, vol. 175, no. 4, p. 1283, 1968.

[132] P. Ellis, "Particle-hole and particle-particle RPA ground state correlations," *Nuclear Physics A*, vol. 467, no. 2, pp. 173–184, 1987.

[133] A. Bouyssy and N. V. Mau, "Particle-hole and particle-particle RPA ground state correlations and the Green function formalism," *Nuclear Physics A*, vol. 229, no. 1, pp. 1–14, 1974.

[134] J. Terasaki, "Overlap of quasiparticle random-phase approximation states based on ground states of different nuclei: Mathematical properties and test calculations," *Physical review C*, vol. 87, no. 2, p. 024316, 2013.

[135] A. Meurer, C. P. Smith, M. Paprocki, O. Čertík, S. B. Kirpichev, M. Rocklin, A. Kumar, S. Ivanov, J. K. Moore, S. Singh, *et al.*, "SymPy: symbolic computing in Python," *PeerJ Computer Science*, vol. 3, p. e103, 2017.

[136] A. Signoracci, T. Duguet, G. Hagen, and G. Jansen, "Ab initio Bogoliubov coupled cluster theory for open-shell nuclei," *Physical Review C*, vol. 91, no. 6, p. 064320, 2015.

[137] G. E. Scuseria, T. M. Henderson, and D. C. Sorensen, "The ground state correlation energy of the random phase approximation from a ring coupled cluster doubles approach," *The Journal of chemical physics*, vol. 129, no. 23, 2008.

[138] I. Stetcu and C. W. Johnson, "Random phase approximation vs exact shell-model correlation energies," *Physical Review C*, vol. 66, no. 3, p. 034301, 2002.

[139] D. Brink and E. Boeker, "Effective interactions for Hartree-Fock calculations," *Nuclear Physics A*, vol. 91, no. 1, pp. 1–26, 1967.

[140] D. W. Lozier, "NIST digital library of mathematical functions," *Annals of Mathematics and Artificial Intelligence*, vol. 38, pp. 105–119, 2003.